

NONINVASIVE CHARACTERIZATION OF SKELETAL MUSCLE DAMAGE AND
REPAIR IN MURINE MODELS OF MUSCULAR

By

NATHAN DAVID BRYANT

A DISSERTATION PRESENTED TO THE GRADUATE SCHOOL
OF THE UNIVERSITY OF FLORIDA IN PARTIAL FULFILLMENT
OF THE REQUIREMENTS FOR THE DEGREE OF
DOCTOR OF PHILOSOPHY

UNIVERSITY OF FLORIDA

2010

© 2010 Nathan David Bryant

To my friends and family who carried me through the most difficult times and to my mentors that showed me the path. I could not have done this without you.

ACKNOWLEDGMENTS

I would like to thank the NIH T-32 Training program in Neuromuscular Plasticity in Rehabilitation (T32H D043730) for giving me the opportunity to work in this field, providing guidance in career planning and introducing me to the world of clinical research and practice. I would also like to acknowledge Dr. Elizabeth McNally for providing the γ -sarcoglycan^{-/-} knockout mice used in this study and Dr. Philip Miles for his invaluable mentoring in the areas of scientific writing and presentation. Funding for this research was provided by the Muscular Dystrophy Association (MDA) and the National Institutes of Health (NIH) R01AR47292T, R01HL78670, and T32H D043730.

TABLE OF CONTENTS

	<u>page</u>
ACKNOWLEDGMENTS.....	4
LIST OF TABLES.....	9
LIST OF FIGURES.....	10
LIST OF ABBREVIATIONS.....	13
ABSTRACT.....	15
CHAPTER	
1 INTRODUCTION AND BACKGROUND.....	17
Skeletal Muscle.....	18
Growth and Repair of Skeletal Muscle.....	19
Structural Organization Within the Muscle Fiber.....	21
Dystrophin and the Sarcolemma.....	23
Muscular Dystrophy.....	23
Clinical Impact and Symptoms.....	23
Pathology.....	26
Laboratory Models of Muscular Dystrophy.....	27
Animal models of dystrophinopathies.....	27
Animal models of sarcanopathies.....	29
Approaches to treatment of muscular dystrophy.....	30
Monitoring disease progression.....	34
Magnetic Resonance Imaging (MRI).....	35
Basic Components Required for MR or NMR.....	36
The Origin of the Signal.....	36
The Larmor frequency.....	37
The 90° RF pulse and the B ₁ field.....	38
The free induction decay (FID).....	38
Basic Parameters of MR.....	39
Longitudinal relaxation (T ₁) and pulse repetition time (TR).....	39
Transverse relaxation (T ₂) time and echo time (TE).....	40
Spatial localization of the signal.....	42
MRI Contrast Methods.....	44
MRI of Skeletal Muscle.....	48
MRI of muscular dystrophy.....	51
Summary.....	53

2	OUTLINE OF EXPERIMENTS.....	62
	Overview.....	62
	Experiment 1: T ₂ as a Marker for Sarcolemmal Damage in Dystrophy Muscle.....	63
	Hypothesis 1.....	64
	Specific Aim 1.....	64
	Experiment 2: Diffusion Imaging to Monitor Recovery From Damage.	64
	Hypothesis 2.....	65
	Specific Aim 2.....	65
	Experiment 3: Magnetization Transfer Imaging to Assess Fibrosis.	65
	Hypothesis 3.....	65
	Specific Aim 3.....	66
3	METHODOLOGY	68
	Animals.....	68
	Rodent Handling and Care.	68
	Mouse Strains	68
	Gene Delivery to Young LGMD Mice.	70
	Exercise Induced Eccentric Damage: Downhill Treadmill Running.	71
	Magnetic Resonance Imaging	72
	Determination of Muscle T ₂	72
	Determination of Mean ADC at 4.7T.	73
	Determination of ADC and FA at 11T.....	75
	Determination of MTR:	76
	Measurement of Longitudinal Relaxation (T ₁).	77
	Histology.....	78
	Histological Verification of Sarcolemmal Damage.	78
	Histological Quantification of Fibrosis.....	79
	Verification of transgene expression in gene delivery experiments.	79
4	EXPERIMENT 1: DETECTION OF SARCOLEMMAL DAMAGE IN DYSTROPHIC MUSCLE WITH T ₂ WEIGHTED MRI.....	89
	Abstract.....	89
	Introduction	89
	Dystrophic Muscle Undergoes Bouts of Acute Damage.....	89
	T ₂ Relaxation as a Measure of Muscle Damage.	90
	Multi-Exponential T ₂ Decay in Skeletal Muscle.	91
	Proposed Origins of T ₂ Components in Skeletal Muscle.	92
	Purpose and Summary.....	93
	Methods.....	94
	Animals.....	94
	Gene Correction.....	94
	Histological Verification of Sarcolemmal Damage.....	94
	Non-Negative Least Squares (NNLS) Analysis of Multicomponent T ₂	95

Results.....	96
Assessment of Acute Damage in Dystrophic Muscle Using T ₂ -weighted MRI.....	96
T ₂ MRI: Detection of Gene Correction.....	97
NNLS Analysis of Multicomponent T ₂	97
Discussion	99
5 EXPERIMENT 2: IMAGING REGENERATION IN DYSTROPHIC MUSCLE USING T₂ AND DIFFUSION MRI.....	111
Abstract.....	111
Introduction	112
Detecting Changes in Microstructure with Diffusion MR.....	113
Diffusion Tensor Imaging of Skeletal Muscle.....	114
Experimental Design.....	117
Results.....	119
Diffusion weighted imaging of recovery from acute damage in healthy control C57BL/10 mice.....	119
Diffusion weighting imaging of damaged and unaffected muscle in <i>mdx</i> mice.	120
Diffusion weighted imaging of rAAV correct <i>sgca</i> ^{-/-} mice.....	121
Diffusion tensor imaging (DTI) in rAAV corrected <i>sgcg</i> ^{-/-} mice.....	122
Recovery from eccentric damage.....	122
Discussion	123
6 EXPERIMENT 3: ASSESSMENT OF DAMAGE AND FIBROSIS IN DYSTROPHIC MUSCLE USING MAGNETIZATION TRANSFER MRI.....	136
Abstract.....	136
Introduction	136
Detection of Fibrosis with Magnetization Transfer Imaging.....	137
MT Imaging of Dystrophic Muscle.	138
MT Imaging of Damaged and Fibrotic Muscle.....	139
Methods.....	140
Animals.....	140
MR Imaging Data Acquisition	140
MR Image Analysis	142
Histological Measurements.	143
Postnatal Gene Delivery.....	143
Statistical analysis	144
Results.....	144
Optimization of Magnetization Transfer Contrast.	144
T ₂ and MTR in Gastrocnemius Muscles From Young and Old Control and Dystrophic Mice.....	145
Histological Assessment of Fibrosis in Dystrophic Muscle.....	147
Use of T ₂ and MTR in Monitoring Therapeutic Intervention.....	148
Discussion	148

7 CONCLUSION.....	161
REFERENCES.....	164
BIOGRAPHICAL SKETCH.....	178

LIST OF TABLES

<u>Table</u>		<u>page</u>
6-1	Comparison of T_2 and MTR for TA and GAS muscles by age and strain	160
6-2	T_2 and MTR for unaffected regions ($T_2 < 29$ ms) of TA and GAS muscles	160

LIST OF FIGURES

<u>Figure</u>	<u>page</u>
1-1	Bout of damage and repair drive disease progression in muscular dystrophy... 54
1-2	Mouse models of Duchenne (DMD)/Beckers muscular dystrophy and limb-girdle muscular dystrophy (LGMD) compared to a health C57/B10 mouse..... 55
1-3	Limitations of classical invasive measures 56
1-4	Spin echo sequence. 57
1-5	Longitudinal relaxation: T_1 recovery. 58
1-6	Transverse relaxation 59
2-1	An overview of dystrophic disease progression and the specific aims of this research. 67
3-1	Mouse age cohorts and experimental design 82
3-2	Gene correction model 83
3-3	Radio frequency coil and sample positioning for MRI..... 84
3-4	Diffusion in the plane perpendicular to net fiber orientation (axial) was determined by fitting the exponential diffusion dependant loss of signal with increasing diffusion gradient strength (reflected in the increased b value) <i>in vivo</i> at 11T 85
3-5	MR cradle mounted heating block. 86
3-6	T_1 was measured in the hindlimb muscles of aged C57BL/10 and <i>mdx</i> mice..... 87
3-7	Verification of human γ -sarcoglycan expression in rAAV treated γ -sg ^{-/-} mice..... 88
4-1	T_2 weight assessment of damage in young and old <i>mdx</i> muscle 103
4-2	Histological verification of intensity and distribution of muscle damage in murine models of muscular dystrophy 104
4-3	Immunohistochemical labeling of γ -sarcoglycan in muscle of the untreated 105
4-4	Correction of the rAAV treated limb in α -sg ^{-/-} and γ -sg ^{-/-} mice was easily observed in T_2 weighted MRI..... 106
4-5	Dystrophic muscle pathology is characterized by an increased heterogeneity in T_2 107

4-6	Multiple component T_2 analysis of computer simulated T_2 relaxation times	108
4-7	Multiple component T_2 analysis in copper sulfate (CuSO_4) phantoms.....	109
4-8	Multiple component T_2 analysis in dystrophic muscle.....	110
5-1	The diffusion of water molecules can be restricted by physical barriers in biological tissues	127
5-2	Muscle fibers are normally rather anisotropic and in our experiments the length of the muscle fibers run approximately parallel to the Z-axis, while the X axis and Y axis are perpendicular to the fiber	128
5-3	Muscle fibers of the TA muscle relative to the diffusion sensitive pulsed field gradients used in the DWI sequences at 4.7T	129
5-4	Diffusion weighted imaging of gene corrected LGMD mice	130
5-5	Directions and diffusion weighting in diffusion tensor imaging.....	131
5-6	Diffusion tensor imaging of viral vector treated $\gamma\text{-sg}^{-/-}$ mice	132
5-7	Schematic diagram illustrating the downhill running protocol	133
5-8	Control C57 and <i>mdx</i> hindlimb muscle post downhill treadmill running.....	134
5-9	T_2 and diffusion indices during recovery from eccentric contraction induced muscle damage.	135
6-1	Typical T_2 and magnetization transfer contrast and the Z-Spectra from damaged and undamaged muscle.	153
6-2	Z-spectra from the gastrocnemius muscles of old C57BL10 control and old <i>mdx</i> mice	154
6-3	Lesions in young dystrophic mice are distinctly visible in magnetization transfer (MT) contrast images and have a similar spatial distribution as damage observable in T_2 weighted images.....	155
6-4	T_2 and MTR in unaffected ($T_2 < 29$ ms) GAS muscle.	156
6-5	Extensive fibrosis was seen in the muscles of older (>1.5yr) dystrophic mice and is not observed in control C57BL10 mice	157
6-6	Extensive fibrosis was observed in the old <i>mdx</i> muscle as compared to the C57 control	158

6-7	MT contrast was able to detect genetic correction of dystrophic muscle tissue	159
7-1	A model of multiple methods of MRI contrast at various stages of damage and disease progression is show above	163

LIST OF ABBREVIATIONS

AAV	adeno-associated virus
B_0	magnitude of static magnetic field
B_1	magnitude of excitatory radiofrequency field
BMD	Becker muscular dystrophy. A form of muscular dystrophy with partial expression of the protein dystrophin.
DAG Complex	dystrophin associated glycoprotein complex. A transmembrane glycoprotein complex that structurally links the cytosolic protein dystrophin to the extracellular matrix via the protein laminin. This complex includes as subunits the sarcoglycans which are involved in limb-girdle muscular dystrophy.
DMD	Duchenne muscular dystrophy. The most common and severe form of muscular dystrophy due to a lack of the protein Dystrophin.
DTI	diffusion tensor imaging
DWI	diffusion weighted imaging
ECM	extracellular matrix
FID	free induction decay.
FOV	field of view
GAS	Gastrocnemius muscle
LGMD	limb-girdle muscular dystrophy. This includes several forms of muscular dystrophy. The causes include absence of the subunits of the dystrophin-associated-glycoprotein complex, including the sarcoglycans.
<i>mdx</i>	muscular dystrophy X-linked. A genetic mouse model of Duchenne and Becker Muscular Dystrophy due to its dystrophin expression being little to none.
MRI	magnetic resonance imaging.
MTC	magnetization transfer contrast
MTR	magnetization transfer ratio
NMR	nuclear magnetic resonance.

RF	radio frequency
sgca ^{-/-}	an α -sarcoglycan deficient knock out mouse that is a model of limb-girdle muscular dystrophy.
sgcg ^{-/-}	an γ -sarcoglycan deficient knock out mouse that is a model of limb-girdle muscular dystrophy.
SNR	Signal to noise ratio
SOL	Soleus muscle
T ₁	longitudinal relaxation rate constant
T ₂	transverse relaxation rate constant
T ₂ *	apparent transverse relaxation time
TA	Tibialis Anterior muscle
TE	echo time
TR	pulse repetition time

Abstract of Dissertation Presented to the Graduate School
of the University of Florida in Partial Fulfillment of the
Requirements for the Degree of Doctor of Philosophy

NONINVASIVE CHARACTERIZATION OF SKELETAL MUSCLE DAMAGE AND
REPAIR IN MURINE MODELS OF MUSCULAR DYSTROPHY

By

Nathan David Bryant

May 2010

Chair: Glenn A. Walter

Major: Medical Sciences – Physiology and Pharmacology

The muscular dystrophies represent a class of devastating neuromuscular diseases that lead to the rapid wasting of muscle. Currently, there is no cure for muscular dystrophy. Duchenne muscular dystrophy is one of the most devastating forms of muscular dystrophy resulting rapid progression and loss of ambulation in the early teenage years. Eventually the disease will prove to be fatal, due to both respiratory and cardiac muscle failure.

Current invasive assays, such as muscle biopsy, are limited in their ability to accurately represent the entire tissue. The heterogeneous distribution, both spatially and temporally, of damaged and regenerating muscle fibers in the presence of fibrosis and fatty tissue infiltration makes biopsy much less reliable until later stages when the entire muscle is uniformly involved. In contrast, noninvasive imaging methods, such as magnetic resonance imaging (MRI), have the advantage of noninvasive detection of tissue pathology in three dimensions. A wide range of endogenous MRI contrast methods provides tools for researchers and clinicians to locate pathological features like muscle damage, edema, atrophy, and fat infiltration but most of these have been used in a purely qualitative manner. With this in mind, I set out to establish several working

models of muscle damage, repair, and therapeutic correction in animal models of muscular dystrophy in order to develop effective monitoring and quantitative assessment protocols using MRI. I established that transverse relaxation (T_2) is a consistent indicator of sarcolemmal damage in dystrophic skeletal muscle in both Duchenne and limb-girdle models of muscular dystrophy. I also explored the multi-exponential nature of muscle tissue T_2 and its relationship to muscle damage. Taking it a step further, I studied changes in myofiber structure noninvasively using diffusion weighted imaging follow eccentric damage from downhill running. The use of diffusion tensor imaging (DTI) provided detailed insight into the underlying changes occurring over the throughout a two week period post injury. Ultimately, the muscle exhausts its ability to undergo this regenerative phase and its contractile tissue is replaced by fibro-fatty tissue. Unfortunately, fibrosis is extremely difficult to directly image, due to its extremely short transverse relaxation times. Therefore, I investigated an alternative approach to image “tightly” bound water molecules associated with tissue fibrosis. Magnetization transfer (MT) allows for the indirect imaging of fibrosis by looking at the proton MT between a free liquid pool and a macromolecular bound pool, of which, collagen is a major component in fibrosis. Combining these different basic MR imaging properties of muscle, I developed a multimodal approach to gain new perspectives in monitoring disease progression and detecting efficacy of potential treatments in animal models of muscular dystrophy.

CHAPTER 1 INTRODUCTION AND BACKGROUND

The ultimate goal in muscular dystrophy research is to find cures for the various forms of the disease. While many promising preclinical trials are under way, there still largely remains the lack of a non-invasive monitoring protocol that provides a detailed profile of a muscle's pathological condition *in vivo*. Non-invasive measures offer a significant advantage over traditional histological methods on several fronts. For one, they allow repeated measures on the same subject, in longitudinal studies, without destroying the tissue in question. Another benefit is that the researcher is able to quickly collect data representing large areas of the body simultaneously. This provides data that reflects the entire muscle in question, as opposed to being confined to the histology observable via a localized muscle biopsy. For instance it has been shown that an accurate measure of muscle fiber type distribution within the healthy human quadriceps muscle requires at least three biopsies (1).

Skeletal muscle and its pathologies have been studied with non-invasive modalities such as computed tomography (CT; (2)), ultrasonography US; (3, 4), positron emission tomography (PET; (5)), and magnetic resonance imaging (MRI; (6)) and spectroscopy (MRS; (7)). Each modality has its unique advantages. For instance, ultrasound provides a cheap and fast measurement of fascicle structure (8), but lacks metabolic information. PET on the other hand provides extremely sensitive measures of small amounts of target tracers and glucose metabolism, but lacks anatomical information. MRI can provide both high-resolution anatomical and metabolic information. This is a great advantage, as registration between spatial data of two unrelated noninvasive techniques can be very difficult; for example overlaying PET data over high

resolution anatomical CT data. By using MRS and MRI, all of the metabolic or chemical composition data can be collected with the same experimental set up as the high resolution imaging. In addition, depending on what nuclei the instrument coils are tuned to, a wide variety of tissue composition and relative metabolic intermediate changes can be recorded. For example, localized ^1H MRS can be used in conjunction with numerous two and three-dimensional imaging protocols using the same ^1H tuned coil. This type of experiment is especially useful in looking at water to fat ratios in various biological samples and with the ability to precisely defining specific regions from which the spectra is collected (9). ^1H MRI can also be used along side ^{31}P MRS and has proven to be valuable in healthy and diseased muscle research (10). Such studies in skeletal muscle are often interested in following changes in phosphorylated metabolic intermediates, including phosphocreatine (PCr) and the individual phosphate groups the various phosphorylated forms of the predominant energy shuttle and regulatory nucleoside adenosine; ie ATP, ADP, and AMP (11). In these ^{31}P experiments, environmental changes in muscle tissue can also be monitored; such as changes in intracellular pH (12). For those researching diseases in humans and in animal models, the vast and powerful applications of NMR are commonly available in both the clinical and research laboratory setting. As such, MR is a rapidly growing field in noninvasive medical imaging that we feel is perfectly suited for the study of disease, atrophy, damage and repair in skeletal muscle.

Skeletal Muscle

Skeletal muscle is a unique tissue and displays impressive levels of specialization making it possible for us to move about our environment, speak, and draw each vital breath of air. Skeletal muscle exhibits incredible plasticity (13), making it sensitive to

disuse atrophy, but also allowing for drastic adaptation with rehabilitation (14). Muscle also has a tremendous regenerative capacity capable of completely regenerating itself within mere days of an injury (15). In a healthy individual, muscle injury is a common event and plays a role in every day hypertrophy and in the extreme cases of muscle building in weight bearing exercise. Normally, when minor damage to a muscle fiber occurs, growth factors and cytokines are released and populations of pluripotent stem cells and muscle satellite cells are activated and will home toward the source of the signal. The muscle progenitor cells either fuse with existing damaged fibers or they differentiate and fuse with each other to form new fibers. Overall this results in a very dynamic process resulting continual muscle growth, remodeling and repair. For all these reasons, it makes it all more devastating when this regenerative capacity is exhausted in the event of disease. This is dramatically illustrated in children with Duchenne muscular dystrophy (DMD) that have normal to enlarged muscles prior to clinical manifestations (Figure 1-1) due to the inability to match tissue regeneration with the damage associated with normal ambulation, breathing, or cardiac function in the face of a structural muscle deficiency.

Growth and Repair of Skeletal Muscle

Skeletal muscle tissue is made up of bundles individual muscle fibers. Each of these muscle fibers is a multinucleated single cell. The distance between these myonuclei is heavily regulated, forming myonuclear domains (16). This plays an important role in understanding repair of damage and recovery from atrophy. As a myofiber decreases in diameter, these myonuclei are brought closer together. Once the minimal spatial barriers of the myonuclear domain are violated the myonuclei will become an apoptotic nucleus and it will be lost by the muscle fiber. Although, it has

been debated as to which event triggers the apoptosis in the nuclei, Gundersen *et al.* observed no myonuclear loss in the first weeks of atrophy but did see a decrease in fiber diameter (17). This may suggest that there is a range of acceptable fiber diameters and that there is a lower size threshold that is associated with the loss of nuclei. Mature myonuclei do not divide and the muscle fibers are limited in their diameter by the number of their nuclei; i.e. there seems to also be an upper threshold that limits fiber diameter when there are too few nuclei in that region. This then affects the ability of muscle tissue to recover from necrotic damage or atrophy; where many myonuclei were lost. In order for the fibers to increase in diameter, new myonuclei must be introduced to the fiber. These nascent nuclei come from satellite cells (18) and muscle progenitor cells. During muscle repair, on a cellular level, many events are similar to embryonic development (19). A reserve of these satellite cells reside largely in the basement membrane, between the plasmalemma and the basal lamina, surrounding the myofibers and are generally in a quiescent state in adult muscle tissue (20). These populations of satellite cells have been shown to be heterogeneous in nature (21), but as a group they are often characterized as being positive for M-cadherin, Pax7, Myf5, and neural cell adhesion molecule-1 (22). During development, several transcription factors are expressed that regulate early genes in muscle cell differentiation and myofiber maturation. Among these transcription factors are Pax3 and Pax7. Lepper *et al.* in 2009 demonstrated that while Pax3 and Pax7 had a role in embryonic development, only Pax7 was important to mechanisms of growth and repair in the postnatal animal (23). In fact, due to its roles in survival, proliferation and commitment to a muscle lineage of differentiation, Pax7 has become a recognized cellular marker for tracking muscle

satellite cell activation during these growth and repair events in the laboratory. In addition to Pax7, several other markers of muscle cell lineage and differentiation are used to study these processes. Members of a Myc-c related superfamily are closely monitored in the laboratory and include MyoD1, myogenin, myf-5 and MRF4 (24). In general, these regulatory proteins activate other members in the family resulting in a cascade that results in myoblast and fiber maturation (24).

When new muscle growth or repair is needed in adult skeletal muscle these satellite cells ($Pax7^+/Pax3^{+/-}/Myf5^{+/-}$) are activated and proliferate (25). A small fraction of these new satellite cells will not express MyoD, and they will presumably return to the quiescent pool to replenish the reserve for future repair and growth (25). The $MyoD^+$ cells become mononucleated myoblasts ($Pax7^+/Myf5^+/MyoD^+$) (26) and migrate to the area of tissue that needs repair. As these myoblasts fuse, they will start to express myogenin and later the nucleus within this domain will start to express embryonic myosin. Thus, embryonic myosin is a marker of new or recently repaired myofibers. These nascent muscle fibers will also have centrally located myonuclei, providing a histological marker of new fiber growth and repair, which move to the periphery upon maturation (marker of healthy adult skeletal muscle).

Structural Organization Within the Muscle Fiber

Within each muscle fiber, are dense arrays of myofibrils that are made up of repeating sarcomeres. Each sarcomere is in turn made up of overlapping thick and thin filaments (of myosin and actin/tropomyosin/troponin respectively) that are interdigitated and able to slide past each other during contraction. At each end of the sarcomere, is a Z-disk. The Z-disks organize the ends of the filaments and in striated skeletal muscle, are bound to neighboring Z-disks, giving the tissue its recognizable “striped” or striated

appearance, and add to the organized structure of the myofibrils. The Z-disks are tethered to the center of each sarcomere by the massive protein titin. Titin is the largest known protein in humans and each individual molecule spans half of a sarcomere. One terminal domain of titin has an elastic property, while the other largely acts to regulate the length of extended sarcomeres. The thin filaments are bound to the protein nebulin, which performs a similar function for regulating the length of the thin actin filaments (27).

During contraction it is the heads of the myosin proteins making up the thick filaments that bind to active sites on the actin filament and then follow through with a power stroke, pulling the Z-disks one increment closer together. The myosin head then releases, triggered by Ca^{++} influx to the cytoplasm from the sarcoplasmic reticulum, and re-cocks as ATP is hydrolysed by the protein; thus it actually requires energy to relax the muscle as opposed to contract it. This can be observed in the muscle stiffening that occurs following death; *rigor mortis*. The myosin head alternate relaxing, binding the muscle contracts as each sarcomere simultaneously shortens. During eccentric contractions the muscle is forced to lengthen during this myosin head cycling event and damage is done to the fibers at the level of the z disk (28) and muscle membrane (29). This will be an important concept later in this dissertation. The Z-disks are rich in the protein desmin, which is also found in costameres (30). Desmin is solely found in muscle tissue and is another biological marker for muscle lineage differentiation (both myoblasts and fibers are positive for desmin). Costameres are complexes associated with desmin and other cytoskeletal proteins and are found in the outer membrane of the cell and serve to link the contractile machinery and f-actin cytoskeleton to the

extracellular matrix (31). One such costamere that is particularly important in muscular dystrophy is the dystrophin-associated glycoprotein complex or DAG complex, because this is where the gene mutation in many dystrophies affects the stability of the cell membrane making it susceptible to damage.

Dystrophin and the Sarcolemma

In muscle fibers, the cellular plasma membrane is called the sarcolemma. The f-actin cytoskeleton is tethered to the sarcolemma through the structural protein dystrophin. The dystrophin proteins are anchored to the inner surface of the sarcolemma through the dystrophin associated glycoprotein (DAG) complex (10) costamere. On the extracellular side, the complex is then attached to laminin, which in turn is bound to the extracellular matrix (ECM). The ECM is largely made up of the protein collagen and proteoglycans. The various forms of muscular dystrophy arise when gene mutations prevent any of the proteins in this network that stabilizes the sarcolemma during muscle contraction.

Not all of the DAG complexes functions are structural. The complex is large and has many subunits. Some of these bind to cellular proteins that are important in cellular signaling and regulation metabolism. One such protein that forms a part of the complex is neural nitric oxide synthase (nNOS). nNOS is required in skeletal muscle to maintain activity following exercise (32). This led to the observation that mice with disrupted DAG complexes were more susceptible to fatigue (32), further debilitating the individual.

Muscular Dystrophy

Clinical Impact and Symptoms

The muscular dystrophies are a group of genetic diseases exhibiting progressive skeletal muscle wasting due to a structural weakness in the sarcolemma. The most

prevalent and severe form, Duchenne muscular dystrophy (DMD), arises from a mutation in the 2.4Mb gene coding the protein dystrophin located on the X-chromosome and its phenotype is recessive. In DMD, this mutation is generally a nonsense or frameshift mutation that results in the complete absence of the functional protein. In the less severe Becker muscular dystrophy (BMD), some level of dystrophin is present, though it is often structurally truncated or has a reduced expression level. DMD/BMD occurs in one out of 3,500 to 5,000 male children, giving rise to an estimated 400 to 600 new cases in the United States each year (CDC, SGDD 2006). Onset of symptoms of DMD can often be seen between 2 to 6 years of age and manifest as general weakness of voluntary skeletal muscles, especially in the hips, pelvis, thighs and shoulders. Impaired ability to rise to a standing position from a prone position is common and the use of the arms to “walk” up the body until upright, also known as the Gower’s sign, is suggestive of a dystrophic diagnosis. Enlarged calf muscles are also typical and are considered to be the result of pseudohypertrophy (33-36). In DMD, the loss of effective ambulation usually occurs around the age of 12, but could occur as young as 7 years old. As the disease progresses, there is increasing involvement of the muscles of respiration (diaphragm) and of the heart. This leads to further complications, often in the late teenage years to the late twenties, where weakened respiratory function, cardiac failure, or an increased susceptibility to infection may prove to be fatal. In BMD similar trends are observed, but the time of onset is shifted later in life. The symptoms are often milder than in DMD, yet the path of progression is much less predictable. In addition to the dystrophies that lack dystrophin itself, there are numerous other forms that are caused by mutations that result in the disruption of the dystrophin associated glycoprotein

(DAG) complex. Among these, are the limb-girdle muscular dystrophies (LGMD), of which at least 15 forms of LGMD are currently recognized. The different forms of LGMD arise from autosomal mutations and both dominant and recessive mutant alleles have been observed. Some types of LGMD are caused by the lack of sarcoglycan, transmembrane glycoproteins in the sarcolemma. These proteins are integral components of the DAG complex that acts as a structural tether between dystrophin and the extracellular matrix. Onset in LGMD is first seen in muscles around the hips and shoulders, with slower progression than in DMD, and there is a concern for cardiopulmonary complications later in life. Overall, LGMD is less severe and less prevalent than DMD and BMD, but since it is autosomal, females are equally affected.

Beyond these examples, it should also be noted that there are a wide spectrum of muscular dystrophies that have been identified. And they do not all result in the same symptoms or severity due to a vast range of underlying causes. Several years ago it was noted that there were 34 clinical disorders that were currently under the umbrella of the dystrophies (37). There are the somewhat less severe distal muscular dystrophies like Miyoshi myopathy due to a mutation of dysferlin (38) and the tibial muscular dystrophy which has a mutation in titin (39). There are also congenital muscular dystrophies, like MDC1A that results from a mutation in Laminin $\alpha 2$ that manifests as seizures, speech problems, and contractures (37). Fukuyama CMD affects primarily populations in Japan and causes neural malformations. Still other forms like Emery-Dreifuss (EDMD) arise from deficiencies of emerin and laminin and lead to cardiomyopathy and contractures early in life. Finally I will mention myotonic (DM) that

has defects in myotinin protein kinase and ZNF9. Myotonic dystrophy has several different forms and is the most common dystrophy observed in adults (37).

Pathology

Common to many of the dystrophies associated with dystrophin (dystrophinopathies) and the sarcoglycans (sarcoglycanopathies) is an increased susceptibility to contraction induced muscle damage due to a compromised sarcolemmal integrity (Fig. 1b). As the dystrophic muscle contracts, the internal cytoskeleton (f-actin) is not structurally anchored to the muscle plasma membrane and the extracellular matrix. This structural and functional disconnect, leads to a tearing of the sarcolemma during what would normally be withstood by normal muscle (see Fig 1-1). As the damaged muscle fibers are repaired, they still lack the missing structural component and will inevitably be torn again by future muscle activity and the process will be repeated. This results in an ongoing cycle of muscle damage and repair. This is observed clinically as a rise of muscle enzymes and proteins in the blood (i.e. the m isozyme of creatine kinase) levels, indicative of damaged muscle tissue. The tears in the membrane are large enough to allow large serum proteins such as albumin and immunoglobulin into the fiber, indicating that even large proteins are able to freely transverse the normally impermeable membrane (40). When looking at histological samples, signs of tissue remodeling and regeneration are observed simultaneously with a heterogenous distribution. Regions of necrosis are also seen with vast areas of edema and immune cell infiltration. While such damage can be observed in stained tissue sections from muscle biopsies, it has been difficult to observe this increase in membrane permeability *in vivo*. Furthermore, due to the sporadic spatial and temporal distribution of muscle damage, histological lab results may not well represent the extent

of damage to the entire muscle. When it is also taken into consideration that not all muscles are affected equally, the need for a non-invasive *in vivo* detection method becomes further evident.

Laboratory Models of Muscular Dystrophy

In the laboratory setting researchers are now fortunate to have several animal models of the various forms of muscular dystrophy. These genetic models span a wide range of forms of the disease and have been developed in many different background species. The most commonly used models are murine and canine. The *in vivo* work carried out in the studies described in this dissertation was carried out using the mouse models described below.

Animal models of dystrophinopathies.

The *mdx* mouse has been used extensively as a model of Duchenne and Becker's muscular dystrophy. The name *mdx* refers to the mouse having a X-linked muscular dystrophy phenotype (see Figure 1-2) that is due to specific point mutation resulting in premature termination of translation of the protein dystrophin (41). The *mdx* mouse has a low level of revertant fibers that express low levels of dystrophin in an otherwise dystrophin null animal. This contributes to the mild dystrophic phenotype in the strain and is the factor that allows it to also serve as a model for BMD. One sizable difference between the *mdx* and human DMD/BMD phenotype is the lack of severe fat deposition in the mouse model. While this does affect the ability to directly translate some of the data from noninvasive imaging techniques described later in this chapter, this does provide a simplified model where researchers can concentrate solely on the muscle fibers themselves giving a clear view of the source of the underlying problem. Like human individuals with an X-linked mutation in the gene for dystrophin (Figure 1-1), *mdx*

mice are susceptible to contraction-induced injury during normal muscle use and also possess many of the histological changes described in humans. Mice with mutations in the dystrophin gene have also been described in the *mdx2-5^{CV}* mice, which display an increased variation in muscle fiber diameter, and in *mdx52* mice, which have large deletions in the dystrophin gene, similar to more than 65% of human patients (42). Since a mutation in exon 52 was induced, this generates a splicing error between exons 51 and 53 and as such this mouse model also lacks the shorter dystrophin isoforms Dp140 and Dp160, along with dystrophin itself (43). While 90% of the muscle fiber in *mdx52* mice had centralized nuclei, the muscle did still have a small amount of “revertant” fibers that immuno-labeled positive for dystrophin; similar to *mdx* mice (43). In addition to these *mdx* variations, there are also double mutants, like the dystrophin/utrophin null mouse (*mdx;utnr^{-/-}*), that show a much more severe phenotype. One possible explanation for the mild *mdx* phenotype is the role of utrophin compensating for the loss of dystrophin in these animals. In the *mdx;utnr^{-/-}* double mutant, both of these proteins are missing and a model with a much more severe pathology was created, replicating many more classical symptoms of the human disease. While the *mdx* mice have bouts of damage that occur early in age and then lie dormant and then gradual weakening is observed later in life, the *mdx;utnr^{-/-}* double mutant mice have a severe phenotype early on and progressively get worse. During this course they develop necrotic lesions, muscle weakening, kyphosis, contractures and fibrosis. It has therefore been argued that double mutants like this serve as a more accurate model for preclinical trials (42). Other double mutants include *mdx;adbn^{-/-}* which lack α -dystrobrevin, *mdx; α 7integrin^{-/-}* which appears to be deficient in its muscles

to regenerate, *mdx;MyoD*^{-/-} which also have a reduced capacity to regenerate and are a model of cardiomyopathy related to DMD, and finally the *mdx;PV*^{-/-} double mutant that lack parvalbumin (PV), a calcium binding protein, also displays a slightly increased severity in the dystrophic phenotype (42).

While the murine models are widely used, canine models of X-linked muscular dystrophy (CXMD) are more similar to the human disease (44-46). The most established of these is the golden retriever muscular dystrophy (GRMD) model. Though the model is much more relevant than the mice, the dogs display a higher amount of phenotypic variation (even within the same litter) and require an extensive amount of care in order to maintain (46). Early studies demonstrated that the phenotypes were much less severe in females and in smaller breeds of dog (45), but the beagle also remains an attractive model animal due to its smaller size making it easier to maintain in laboratory kennels (47). In Japan (2003), a beagle model (CXMD_J) was produced as a backcross from the GRMD model via artificial insemination (47). It was argued that the beagle's body size was more appropriate for a dystrophy model and that the milder phenotype also made it easier to care for them, as well as increasing their life span making longer longitudinal studies possible (47). Later it was reported that the symptoms in the now well established CXMD_J colony are nearly identical to those seen in GRMD, but with the added benefit of a much smaller animal (48). Finally, in 2006 Yugeta reported cardiac involvement in the CXMD_J model (49), further making it one of the more attractive animal models in use to date.

Animal models of sarcanopathies.

The BIO 14.6 cardiomyopathic Syrian hamster (50, 51) became the first animal model of human sarcoglycanopathy (specifically for LGMD2F) after it was recognized

that a mutation in the δ -sarcoglycan gene was the underlying cause of the pathological phenotype (46).

Mouse models of limb-girdle (LGMD) have been created in which specific dystrophin-associated glycoprotein null mice, such as α -sarcoglycan null (α sg^{-/-}) or γ -sarcoglycan null (γ sg^{-/-}), have been made using knockout technology (12, 13). These mouse models serve as useful preclinical tools to test various therapeutic interventions aimed at curing or halting disease progression in human. They have been successfully used to show the potential of cell therapy (14-16), gene therapy (17-19) and pharmacological interventions (20, 21) all as potential candidate treatments for muscular dystrophy.

Approaches to treatment of muscular dystrophy.

Gene therapy. In the majority of the forms of muscular dystrophy, the disease is caused by a single gene mutation. This makes the dystrophies prime targets for gene therapy strategies. There are several approaches that are under development. One approach is gene delivery. There are many strategies in the gene delivery mechanism itself. One of the most direct approaches is the direct injection of plasmids containing the full length gene into the muscle, followed by electroporation (52). In the case of DMD, it was observed that plasmid expressed full length dystrophin may have been protected for eliciting an immune response in *mdx* mice due to the life long presence of revertant fibers in the mouse model (52). While these studies were valuable proof of concept experiments, long-term expression and systemic delivery to all of the body's skeletal muscle would not be possible using this delivery method. Another promising approach is viral mediated gene therapy vectors. One limitation encountered when

dealing with the dystrophin gene is its length, spanning over 2,300 kilobases and requires 16 hours to transcribe (53). One approach to ameliorating dystrophin deficiency using smaller Parvovirus vectors is to use modified, truncated genes that, the product of which, would still functionally add stability to the sarcolemma. Examples of these include minidystrophin and microdystrophin. Adeno-associated viruses (AAV) has been successfully utilized as a vector for minidystrophin delivery in *mdx* mice and was shown to produce long term expression at least up to one year (54). Adeno-associated viruses (AAV) have also been found to be an extremely efficient tool to deliver other foreign, booster or other missing genes to specific dystrophic muscles (55-57). For instance, our group has shown that in LGMDIIa skeletal muscle can be rescued following neonatal gene transfer of human α -sarcoglycan in mice (56) and clinical trials have recently shown AAV can be a safe and effective vector for delivering the α -sarcoglycan to human muscle (58).

An indirect approach using gene therapy, is the targeted over expression of booster genes. The expression of utrophin, an autosomal homologue of dystrophin, could be an alternative approach to rescuing dystrophic muscle when the host might have an immune response to foreign proteins (59). Furthermore, it has long been suggested that expression of proteins such as agrin may also partially rescue dystrophic muscle, largely by further promoting utrophin expression (60). And finally, other studies take still another approach, such as the use of transgenic knock-in mice (*mdx:mlgf^{+/+}*) that demonstrate local over-expression of insulin-like growth factor 1 (IGF-1) increases the regenerative capacity and decreases necrosis in *mdx* skeletal muscle (61, 62); suggesting IGF-1 would also be a promising booster gene for treatment of MD. The use

of systemically delivered recombinant human IGF-1 bound to an IGF-1 binding protein 3 (rhIGF-1:rhIGFBP3; marketed as IPLEX) is currently in clinical trials for myotonic dystrophy (63).

Pharmacological therapy. Since the underlying deficiency in MD is attributed to gene mutations, many pharmacological therapies are carried out in hopes of lessening the symptoms, but fail to address the primary cause. Unfortunately, these are the most commonly applied therapies in the clinical setting. By far the most common treatment is the prescription of steroids; specifically Deflazacort and Prednisolone (64-66). In the preclinical arena and in clinical trials, several other approaches are showing promise. One area is the idea that pharmacologically reduced protein degradation would result in less muscle loss upon injury. In such a strategy, protease inhibitors are administered to promote the maintenance of muscle mass. Specifically, the Bowman-Birk inhibitor (BBIC), derived from soybean extract, has shown promise in preventing muscle atrophy after disuse (67) in healthy mice. Another pharmaceutical approach is to apply agents that promote read through of early stop codons. These compounds act similar to the antimicrobial gentamycin, but with much less cytotoxicity. One such compound that is currently in early clinical trials is PTC124. The compound PTC124 (commercially known as ataluren) is a 284 Da, achiral, 1,2,4-oxadiazole linked to flourobenzoic rings (68), which can be orally administered and promotes the expression of a slightly modified, but functional dystrophin protein via the read-through of pre-mature stop codons that would otherwise sabotage the functional expression of dystrophin. Recent studies of PTC124 in *mdx* mice show very promising results (69), as well as clinical trials for the treatment of cystic fibrosis and DMD (68, 69).

Finally, other approaches, that lie in between pharmacological and gene therapies involve exon skipping with the introduction of antisense oligonucleotides (70, 71). These methods utilize morpholinos to bind around and slice out the region where the mutation occurs in the mRNA transcript for the dystrophin gene, resulting in a truncated, but functional form of the protein to be expressed (71). There appears to be a higher rate of mutation in exons 44 – 55 of the dystrophin gene, which codes for the structurally spanning “rod” region of the protein (68). The rationale for this approach to treatment comes from observations that in-frame deletions in this region leads to the less severe clinical phenotype seen in Becker muscular dystrophy (BMD) (68). By using antisense oligonucleotides (AONs), or morpholino, to target RNA splicing, the rescued mRNA is shortened but remains in the correct reading frame. Optimizing the delivery of these morpholinos to the myonuclei has been the focus of much research, including the addition of copolymers (68, 72-74) similar to DNA transfection agents, and recombinant adeno-associated virus (rAAV) vectors (75). Clinical trials have shown promising proof of concept results in humans (76). The wide range of mutations in DMD patients may either require extremely personalized treatments (68) or we may find that morpholino cocktails may make a treatment that has a broad application (77). In order for these treatments to be clinically effective, researcher must overcome inefficiencies in delivery and in restoration to dystrophin expression (68); it is estimated that just 30% of wild type levels of expression may be sufficient to achieve this goal (78).

Cell therapy. Finally, it is worth briefly noting that there is a growing wealth of literature on studies of dystrophic tissue correction via the introduction to either gene corrected indigenous muscle progenitor cells or through delivery of exogenous cells

from a healthy donor, but an in depth discussion of this area is beyond the scope of this dissertation. Cell therapy has the benefit of potentially restoring the target tissue via *de novo* fiber formation, while gene therapies and traditional pharmaceuticals generally require the target tissue to be responsive in order for the treatment to be effective. Studies in *mdx* mice have been promising, but early trials in human patients revealed that many of the implanted cells die off rapidly (79). More recently, pluripotent cells extracted from the vasculature, dubbed mesoangioblasts, have shown great promise in engrafting and repairing dystrophic muscle in the GRMD dog (80, 81). To date, human trials have shown promise, but systemic delivery and cell survival are major hurdles that will need to be overcome to make cell transplant a viable therapy for muscular dystrophy (25). These recent developments have led to great hope within the hearts and minds of patients with neuromuscular disorders and their families. Unfortunately this also opens the door to those in desperate circumstances to seek out unproven “experimental treatments” before they have been proven safe or effective. MacReady, in 2009, discussed the ethically grey areas of an emerging trend of “stem-cell tourism,” where families will travel to regions that lack strict medical oversight or to cities where clinics provide blatantly illegal procedures (82).

Ultimately, it is thought that a combined approach using aspects of gene transfer and regulation, pharmaceutical agents and stem cells may be required for complete amelioration of the pathological manifestations of the disease.

Monitoring disease progression.

In evaluating natural disease progression and determining effectiveness of treatments in preclinical trials, the methodology can be categorized as being in one of two broad groups. The classical histology studies have been considered the gold

standard for many years and would be considered invasive procedures. In an animal model as small as a mouse, muscle histology is often a terminal end point and this limits our ability to perform truly longitudinal studies of a single muscle's recovery from damage and thus, it increases the number of animals that need to be sacrificed at each time point in such studies. In addition biopsies have a rather limited scope and often may not represent the tissue very well in dystrophic muscle (see Figure 1-3). More recently developed methods are non-invasive and they provide many advantages. These include experimental design with repeated measures on the same animal to get a true assessment of disease. Numerous functional and behavioral tests have been described and are suitable for collecting non-invasive data (83), but these do not give the precise special and structural information that can be extracted from non-invasive imaging data. As mentioned at the beginning of this chapter, these methods include computed tomography (CT; (84)), ultrasonography US; (4, 85), positron emission tomography (PET; (5)), and magnetic resonance imaging (MRI; (6)) and spectroscopy (MRS; (7)). In our laboratory's work, we have found magnetic resonance imaging (MRI) and spectroscopy (MRS) to be particularly well suited for the three-dimensional study of soft tissues such as skeletal muscle.

Magnetic Resonance Imaging (MRI)

The major advantage of non-invasive measures like MRI is that it allows the acquisition of three dimensional images at the resolution of a muscle cell, visualizing all of the muscles of the entire mouse limb, in real-time and in the living animal. At its core, MRI is a spectroscopic technique and a brief overview of a few fundamental concepts will enrich the discussion presented in this dissertation for those unfamiliar with this methodology.

Basic Components Required for MR or NMR.

The modern designs for both clinical and experimental instruments share common elements. These include a static magnetic field, electromagnetic gradient coils used for spatial encoding of the signal, a radio frequency (RF) coil to used excite and receive the NMR the signal, RF signal amplifiers used in the transmission and reception of RF pulses and the incoming signal, and a computer workstation for the operator to control the system and to transform the acquired data.

The static magnetic field is sustained by a liquid helium cooled, super-conducting electromagnet. The field strength is the strongest at the convergence of the magnetic field lines, which in the case of these cylindrical magnets, is in the middle of the bore. The field strength (B) is measured in the unit Tesla (T), which is equivalent to 10,000 Gauss (G). The static field of the magnet is termed B_0 and ranges between 0.1T and 21.1T for imaging purposes. The larger B_0 is, the larger the induced nuclear polarization and resulting signal strength will be. The majority of the work presented in this dissertation was collected at either 4.7T or 11.1T.

The Origin of the Signal.

In the presence of a static magnetic field, the nuclear spins of specific elements will be polarized in ratios that will enable us to manipulate their orientation and acquire a time dependent change in induced signal as they relax back to equilibrium. The work presented here primarily relies on hydrogen nuclei for the source of our signal. Since the hydrogen nucleus consists of a single proton, ^1H MRS and MRI are often also referred to as proton spectroscopy or proton imaging, respectively. In this simple spin system, the axis of the nuclear spins align either parallel or anti-parallel to the static

field. The relative number of spins in either orientation is given by the Boltzmann distribution:

$$\frac{N^-}{N^+} = e^{2\mu B/kT} \quad \text{[Equation 1-1]}$$

where N^+ spins in the lower quantum energy level are more frequent than the number of N^- spins in the higher energy state. This small excess of spins in the lower energy state is described by the exponential function of the ratio between the energy difference between the two states (complex term: $2\mu B$) and the product of the Boltzmann constant ($k = 1.3805 \times 10^{-23}$ J/Kelvin) and the temperature in Kelvin (T). The energy difference between the two energy states is equal to twice the product of the field strength B and the angular momentum μ of the nucleus. At equilibrium, there is a very small number of spins aligned parallel (N^-) to the Z-axis of the magnet. Thus, at the fully relaxed state, the net magnetization vector that lies on the Z-axis or the direction of the applied magnetic field and is referred to as M_z . At room temperature this holds as a good approximation for spin energy level distribution and is therefore relevant for biological samples.

The Larmor frequency.

The precession of the nuclear spin around this axis is at a rotational frequency that is determined by the Larmor equation:

$$\omega = \gamma B \quad \text{[Equation 1-2]}$$

where ω is the precession frequency in megahertz (MHz), γ is the gyromagnetic ratio of a specific atomic nucleus in megahertz per Tesla (MHz/T), and B is the magnetic field strength in Tesla (T). The gyromagnetic ratio for the hydrogen nucleus is 42.576 MHz/T.

Thus at a field strength of 4.7T, the precessional frequency of the ^1H nucleus is 200.107 MHz about the Z-axis.

The 90° RF pulse and the B_1 field.

If the researcher induces a RF pulse, transmitted perpendicular to the Z-axis, at the Larmor or resonant frequency, energy is absorbed by these specific nuclei and the net magnetization vector will be tipped into the x-y plane. The RF field results in a second magnetic field and is termed the B_1 field. There are many RF pulse sequence strategies available, but in the most elementary NMR experiment the result of an effectively applied RF pulse would tip the net magnetization vector off of the Z-axis completely into the X-Y plane. Since the nuclei have angular momentum about the Z-axis, as soon as they are tipped into the X-Y plane they continue to precess about the Z-axis. Since the orientation of the magnetization vector is brought from being parallel to the Z-axis to being in the X-Y plane, this is referred to as a 90° RF pulse. While tip angles other than 90° are commonly used for preparing the spins for various spectroscopic and imaging applications, it is always the net magnetization vector in the X-Y plane (M_{XY}) that is the source of the signal detected by the RF coil.

The free induction decay (FID).

In this simple experiment, the net magnetization vector is at equilibrium, precessing around the Z-axis and M_z is at its maximum (M_0); so initially $M_z = M_0$. The M_0 is a function of the proton density (PD) of the sample and the polarization of nuclear spin states increasing with magnetic field strengths (B_0). After a 90° RF pulse plays out, the M_z is reduced to null and M_{XY} is at its greatest. As M_{XY} precesses freely around the Z-axis, the associated changing electromagnetic field (EMF) induces current in a RF receiver coil, according to Faraday's law of electromagnetic induction. If this vector were

to remain the same magnitude and within the X-Y plane the plot of the induced current would be a *sine* wave. In the laboratory however there are multiple processes that result in the dampened sinusoidal decay in the magnitude of the M_{XY} vector over time. This signal is termed the free induction decay (FID), which contains the frequency, amplitude and relaxation information and is the phenomenon that makes MRS and MRI contrast possible.

Basic Parameters of MR.

In three dimensions a plot of the net magnetization vector, following an initial 90° RF pulse, would resemble an inverted funnel rising out of the X-Y plane, spiraling upward as it precesses increasingly tighter around the Z-axis until it reaches equilibrium once again fully aligned with the Z-axis. As described earlier, when the M_z is equal to M_0 , this spin system is at equilibrium.

Longitudinal relaxation (T_1) and pulse repetition time (TR).

Following a 90° RF pulse (Figure 1-4), M_z will be approximately zero. Over time the M_z magnetization will recover exponentially. The time constant for this recovery of the M_z is characterized by longitudinal relaxation and is called T_1 . The T_1 is a time constant that is specific to a given sample or body tissue at a specific magnetic field strength. The T_1 time constant is due to spin-lattice interactions and is also referred to as the longitudinal relaxation. In general, samples that are more solid in nature have a shorter T_1 than samples that are more fluid in nature due to these spin-lattice interactions. T_1 tends to lengthen for samples as the B_0 field increases in strength, which can make measurements at higher field strengths require a greater interval of time in between signal acquisitions in order to achieve the same initial M_0 . This interval is termed the pulse repetition time or TR and should exceed 5 to 6 times the T_1 of the

sample if no T_1 weighting is desired. Otherwise, if the $TR < T_1$, the M_z will not be allowed to fully relax to M_0 and the net magnetization vector will have less magnitude to be tipped into the X-Y plane for the subsequent signal acquisitions (Figure 1-5). Thus the reduction in signal will not be due to a lack of proton density but due to the TR being too short for complete longitudinal relaxation of the sample, resulting in signal saturation. In such a case the data would be said to be T_1 weighted.

Transverse relaxation (T_2) time and echo time (TE).

In most practical MR imaging applications there are many reasons why the FID is not directly acquired. Instead, an echo of the FID is the source of the collected data (Figure 1-4). This is partially due to limitations of common MR hardware, including the speed of signal digitization, but this can be an advantage as many useful contrast and signal selectivity methods arise by playing out other RF pulses and electromagnetic (EMF) gradients before and following the 90° pulse. There is an exponential decay of the M_{XY} vector due to spin-spin interactions, leading to the gradual loss of signal intensity, which is also referred to as the transverse relaxation. The time constant for this reduction in M_{XY} magnitude is called T_2 .

While the permanent loss of M_{XY} following the initial 90° pulse is due to T_2 spin-spin interactions, a more rapid apparent signal loss is observed. Although the B_0 field is “shimmed” or optimized for homogeneity for each sample, local inhomogeneities will cause the observed time constant of the decay of the FID to be shorter than the actual T_2 time. This observed time constant is referred to as T_2^* (“ T_2 star”) and is commonly measured using gradient echo imaging. As was mentioned above in the Larmor equation, the frequency of precession is due to the external magnetic field strength experienced by each nucleus and the magnet. As the protons interact with their

environment, including B_0 field inhomogeneities and temporal interactions with neighboring molecules, some nuclei speed up while others are slowed down. The result is a “de-phasing” of the individual spins, which leads to an accelerated decay of the original FID and each echo, this is due to T_2^* . A sample with a short T_2 may have magnetization in the X-Y plane for a long time if it has a long T_1 , but the signal will die out quickly due to the rapid de-phasing of T_2^* mechanisms. Immediately following the 90° RF pulse, the net magnetization vector in the X-Y plane is at its greatest. If a 180° pulse is applied, the investigator is able to refocus the coherent signal, producing an echo of the original FID. The period of time allotted to refocus the transverse magnetization is termed the echo time (TE). If a curve were plotted at the peak amplitudes of several echoes over time, the slope of the logarithmic function of this curve would be equal to the T_2 relaxation time of the sample. It is possible to produce a series of echoes using a train of spaced 180° pulses; such an experiment would be referred to as being multi-echo.

The TE in a simple spin-echo experiment is equal to twice the time interval between the 90° pulse and the 180° pulse (Figure 1-6). The longer the TE, the greater T_2 weighting the data will have. A simple approach to determining the T_2 of a sample is to collect series of data with a sufficiently long TR and a range of TE values (Figure 1-6). Like T_1 , samples that are more fluid and aqueous in nature will generally have a longer T_2 . Biologically, this leads to the observation that areas of fluid accumulation will be conspicuous in T_2 weighted images, having higher relative signal intensity at longer echo times than unaffected tissue surrounding them. Carr and Purcell demonstrated that if multiple 180° pulses were applied a train of echoes could be collected in a serial

manner (86). If the rf pulses applied for the 90° and 180° tip angles are not precise on multi-echo experiments, stimulated echos will occur. This can lead to an artificially high value for the calculated T_2 time constant. To correct for this, Meiboom and Gill added an additional inversion pulse to the beginning of the Carr-Purcell sequence to produce what is now commonly called the Carr-Purcell-Meiboom-Gill (CPMG) sequence (87). As such the sequence plays out as follows. First a 90° rf pulse is applied and is followed by a time τ , then a pulse less than 180° (ie 175°) is applied and then a time twice that of τ is waiting before applying a second 175° rf pulse. This serves to put in place an internal correction for what would likely be an imperfect single 180° pulse and the magnetization vector is rotated exactly into the X-Y plane. Such a sequence in spectroscopic studies can be a valuable method to verify the accuracy of *in vivo* imaging methods of T_2 calculation and water/fat content ratios.

Spatial localization of the signal.

In basic NMR studies, the signal comes from the bulk of the sample that is in range of the RF coil and has no spatial information. The ability to produce and locate spatially unique MR signals is essential to our ability to generate images. This is done through the use of electromagnetic gradients that are installed within the bore of the static magnet. During the setup procedure, the B_0 field is carefully shimmed to ensure that the sample experiences a homogeneous magnetic field. Since, according to the Larmor equation, the resonance frequency for all equivalent species of nuclei, for example the protons from the hydrogen atoms of water molecules, will all be the same. Using electromagnetic gradient coils, the local field strength is altered along a known direction using different strength gradients. This in turn creates a range of Larmor frequencies for a given species of nuclei that are arranged based on their spatial

location. These gradients are often played out along the X, Y, and Z axis of the static magnet or laboratory frame. In advanced applications, time varying combinations of these gradients give us multiple axis gradient directions.

Slice selection. Any directional gradient may be used as a slice selection gradient. For example, in a clinical body MRI this would be in the direction of head to feet. A range of resonance frequencies corresponding to the location on the sample or patient you wish to get signal from can then be selected by a frequency selective 90° RF pulse in the presence of a gradient, effectively only tipping the spins in the band of sample you are interested in. Shortly after the 90° RF pulse is over, the slice select gradient is turned off and the system returns to the base field strength and corresponding precession frequency of the homogenous B_0 field.

Phase and frequency encoding. One manner of spatial encoding of the MR signal is by shifting the phase of the of signal contribution of groups of spins in a spatially dependent manner. By applying an electromagnetic gradient at a time after the 90° RF pulse, when M_{xy} is greater than zero, frequency of precession will vary based on the hydrogen nuclei's position. Thus while the phase gradient is on, spins will either wind up faster (therefore a positive phase shift) or they will slow down (a negative phase shift). The amount that they shift depends on how steep of a gradient is being used. Many gradient strength increments are played out to get a single image. Once the phase encoding gradient is turn off, the spins return to precession at the base frequency dictated by B_0 , but they are no longer in phase with each other. The last dimension needed for making an image is often called the read gradient. This is aptly named since it is turned on during data acquisition. This has the same basic effect, of slowing one

side down and speeding the other side up, but this time data are acquired while the gradient is on (spatially encoding this direction with varying frequency). The cumulative effect of applying both of these gradients (phase, frequency) successively is that signal from any point in the plane of those two perpendicular gradient directions is unique; each having a phase and frequency that identifies it as a unique point in data space. The data space is in the time domain and is called k-space. The Fourier transform is then applied and the processed data is transformed from the time domain to spatial encoded information as an MR image. Since each pixel in the calculated image represents a three dimensional space, they are considered pixels with volume and are termed voxels.

The contrast of these images can vary greatly based on how the proton spins' net magnetization is manipulated prior to and during data acquisition. This is done with extra RF pulses resulting in spin "gymnastics" and encoding electromagnetic gradients. These basic concepts form the basis of the imaging experiments described in the chapters that follow possible.

MRI Contrast Methods.

T₁ and T₂ contrast. T₁ contrast can be generated by collecting MR data using relatively short repetition times between RF pulses that would place Z magnetization into the XY plane (typically 90° pulses). By not allowing magnetization to fully recover in the Z-axis, tissues with a shorter T₁ relaxation will appear brighter (less saturated). Therefore, tissues like adipose will then have a greater signal intensity due to their T₁ than regions of edema (long T₁).

Another contrast method based on fundamental relaxivity properties of the sample is T₂ weighting. In biological samples, high fluid retention or high lipid density will both

increase the proton density and tend to elongate the T_2 relaxation. In those cases, such areas would appear brighter in signal as compared to surrounding areas in T_2 weight images (ie $TE > T_2$). This is in contrast to solid tissues, like bone and tendon, which have a much shorter T_2 and appear darker than surrounding soft tissues ($T_2 \ll TE$) in routine clinical T_2 weighted imaging. Several approaches of exogenous contrast agents are used to enhance T_2 weighted images. One popular method is to label tissues or cells of interest with superparamagnetic iron oxide particles. The particles' superparamagnetism alters the magnetic field surrounding them and results in a loss of signal due to rapid dephasing of proximal proton spins.

Diffusion weighted contrast. Through the use of electromagnetic gradient coils, images that have contrast based on the amount of free diffusion of specific nuclei can also be generated. In the case of the work presented in this dissertation, this would be the diffusion of the protons of hydrogen atoms; largely in water and lipid molecules. To do this within a spin-echo imaging sequence, an additional set of gradients are played out on either side of the refocusing 180° RF pulse (see Figure 1-7). Much like a phase encoding gradient, this diffusion gradient changes the phase of M_{XY} spins in a location dependant manner. After a specifically determined time interval the 180° RF pulse inverts M_{XY} and then a complementary diffusion gradient returns the phases of the spins to their original state if they have not changed their location. As protons diffuse through space away from their original position, the magnitude of the refocused M_{xy} for each voxel will decrease. Thus, loss of signal following the use of a diffusion gradient sequence is a measure of free diffusion in each voxel in the direction of the spatial gradient. By comparing an image with no diffusion gradient with an image with a

diffusion gradient executed, but having all other parameters equal, a level of mean diffusion for a given area in a specified direction can be determined. This measure is then repeated in multiple directions to assess natural barriers to diffusion within the sample. These individual images would be said to be diffusing weighted because the contrast will be biased toward levels of diffusion in the sample. Parameters that are important in generating this type of contrast are the duration of the diffusion gradient (δ) and the spacing between the de-phasing and re-phasing gradient (Δ), and the slope of those gradients. The duration and spacing of the diffusion gradients are important in determining the diffusion distances that can be detected. The gradient amplitude level and rate of change in the diffusion gradients will be important in dictating the amount of diffusion weighting that occurs in the resulting image. The power levels of the diffusion gradients, in combination with the duration, are discussed in terms of a b-value, which has the units of mm^2/s^2 . As the b-value increases, there is an exponential loss of signal that corresponds to diffusion in a given direction. In order to compare samples, several indices of diffusion are calculated. The mean diffusion in all directions is estimated by an apparent diffusion coefficient (ADC). In non-homogenous samples such as biological tissues this is considered an “apparent” diffusion measurement since macromolecules and complex macrostructures hinder truly free diffusion. If the mean diffusion along the direction of the X-axis (D_x) and that of D_y and D_z (along the Y and Z axis respectively) is calculated, then the ADC is equal to the mean of D_x , D_y , and D_z . This is shown in the equation below:

$$\text{ADC} = (D_x + D_y + D_z) / 3 \quad \text{[Equation 1-3]}$$

In addition to considering the average amount of diffusion in a given region of tissue, researchers can also evaluate the shape of the space which allows free diffusion of these molecules. One such index gives us an idea as to how spherical (isotropic) or cylindrical (anisotropic) the compartments containing these diffusing molecules are. Specifically, the term fractional anisotropy (FA) is elevated if one direction of measured diffusion greatly outweighs the other two. By this definition, molecules in a spherical compartment would have a low FA. Since healthy muscle fibers are cylindrical, it would be expected to have a reasonably elevated FA as compared to many other tissue types.

Taking the elements of diffusion imaging one step further, diffusion tensor imaging can be utilized. By collecting diffusion measurements in at least six different directions, and with the option of including multiple b-values, and an image that has no diffusion weighting (A_0), a diffusion tensor and its eigenvectors (L_1 , L_2 , and L_3) and corresponding eigenvalues (λ_1 , λ_2 , and λ_3) can be calculated. In this case the ADC is equivalent to the tensor trace. The orientation of the eigenvectors for each voxel indicates the dominant direction of diffusion in that region.

Magnetization transfer contrast. MRI has been shown to be a valuable tool in the study of these neuromuscular diseases, yet current methodology falls short of directly measuring tissue fibrosis. This difficulty arises from the extremely short T_2 (88-91) associated with collagen. To overcome this investigators have utilized a technique which images the magnetization transfer of signal from a “bound” pool of water to the highly mobile bulk pool of water (see Figure 1-8) (92). Tissues containing high concentrations of hydrated macromolecules with short T_2 s, such as muscle and cartilage, experience the largest magnetization transfer effect, resulting in larger

decreases in signal intensity compared to other tissues (ie fat, blood, water). Guo *et al.* (2003) suggested that magnetization transfer contrast MRI was sensitive to an increase in tissue fibrosis in a murine model of liver disease (93). They demonstrated that the amount of magnetization transfer (4.7T) was related to the degree of liver fibrosis and the hydroxyproline content. Hydroxyproline is a modified amino acid that is almost exclusively found in collagen, making it quantitative biochemical measure of tissue collagen content (94, 95). Magnetization transfer (MT) was first measured in skeletal muscle tissue by Wolff and Balaban (1989) and it was estimated to be three times more efficient than MT in the kidney (93).

MRI of Skeletal Muscle.

Magnetic resonance is particularly suited for the study of dystrophic muscle due to its high soft tissue contrast in imaging combined with the ability to collect biochemical data from localized regions (10); thus giving detailed information about metabolism (96, 97) and tissue composition (98, 99). Many MR parameters have been investigated in various models of muscle damage and disease, including muscular dystrophy (100, 101). MRI of muscle tissue was described in early publications relied heavily on morphological differences in images to distinguish between healthy and diseased muscles (102). Later it became routine to evaluate inflammatory myopathies with contrast methods such as T_1 -weighting or T_2 -weighting, with or without short tau inversion (STIR) sequences to suppress the signal derived from fat. These methods have more recently become common practice for the evaluation of numerous inherited neuromuscular disorders (101).

During the 1980's, following studies in rat muscle by Le Rumeur *et al.* (103), Fleckenstein *et al.* demonstrated an increase in T_2 relaxation time was associated with

specific muscle activation and exercise after having human subjects perform submaximal contractions of their forearm muscles (100). Since then many reports have been made suggesting the T_2 weighted imaging is sensitive to activation and edema in skeletal muscle tissue. More recently, Frimel *et al.* demonstrated a correlation between the amount of Evan's blue dye positive staining muscle fibers and an increased T_2 relaxation in mouse soleus muscles after a weight-reloading induced injury (15), thus providing strong evidence for a connection between increased T_2 relaxation and compromised sarcolemmal integrity.

In proton MRI, the predominant source of the induced signal is from tissue water and lipid molecules. Due to the structural compartmentalization of water in different macro and micro scale features, it is understandable that water in these different environments may have different MR relaxation properties, as well as other parameters discussed later, such as restriction to free diffusion and the transfer of magnetization. While it is commonly recognized that T_2 relaxation times increase after injury and/or activation, the exact mechanisms remain unclear. Although the transverse relaxation times of healthy muscle tissue are often reported as being from a single source (mono-exponential), sharing a common decay rate, it has been demonstrated that the signal decay curve (signal intensity vs. echo time) can be de-convolved and is better fit to a multi-exponential (104, 105); assuming the original data is high enough quality(106). It is also likely that with different types of damage and differing pathologies associated with the various myopathies, that contributions of these different water compartments maybe be in unique proportions depending on the specific state of the muscle tissue. Effort has been undertaken within the research community to indentify the anatomical or

physiological origins of these specific components (discussed in detail in Chapter 4), but such assignments have proven difficult, due to the complexity of the tissue and numerous approaches to modeling the components, the exact number of components still remain somewhat controversial (105, 107). Despite the difficulty in these assignments, multi-component analysis of muscle T_2 relaxation still may provide valuable insight to the plasticity of muscle tissue following injury or during disease.

Another growing area of study in muscle MRI utilizes diffusion weighted imaging to study the organization, orientation, and other physical attributes, such as fiber diameter. This type of data has an increasing set of applications that range from describing the overall order of the spacing and orientation of myofibers, as well as complex uses like three dimensional fiber tracking. Several studies have reported the mean diffusivity (ADC) and fractional anisotropy (FA) as indicators of damage and repair in skeletal muscle (108). Three dimensional tracking of the myoarchitecture in complex regions of the body, such as the tongue (109-111) and uterine wall (112) has proven to be a valuable tool in better understanding fiber arrangement and function in these tissues. Numerous other studies have applied diffusion imaging to cardiac muscle to look at both structure in both damaged (113) and healthy (114, 115) conditions. In addition to resolving structures of complex organized tissue, like those examples above, diffusion tractography has also been used to investigate the skeletal muscles of the limbs in humans and in animal models (116-118).

An additional line of research has shown magnetization transfer contrast to be a sensitive tool in studies of skeletal muscle. Decreased muscle MT has previously been shown to occur under conditions of large fluid shifts. Yoshioka *et al.* 1994 showed an

inverse correlation of MT in muscle with free water content in exercised muscle (119). Also Mattila *et al.* (1995) found that following muscle damage in a rodent model that there are large acute changes in MT that could not be associated with fatty tissue infiltration over the time scale studied (120). Acute muscle damage is associated with muscle fiber swelling, edema, cell necrosis and regeneration. It has also been suggested that other factors such as destruction of the large protein complexes, damaged cell membranes, and infiltration of inflammatory cells could also reduce MT (121). Vahlensieck *et al.* (1999) used MT imaging to look at intramuscular tumors and observed that muscular scar tissue had a lower MTR than healthy muscle, while both had MTR values that were significantly higher than that of the tumors (122). This supports the possibility that despite collagen having a high MTR relative to most body tissues and an increase in its concentration with progressive fibrosis, that due to the higher MTR of healthy muscle, an increase in fibrosis in muscular dystrophy could result in a decrease in the MTR that is independent of an increase in water content (edema) or lipid deposition.

MRI of muscular dystrophy.

Most MR studies of dystrophic muscle have centered on the fundamental MR parameters of muscle tissue and lipid, specifically proton longitudinal (T_1) (123, 124) and transverse (T_2) relaxation (125) or morphological observations in specific case studies. Currently, much of the MR imaging of dystrophic tissue *in vivo* is carried out based on T_1 contrast. This method is particularly useful in assessing volumetric information and resolving areas of high lipid infiltration. Unfortunately, acute dystrophic lesions, due to muscle damage prior to fatty tissue infiltration, fail to be visible on these T_1 weighted images at higher field strengths (126, 127). On the other hand, acute

muscle damage (128) and inflammation (129, 130) can be easily detected based on T_2 values up to 17.6T. McIntosh *et al.* noted that dystrophic lesions are easily identifiable on T_2 -weighted images, but they did not look at quantitative measures of the transverse relaxation (125).

While several publications describe diffusion imaging of healthy and diseased muscle, none that we are aware of have addressed diffusion parameters in dystrophic muscle. All of the current articles on diffusion MRI of subjects with muscular dystrophy were focused on imaging the brain and were cases of myotonic or congenital MD (131).

A few studies have looked at magnetization transfer in dystrophic muscle. Fatty tissue deposition has complicated the interpretation of MT results in human subjects with muscular dystrophy. For instance, Schick, 1996 *et al.* found that when using a water selective imaging sequence that there was no difference in MT between affected and unaffected muscles in three patients with Erb muscular dystrophy (132). In contrast, McDaniel *et al.* 1999, not only found that in subjects with LGMD that MT was dramatically reduced in muscles with gross fatty infiltration but MT also was also reduced in muscle tissues without visual evidence of fatty infiltration (133). Overall fatty tissue infiltration is anticipated to be lesser a problem in murine models of dystrophy. Mouse models of muscular dystrophy reflect many of the hallmarks of human dystrophies with muscle fiber damage and regeneration, yet the amount of fatty tissue infiltration is not as severe (134). Thus we intended to use MT imaging as a method of detecting progressive fibrosis and muscle tissue damage in mouse models of muscular dystrophy.

Summary

The muscular dystrophies represent a devastating group of neuromuscular disorders that greatly needs clinical solutions. Research on putative treatments is moving ahead using traditional techniques, but there is a tremendous demand for more efficiency in the process of evaluation of potential treatments. Non-invasive imaging modalities like MRI can provide this much needed rapid feedback and in the process give a much clearer picture of the overall tissue with specific biochemical and anatomical data. While parameters such as T_2 , indices of diffusion, and magnetization transfer have all been demonstrated to reliably detect global changes in muscle composition and integrity, there is much room for refining the application and analysis of these imaging methodologies in order to produce a detailed assessment of the underlying pathological source of these observable changes in MR parameters. A multi-parameter approach, in which a series of such MR imaging parameters are observed within one session, would allow the consolidation of several biochemically and structurally relevant measures into a unique profile that would characterize the status of the muscle tissue. Therefore I will use a combination of multi-component T_2 , DTI and MT imaging to study dystrophic muscle.

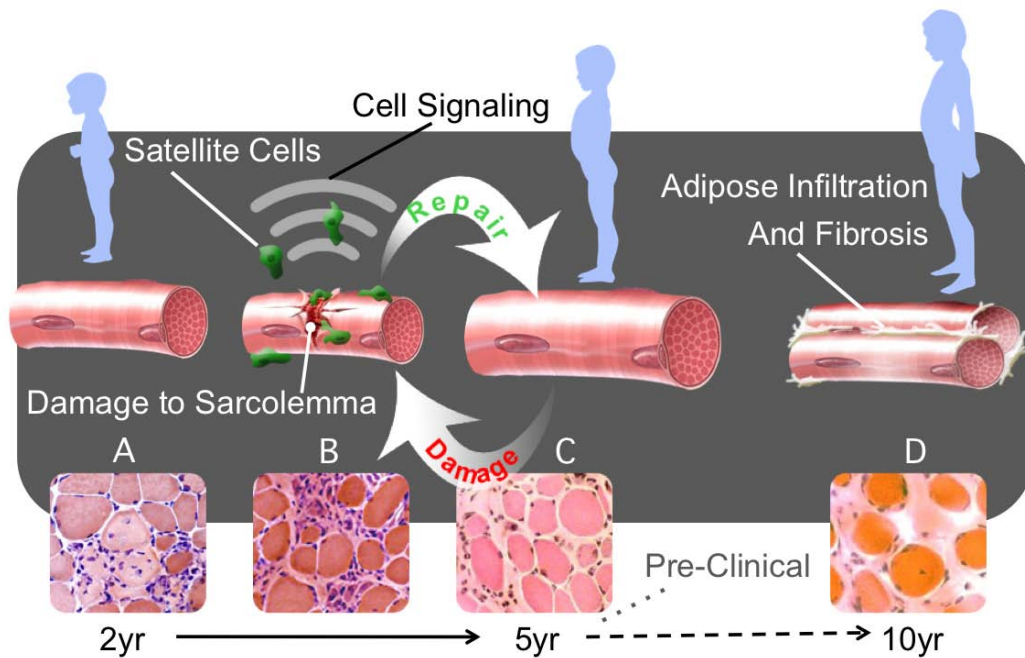


Figure 1-1. Bout of damage and repair drive disease progression in muscular dystrophy. In Duchenne muscular dystrophy, a) the absence of dystrophin results in a loss of sarcolemmal integrity. As a result, b) these muscle fibers will be damaged as the sarcolemma is compromised. The damaged cell will signal for the recruitment of satellite cells, which will home in on these chemical signals and then repair the damaged cell or they will c) form new myofibers. Since dystrophin is absent in these fibers, the newly repaired myofibers are likely to undergo damage again. This process continues to repeat until the tissue's ability to completely repair itself is d) eventually lost and the functional muscle fibers are replaced by fat and scar tissue.

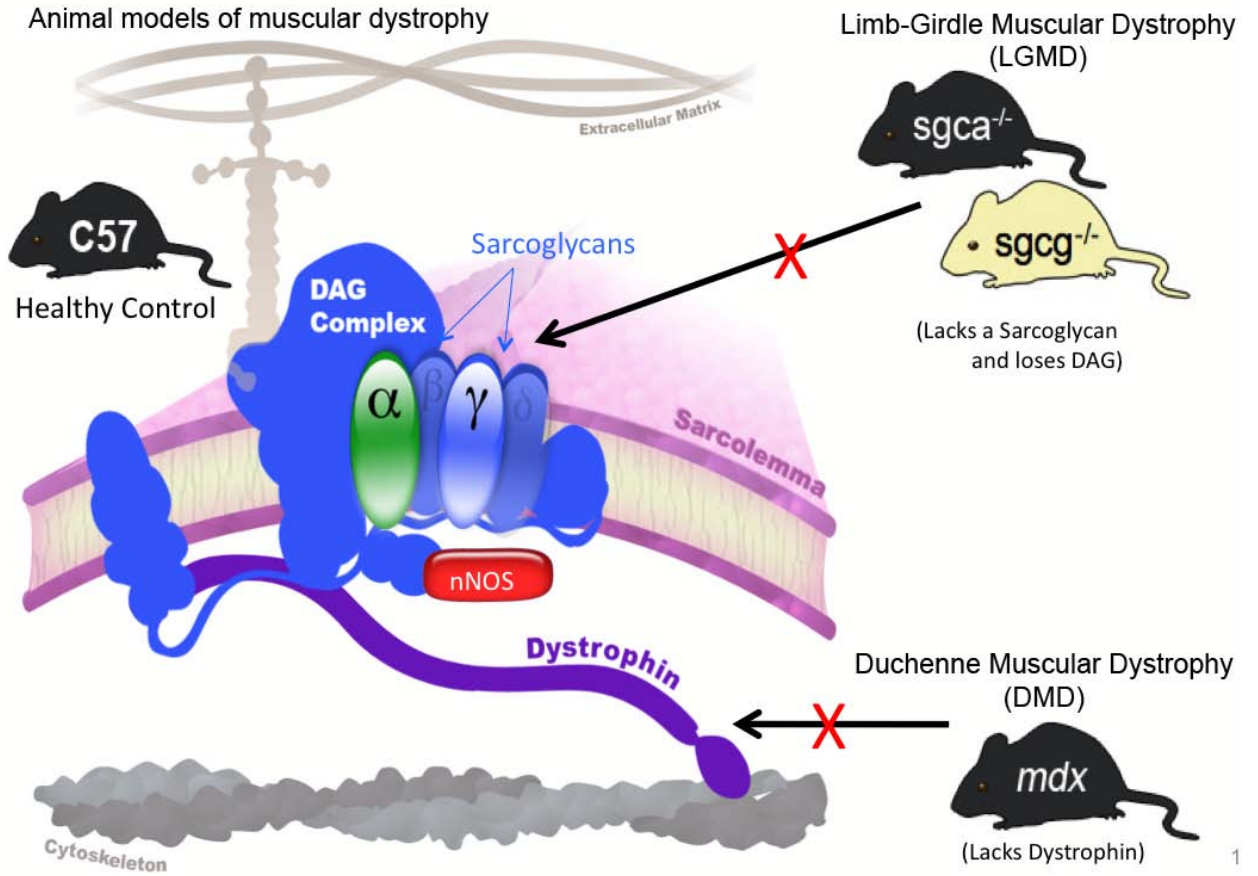


Figure 1-2. Mouse models of Duchenne (DMD)/Beckers muscular dystrophy and limb-girdle muscular dystrophy (LGMD) compared to a health C57/B10 mouse.

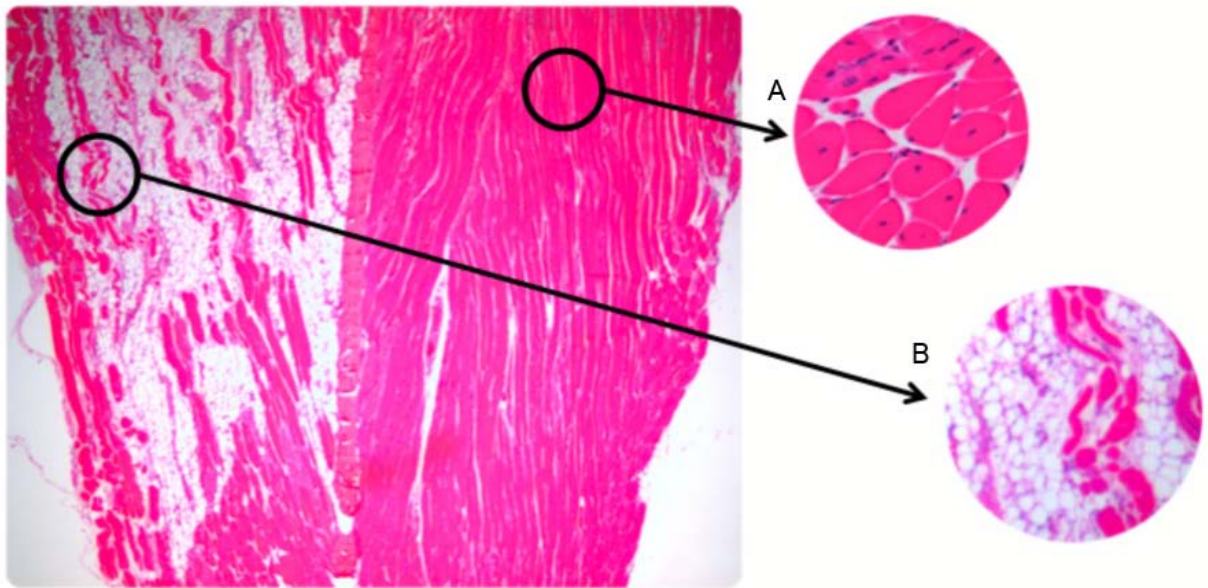


Figure 1-3. Limitations of classical invasive measures. The golden standard in pathology of dystrophic muscle has been invasive methods such as biopsy and histology of excised muscle from animal models. This image depicts typical damage observed on a dystrophic GAS muscle in a mouse model of LMGD (α -sg^{-/-}) and it is very similar to what is seen in *mdx* mice. Note the difference in disease assessment between two hypothetical biopsy locations A) a seemingly unaffected region and B) within a dystrophic lesion. This example shows the extensive muscle damage and fatty tissue deposition typically found in a 2 year old α -sg^{-/-} mouse.

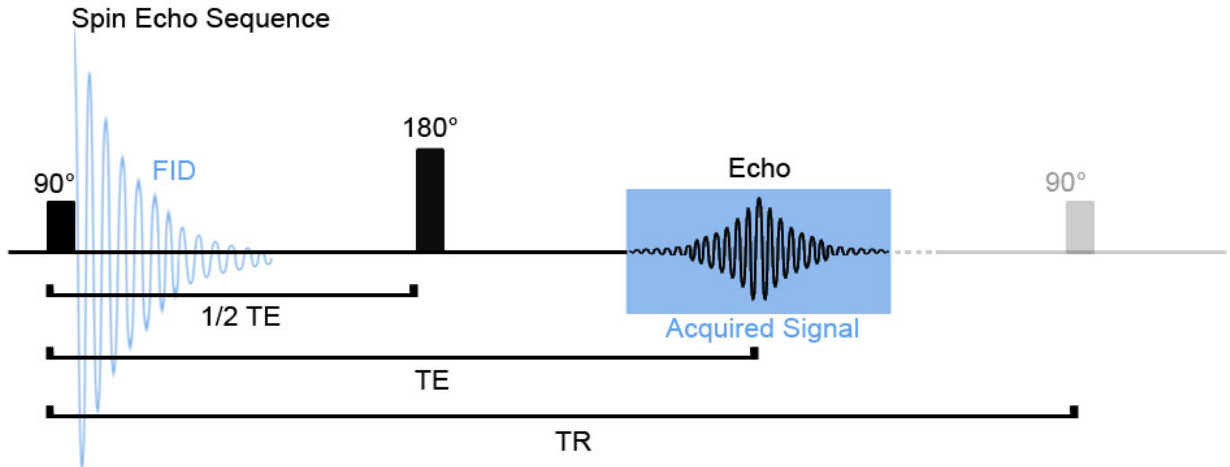


Figure 1-4. Spin echo sequence. Above is a simplified diagram of a spin echo sequence illustrating the spacing of the 90° and 180° radio frequency pulses, the free induction decay (FID) and the echo. The echo time (TE) is the time between the 90° pulse and the echo and the repetition time (TR) is the time interval in between successive 90° pulses. In a spin echo experiment, the echo of the original FID is the signal that is acquired and processed.

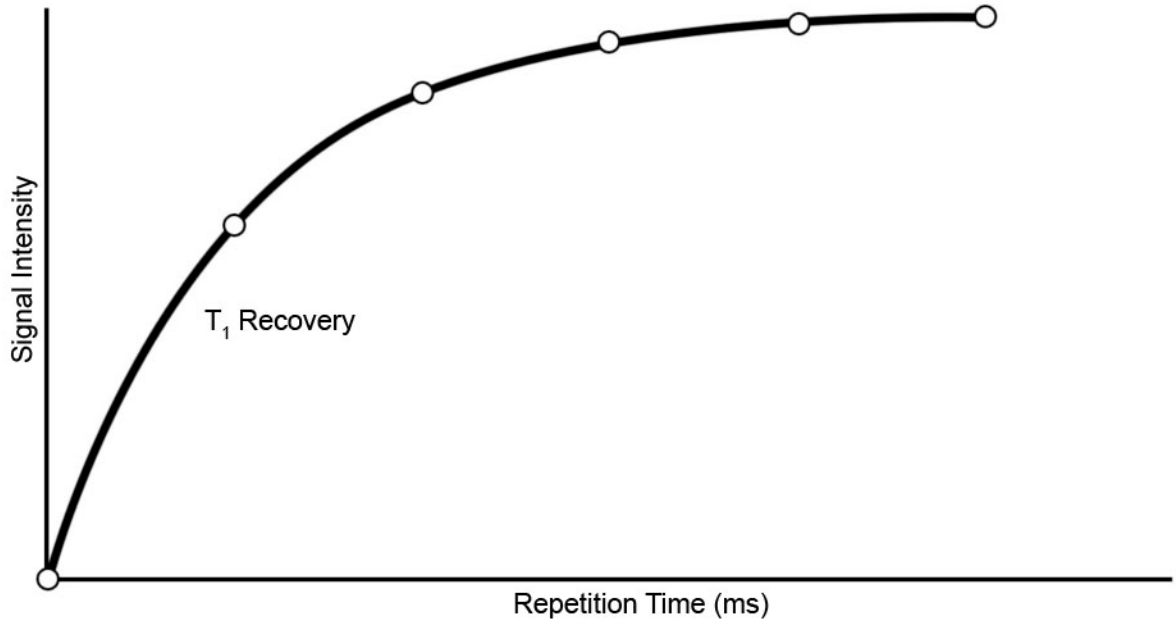


Figure 1-5. Longitudinal relaxation: T_1 recovery. Following a 90° rf pulse the M_z magnetization is reduced to zero and recovers at an exponential rate determined by the T_1 of the sample. As the time between successive 90° pulses, the repetition time (TR), is increased more Z magnetization is allowed to recover. This results in a predictive increase in signal intensity as the TR increases in length. In order to avoid T_1 weighting in collected data, a TR of 5 to 6 times the length of the sample's T_1 should be chosen. If the experimenter's aim is to achieve T_1 weighting, shorter TR times are utilized.

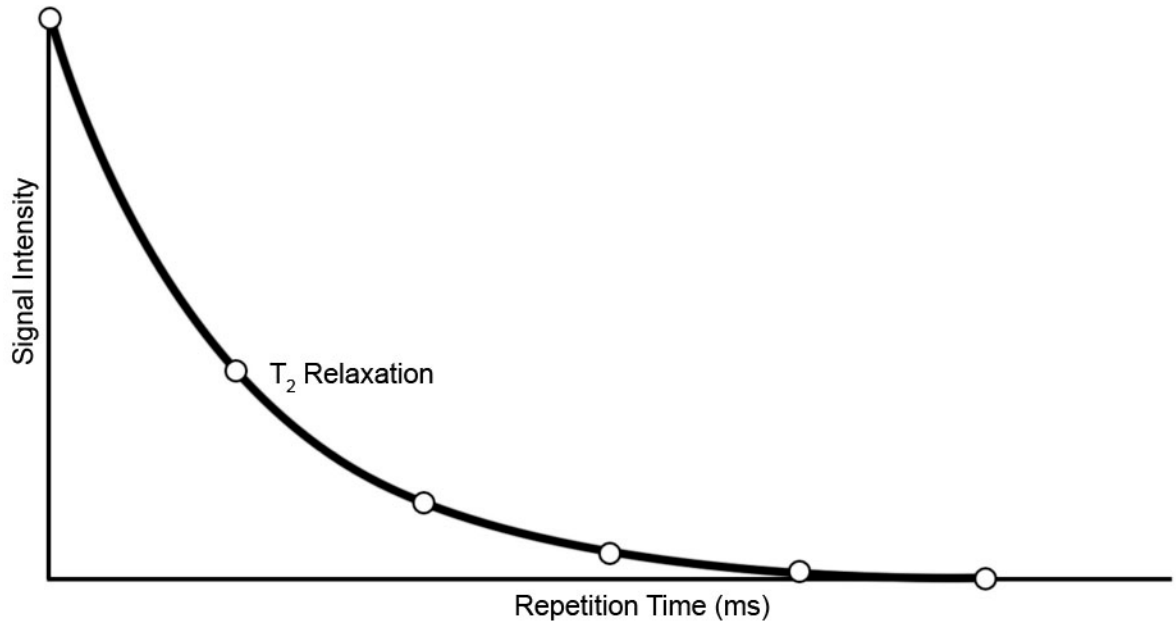


Figure 1-6. Transverse relaxation: T_2 . Following a 90° rf pulse a coherent signal is produced from the precession of magnetization in the XY (or transverse) plane. Interactions with neighboring nuclear spins results in the loss of the ensemble giving rise to precessing M_{XY} vector. These “spin-spin” interactions lead to an exponential decay of the signal acquired. As the amount of time between the 90° rf pulse and the time of acquisition of an echo, (or echo time; TE) increases, the loss in signal intensity can be seen in the plot above. The rate of this exponential decay of signal is determined by the T_2 time constant of the sample being measured.

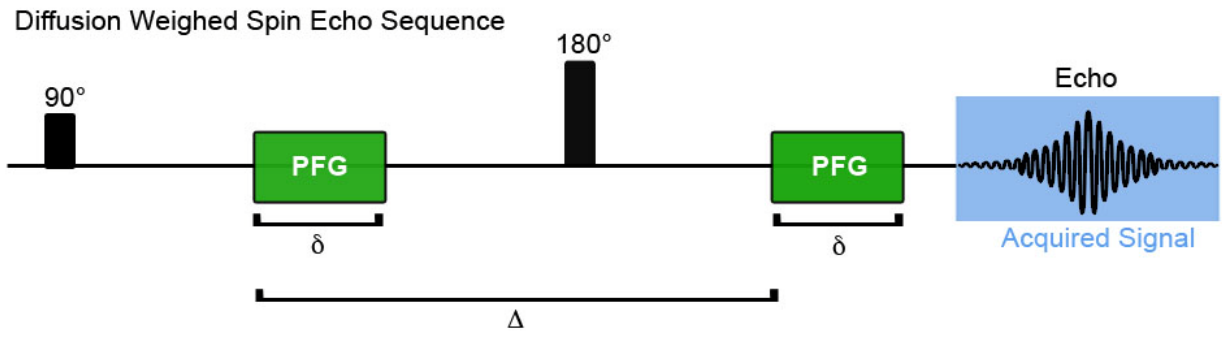


Figure 1-7. A diffusion weighted spin echo sequence.

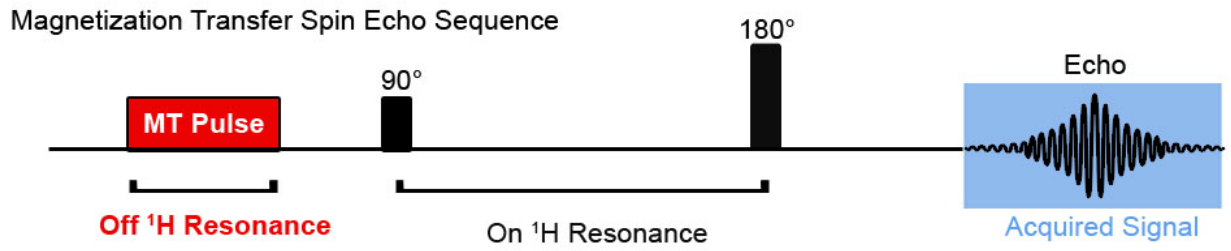


Figure 1-8. A schematic of a simplified magnetization transfer spin echo sequence.

CHAPTER 2 OUTLINE OF EXPERIMENTS

Overview

The ultimate objective of this work was to establish a non-invasive multimodal MR imaging protocol to monitor disease progression and therapeutic correction in dystrophic muscle tissue using magnetic resonance (MR) imaging. The ability to detect dystrophic pathology and its correction was investigated using three MRI contrasts methods. The first aim was to assess sarcolemmal integrity (Figure 2-1) by measuring the T_2 relaxation times of the muscle tissue. The second aim was to detect structural remodeling of dystrophic muscle using diffusion weighted MR imaging (DWI and DTI). The third aim was to determine the magnetization transfer contrast (MTC) and its relationship to fibrosis and damage in dystrophic muscle. The ability of all three MR modalities to monitor disease progression was performed by stratifying mice into both young and old age cohorts. Several mouse models of muscular dystrophy (LGMD and DMD) were compared to healthy control mice. In the dystrophic mouse models, widespread acute damage was expected in the younger animals (42), while the chronic effects of advanced disease (i.e. increased fibrosis and fat infiltration) were not yet expected. The repair pathways in these younger (4 – 8 month old) mice is in constant flux and recovery of damage is similar to what has been observed in acute models of damage in healthy control animals (135). In the aged dystrophic mice (1 – 2 years old) the acute lesions are less common, but extensive tissue remodeling and histopathology was expected (136). In order to assess the ability of T_2 , DTI, and MT to detect therapeutic correction mouse models of limb girdle muscular dystrophy (*sgcg*^{-/-} and *sgca*^{-/-}), were treated with a recombinant adeno-associated virus (rAAV) based gene

therapy vectors which lead to muscle specific expression of γ sg or α sg and were imaged using the three methods under investigation.

Global hypothesis. *Changes in the biophysical properties of bulk water can be used to monitor changes in muscle fiber integrity in dystrophic skeletal muscle.*

Experiment 1: T_2 as a Marker for Sarcolemmal Damage in Dystrophy Muscle.

T_2 weighted MR images of skeletal muscle have been shown to be sensitive to acute injury (15) and exercise induced contrast enhancement (100, 137). Elevated T_2 values may be due to an increase in tissue fluid content or decreased muscle integrity (15, 137). To investigate the changes in global T_2 as a function of long-term dystrophic disease progression, I determined the age dependent changes in T_2 of lower hind limbs in two models of muscular dystrophy and in healthy age matched controls. In order to explore the temporal evolution of changes in T_2 following injury, I utilized an eccentric damage protocol that involved downhill treadmill running. This had the effect of causing a synchronized bout of damage and provided a comparison of T_2 at various stages of injury and repair. In addition to the natural history, I compared T_2 of corrected and uncorrected dystrophic muscle with histological indices (83, 105) of muscle damage and gene expression. It is has also been well established that the MR signal from muscle consists of multiple T_2 values (105) that can be ascribed to different cellular compartments. I set out to determine whether the heterogeneity in T_2 observed within *in vivo* normal, dystrophic and corrected dystrophic muscle correlates with histological indices of muscle damage, permeability, susceptibility to injury, and edema. Finally I used non-negative least squares (NNLS) analysis (105) of multiple spin echo imaging

data collected on *in vivo* muscle to study changes of these multiple T_2 components in muscle damaged in a physiologically relevant manner.

Hypothesis 1.

T_2 weighted magnetic resonance imaging (MRI) detects muscle damage and gene correction in dystrophic muscle.

Specific Aim 1.

The primary aim of the first set of experiments was to determine the ability of T_2 imaging to detect muscle damage and monitor gene correction in dystrophic muscle. In testing this aim I specifically sought out to determine if: a) changes in muscle T_2 are related to muscle damage in muscular dystrophy, if (b) damaged muscle can be further characterized by multiple T_2 components, and if (c) changes in muscle T_2 during the time course directly following injury, reflect structural remodeling and repair of muscle tissue.

Experiment 2: Diffusion Imaging to Monitor Recovery From Damage.

Histological comparisons of dystrophic and healthy muscle reveal that there is a much greater variability in fiber size and that the presence fiber splitting (136) is found in the muscles with dystrophy. Pathological alterations such as these could potentially be detected by utilizing diffusion weighted imaging (DWI) (138). From these experiments I calculated local tissue diffusivity and fractional anisotropy. Tissue regions containing fibers with sarcolemmal damage, as well as edematous tissue, were distinguishable from lipid deposition in areas with elongated T_2 relaxation times, by comparison of the apparent diffusion coefficients (ADC). The ADC data combined with T_2 and MTR later provided a multi-modal approach to noninvasively characterize and track the stages of disease progression and therapeutic intervention.

Hypothesis 2.

The diffusion of tissue water and T₂ is altered in dystrophic muscle and related to structural changes following acute damage.

Specific Aim 2.

In this second set of experiments, I set out to determine if the diffusion of tissue water and T₂ relaxation is altered in dystrophic muscle and related to structural changes following acute damage. In exploring this aim I: a) compared the apparent diffusion coefficient (ADC) of healthy and dystrophic muscle, before, after, and during recovery from acute damage and (b) followed changes in ADC, T₂, FA and primary eigenvectors to determine if they reflect structural remodeling and repair of muscle tissue.

Experiment 3: Magnetization Transfer Imaging to Assess Fibrosis.

The build up of collagenous scar tissue between myofibers is a significant contributor to the progressive debilitating effects of muscular dystrophy (139). Not only does this fibrosis replace functional muscle tissue, but it also creates an environment that diverts muscle progenitor cells away from myofiber formation (140). Unfortunately, fibrosis can be very difficult to directly MR image due to its extremely short T₂ relaxation times (88). It has been shown that magnetization transfer contrast (MTC) allows the indirect imaging of fibrosis by looking at the proton magnetization transfer (MT) between a free liquid pool and a macromolecular bound pool (90, 92), of which collagen is a major component in fibrosis (93). In the current study, the effects of age and disease progression in the lower limb muscles of healthy, dystrophic and therapeutically corrected dystrophic muscle on magnetization transfer were determined.

Hypothesis 3.

Magnetization transfer is altered in dystrophic muscle and related to disease progression.

Specific Aim 3.

In the third set of experiments, I set out to determine the ability of magnetization transfer imaging to detect muscle damage, fibrosis and gene correction in dystrophic muscle. To investigate this I: a) initially determined the effect of age and disease progression on the magnetization transfer ratio (MTR) and (b) determine the correlation between fibrosis, muscle damage and changes in MTR in muscle tissue.

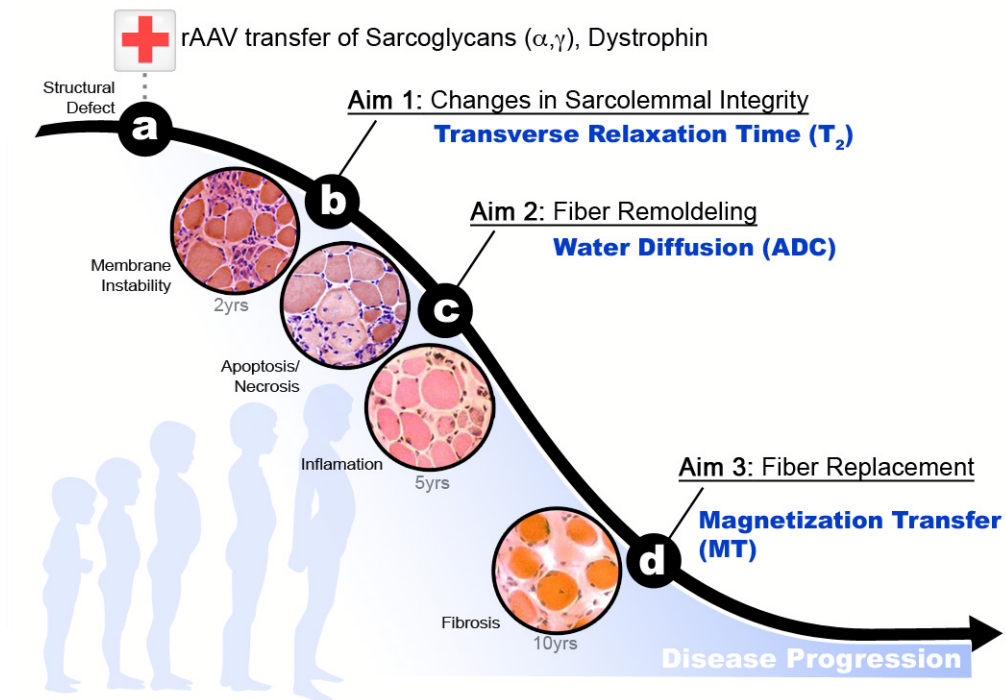


Figure 2-1. An overview of dystrophic disease progression and the specific aims of this research.

CHAPTER 3 METHODOLOGY

Animals

Rodent Handling and Care.

This study was conducted with the approval from the University of Florida institutional animal care and use committee. Mice were fed *ad libitum* and were housed in an AALAC accredited animal facility in a temperature ($22\pm 1^{\circ}\text{C}$), humidity ($50\pm 10\%$), and light (12 h light/dark cycle) controlled room. For age dependent studies, mice were stratified into two cohorts by age and by strain (Figure 3-1). Mouse strains included healthy control C57BL/10 (C57BL/10ScNJ), *mdx* a model strain for DMD (C57BL/10ScSn-*Dmd*^{*mdx*}/J), a model strain for LGMD2D (*sgca*^{-/-}) and a model strain for LGMD2C (*sgcg*^{-/-}) and are described below.

Mouse Strains

Control C57BL/10 mice. The healthy control mice used in this study were from the strain C57BL/10, specifically C57BL/10ScNJ and were obtained from The Jackson Laboratory (Bar Harbor, ME, USA). These mice have a deletion leading to the loss of a lipopolysaccharide (LPS) response (*Tir4*^{*lps-del*}), but this phenotype has no effect on the health of skeletal muscle and is therefore not relevant to this work. C57BL/10 mice served as healthy subjects and generally lived to 2 years of age if they were not sacrificed at an earlier time point.

***mdx* mice.** The *mdx* (C57BL/10ScSn-*Dmd*^{*mdx*}/J), a Duchenne/Becker muscular dystrophy model, mice were initially obtained from The Jackson Laboratory (Bar Harbor, ME, USA) and were bred in house to maintain the colony. The background strain for *mdx* mice are the C57/BL10ScSn colony, which is also currently maintained and

supplied by The Jackson Laboratory. The *mdx* strain resulted from selective breeding of a spontaneous mutation that occurred in a C57BL/10ScSn colony and was first described as a model of DMD and BMD in 1984 (41). The *mdx* mouse has a mutation in exon 23 of the dystrophin gene. The dystrophic phenotype is considered mild compared to the human disease and these mice often live to 2 years of age, but exhibit limited ambulation and kyphosis in late stages. In early stages the mice look healthy, but the muscle tissue shows signs of widespread muscle damage due to the lack of dystrophin.

***Sgca*^{-/-} mice.** The α -sarcoglycan null mice (*sgca*^{-/-}) are a model of the human disease, limb-girdle muscular dystrophy type 2D (LGMD2D). The limb-girdle muscular dystrophies arise from mutations in the various sarcoglycan genes that encode proteins that function as subunits in the dystrophin-associated glycoprotein complex. Even with dystrophin present, without one of these subunits, the remaining complex often disassociates and the function is lost. This leads to a generally more mild form of muscular dystrophy that is autosomal recessive. The *sgca*^{-/-} mice are derived from the background strain C57BL/6 and display a dystrophic phenotype early in life. While there are wide spread lesions in skeletal muscle, the mice are still able to live long lives; up to approximately 2 years of age.

***Sgcg*^{-/-} mice.** The γ -sarcoglycan null mice (*sgcg*^{-/-}) are a model of the human disease, limb-girdle muscular dystrophy type 2C (LGMD2C). The *sgcg*^{-/-} mice are similar to the *sgcg*^{-/-} in severity and their longevity. The *sgcg*^{-/-} strain has also been shown to develop cardiomyopathy and extensive muscle tissue fibrosis. The *sgcg*^{-/-} mice are chimeras that were derived genetically modified RW4 ES, which were injected into C57BL/6 blastocysts, and were then implanted into a pseudo-pregnant mother. The

RW4 ES cells were originally from the 129/SvJ strain of mouse, which have light colored coats. Thus male chimeras could be distinguished by their light color. These mice were reportedly (141) back crossed to the C57BL/6 strain and the phenotype is typically monitored by the presence of a light coat color. The *sgcg*^{-/-} strain was a gift to our laboratory from Elisabeth McNally and Lee Sweeney and our colony was maintained within our house breeding protocol.

Gene Delivery to Young LGMD Mice.

Recombinant adeno-associated viral (rAAV) vectors bearing corrective genes were delivered to the lower limb muscles of both α -sarcoglycan and γ -sarcoglycan null mice as previously reported (55, 56).

Gene delivery to *sgca*^{-/-} mice. In the case of treatment of α -sarcoglycan null mice, one-day-old *sgca*^{-/-} neonates ($n = 6$) were injected with 1×10^{11} vg of rAAV2/1-tMCK-*sgca* in one hindlimb (IM, total volume 35 μ l) and 1×10^{11} vg of rAAV2/1-tMCK-*LacZ* in the contra-lateral hindlimb (single injection per leg) (56). As the vector was injected, the needle was carefully backed out of the port of entry, from under the knee toward the ankle, in order to evenly bathe the muscles and insure maximum delivery. Initially there was concern over the possibility that the injection alone would elicit a damage response, but this did not seem to be the case. In a previous study, when the same rAAV2/1-tMCK-*LacZ*-injected *sgca*^{-/-} muscles were compared with uninjected, untreated *sgca*^{-/-} muscles, no difference was observed in the two negative control groups (56).

Gene delivery to *sgcg*^{-/-} mice. Gene delivery to the right leg of *sgcg*^{-/-} mice was achieved by IM injecting 3 week old mice (see Figure 3-2) with a muscle specific

recombinant adeno-associated virus (1×10^{10} vg of rAAV2/8-Desmin-*sgcg*; the generous gift of Elisabeth Barton; University of Pennsylvania) which expresses the human form of the missing γ -sarcoglycan (*sgcg*). The contralateral limb was not treated and served as a control. Vector diluted in phosphate-buffered saline (total volume of 100 μ l per injection) was directly injected into the lower hindlimb using a 29 1/2 G tuberculin syringe. The needle was inserted near the distal Achilles tendon and pointed upwards into the posterior compartment (GAS and SOL). Virus solution was injected while withdrawing the needle to maximize volume distribution across the lower limb. Expression of γ -sarcoglycan was confirmed using immunohistological techniques including Western blotting and immunofluorescent microscopy (described below). MR imaging of both *sgcg*^{-/-} hindlimbs was performed at 7 weeks of age (4 weeks post injection) and one year post injection.

Exercise Induced Eccentric Damage: Downhill Treadmill Running.

Some MRI methods, such as diffusion-weighted imaging, can be very sensitive to the time course of injury and recovery in skeletal muscle (78). Since the lesions in dystrophic muscle are occurring at random times, it was important to develop a protocol that would induce mild damage to the dystrophic muscle synchronized to a known time course and in a physiologically relevant way. Susceptibility to eccentric contraction induced damage has been demonstrated in both murine (142) and canine (143) models of muscular dystrophy. Since distal limb muscles of humans with muscular dystrophy are also at risk for such injuries (144), results from studies of animal models acquiring and recovering from eccentric induced damage may prove to be more relevant than other damage models. Therefore 6 *mdx* and 6 C57BL/10 mice were exercise on a

treadmill that was positioned with a declination angle of -14° (-24.9% grade), which was slightly less steep than similar protocols reported in the literature (mean declination angle of -16° with a standard deviation of 1° in studies with a similar speed) (145-147). The mice were run in individual lanes, were supervised and were encouraged, with gentle manual guidance, to run until exhaustion. At a speed of 8–10 m/min, this generally took 20–30 minutes, but a few ran as short as 10 min. After leaving the treadmill the *mdx* mice displayed outward signs of fatigue (heavy breathing and limited mobility) or until they ran for a duration of 45 minutes. For this study, imaging data were collected before running and then subsequently at time 0, day 5, day and day 10 post treadmill running. The protocol was stressful enough to elicit mild damage in the *mdx* mice, but did not damage the control C57 lower limb muscles.

Magnetic Resonance Imaging

Determination of Muscle T_2 .

Quantitative T_2 imaging was implemented to monitor muscle injury/regeneration. During all *in vivo* MR experiments animals were anesthetized using gaseous isoflurane (3% induction, 0.5–2.5% maintenance). Both hindlimbs were will imaged simultaneously using a custom built five-turn, 1.5 cm i.d. single tuned ^1H solenoid coil (200MHz) on a 4.7T Bruker Avance (Rheinstetten, Germany) horizontal bore spectrometer (Figure 3-3). To determine transverse relaxation rates (T_2), multiple slice, single spin-echo, diffusion-controlled images were acquired with the following parameters: FOV= $1 \times 1 \text{ cm}^2$, matrix= 256×128 , slices=12, slice thickness=1mm, slice gap=1mm, diffusion weighting= $3 \text{ mm}^2/\text{s}$, NEX=2 and TR=2 s. To avoid the contribution of stimulated echoes to the T_2 measurement, a Hahn spin-echo MR image sequence in which two separate acquisitions were acquired at echo times of 14 ms and 40 ms was implemented. All T_2

images were analyzed using in-house software running in the Interactive Data Language programming environment (IDL version 7.0, ITT Corp.; CO). Initially no attempt was made to determine the multicomponent characteristics of muscle T_2 . The T_2 values were calculated assuming a single exponential decay with respect to TE as previously described using the equation below (41).

$$S_{T_2map} = \frac{1}{\left(\frac{\ln S_{14ms} - \ln S_{40ms}}{\Delta TE} \right)} \quad \text{[Equation 3-1]}$$

A pixel-by-pixel T_2 map was calculated for each axial MRI. Pixels with T_2 values two standard deviations above the average T_2 value of control (C57BL/10) muscles were considered to be significantly elevated and affected by dystrophic lesions. Subsequently the mean T_2 value of the muscles of interest (TA and GAS) was determined, as well as the mean T_2 of affected versus unaffected regions. Muscle groups and affected/unaffected muscle regions were manually outlined in five image slices and the mean muscle T_2 values and the total number of pixels that were elevated were recorded.

Determination of Mean ADC at 4.7T.

Diffusion weighted imaging (DWI) was implemented to detect changes in muscle structure. As in the previous experiments, during all *in vivo* MR experiments, animals were anesthetized using gaseous isoflurane (3% induction, 0.5–2.5% maintenance). Both hindlimbs were imaged simultaneously using a five-turn, 1.5 cm single tuned ^1H solenoid coil (200MHz) and a 4.7T Bruker Avance (Rheinstetten, Germany) horizontal bore spectrometer. Data reflecting mean diffusion in the longitudinal direction (parallel to net muscle fiber orientation) was acquired with a low and then a high diffusion gradient

strength (b -value). This was followed by a separate acquisition of diffusion weighting in the axial direction to net fiber orientation (coinciding the direction perpendicular to mean fiber orientation). To determine an apparent diffusion coefficient (ADC) in the axial (with respect to the limb) and longitudinal (along the length of the limb) direction, multi-slice, single spin-echo, diffusion-weighted images were acquired with the following parameters: FOV=1.6x1.6 cm², matrix=256x128, slices=12, slice thickness=1mm, slice gap=1 mm, Δ =10 ms and δ =6 ms, NEX=3 and TE/TR = 22/ 2,000 ms. In the direction of diffusion approximately perpendicular to muscle fiber orientation, the diffusion weighting (b) for the low diffusion weighted images was $b=252.964 \text{ s}\cdot\text{mm}^{-2}$, while it was $b=912.497 \text{ s}\cdot\text{mm}^{-2}$ for the high diffusion weighted images. In the direction of diffusion approximately parallel to muscle fiber orientation, the diffusion weighting for the low diffusion weighted images was $b=260.917 \text{ s}\cdot\text{mm}^{-2}$ and $b=927.679 \text{ s}\cdot\text{mm}^{-2}$ for the high diffusion weighted images. The set of low and high b -values was different in the two directions due to differences in the strength of gradient coils in those directions. The low b -value were 50.90% of the maximal gradient amplitude, while the high b -values were 97.184% of maximal gradient amplitude. All DWI data was analyzed using in-house software running in the Interactive Data Language programming environment (IDL version 7.0, ITT Corp.). An ADC, pertaining to a single direction, was calculated assuming a single exponential decay of signal with respect to the b -value of the diffusion gradient pulse sequence and represented the linear spatial displacement of water molecules within the diffusion time Δ . An ADC map was created based on pixel changes in MR signal intensity. The mean ADC_{Slice} and ADC_{Read} values of the muscles of interest (TA and GAS) was determined, as well as the mean $ADC_{\text{Slice/Read}}$ of affected

verses unaffected regions. Muscle groups and affected/unaffected muscle regions were outlined in five image slices and the mean $ADC_{\text{Slice/Read}}$ was recorded.

Determination of ADC and FA at 11T.

Within 72 hours of collection of DWI at 4.7T, a DTI data set was collected at 11.1T using diffusion gradients capable of larger diffusion weighting (b) and shorter echo times. While the increase in field strength at 11.1T slightly shortens T_2 , the large increase in SNR was a welcome benefit for the DTI data. But more important was the ability to use the S057 (300G/cm) gradients. The high power gradient coils allowed the application of a steeper diffusion sensitive gradient which made it possible to minimize the TE to 12.8ms; reducing unwanted T_2 additional weighting (loss of signal from muscle). During all *in vivo* MR experiments animals were anesthetized using gaseous isoflurane (3% induction, 0.5-2.5% maintenance). Hindlimbs were imaged using a custom built 1 cm i.d. single tuned ^1H loop-gap coil (470MHz) and an 11.1T Magnex superconduction magnet coupled with a Bruker Avance (Rheinstetten, Germany) horizontal bore spectrometer (PV3). Optimal diffusion imaging parameters (Δ and δ) were determined empirically starting with values published in the current literature (see Figure 3-4). These data were collected with diffusion gradients applied with low b -values ($b=100 \text{ s}\cdot\text{mm}^{-2}$) and with high b -values ($b=900 \text{ s}\cdot\text{mm}^{-2}$) in 6 directions and one scan with no diffusion weighting (A_0). In pilot studies, a large range of b -values were measured and $900 \text{ s}\cdot\text{mm}^{-2}$ was chosen as the upper level of diffusion weighting as it gave best tissue contrast for damaged versus healthy muscle while retaining an adequate SNR. An example of a diffusion gradient power curve is shown in Figure 3-4, along with sample diffusion weighted images. The lower b -value of $100 \text{ s}\cdot\text{mm}^{-2}$ was chosen based on values from the literature (148). These data were processed using a

software program running in IDL (IDL version 7.0, ITT Corp.). From the diagonal diffusion elements (D_{xx} , D_{yy} , D_{zz}), the eigenvectors (e_1 , e_2 , e_3) and the corresponding eigenvalues (λ_1 , λ_2 , and λ_3) were calculated. The indices ADC and FA were determined, from which image maps were generated allowing measurement of specific regions of interest (TA and GAS) using the Paravision JIVE (Bruker Avance) software package. Statistical analyses of mean ADC were carried out to determine differences due to age and disease progression.

Great lengths were taken to ensure that there was no significant fluctuation in body temperature once the mice were in the bore of the magnet. Several approaches were tested and the most consistent solution was to circulate heated water through a custom built heating block that was installed within the cradle that holds the animal and RF coil (Figure 3-5). The core temperature of the animal was monitored using a magnet safe SAll temperature probe and the SA Monitoring system (Small Animal Instruments, Inc, Stony Brook, NY, USA). Temperature of the water bath was manually controlled so that the animals were maintained at 35°C to avoid possible changes in diffusion due to temperature and changes in perfusion due to lowered body temperature.

Determination of MTR:

MT MRI was acquired with a similar Hahn spin-echo sequence as described in the T_2 imaging experiments described in aim 1, but only consisted of a single slice. Specifically images were acquired with the following parameters: one set with a fully attenuated MT pulse (150 dB) and one with an MT pulse reference gain of 40dB (roughly twice the power of the 90° pulse), MT frequency offset equal to -10 kHz, TE/TR=11.3/2000ms, Matrix=256x128, FOV=1.6x1.6cm, and NEX=1. The power level of MT RF pulse at 40dB attenuation was chosen because this power level gave optimal

contrast between damaged and healthy muscle tissue and was well within the SAR limits that we defined. To define the pulse power ranges that were within our SAR limitations I prepared a 3% agarose (in PBS) phantom in a 1.5 conical eppendorf tube and placed an optical temperature probe in the center of the phantom. The phantom was then used to simulate the size and proton density of the animals hindlimb and a series of MTC images were collected with increasing power until the phantoms temperature was increased by 1°C; the result was a block 32 pulse with 33 dB attenuation of a 1 kW transmitter. Then one decibel of attenuation higher was defined as the maximum limit that could be applied to an *in vivo* sample of a similar size and load on the coil. A series of MTC images were then collected on healthy control mice and 40 dB attenuation was found to provide optimal image contrast in the muscle tissue and was well below half that power of our maximum SAR limit.

Magnetization transfer ratios (MTR) were calculated using Equation 3-2, with M_0 representing the scan with no MT pulse and M_{Sat} representing the image with the MT pulse on.

$$MTR = 1 - \frac{M_{Sat}}{M_0} \quad \text{[Equation 3-2]}$$

First, a MTC map was created based on individual pixel M_{Sat} / M_0 values. Subsequently, the mean MTR value was determined from the same ROI as in the T_2 maps. Mean MTR values from regions of interest in healthy, dystrophy and corrected dystrophic muscle were then compared using statistical analysis.

Measurement of Longitudinal Relaxation (T_1).

Since T_1 relaxation can be a dominant term in quantitative measures of MTR, the longitudinal relaxation rates (T_1) of dystrophic and control muscles were determined by

progressive saturation. Single slice, trans-axial images were acquired with a variable TR sequence with TE=7ms, FOV=2.4x 1.8cm², matrix=128x64, slice thickness=3mm, NEX=1 and TRs=6, 3, 1.5, 0.75, 0.325, and 0.2s. T₁ images were analyzed using Paravision 3.0.2 (Bruker Xtip) and T₁ values were calculated assuming a single exponential function. Specifically, the mean T₁ of the TA and GAS was calculated by fitting the ROI signal intensity of each muscle as a function of TR (see Figure 3-6).

Histology

Histological Verification of Sarcolemmal Damage.

Following completion of the MR experiments, all animals were euthanized and muscle tissue was collected for histological verification of the extent and regions of damage. For the detection of muscle fibers that have sarcolemmal damage, Evan's Blue Dye (EBD; Sigma) was systemically delivered to the mice following their last MRI and 24hrs prior to tissue harvest. The EBD was dissolved in phosphate buffered saline (0.15M NaCl, 10mM phosphate buffer, pH 7.4) at a concentration of 1 mg/0.1 ml/10 g body weight (41, 91). The EBD solution was then filter sterilized (2 µm pore syringe filter; Nalgene) prior to intraperitoneal injection. Within 24 hours the animal was sacrificed and the TA and GAS muscles were dissected from both hindlimbs and visualized for macroscopic accumulation of EBD in fibers and muscles. The muscles were gently stretched to resting length by dissection pins supported by dense styrofoam, coated in O.C.T. gel (Tissue-Tech), rapidly frozen in melting isopentane and stored at -80°C. Frozen muscles were subsequently cut in half and thin sections were taken at the belly of the muscle. Frozen sections (10 µm) were stained with Hematoxylin & Eosin and Oil Red O. Slide mounted sections were visualized and digitized under

brightfield at 5x and 20x magnification on a DM LB microscope (Leica Microsystems, Solms, Germany).

Histological Quantification of Fibrosis.

Following completion of the MR experiments, all animals were euthanized. The tibialis anterior and gastrocnemius muscles were dissected from both hindlimbs. The muscles were set at resting length using pins, coated in O.C.T. gel (Tissue-Tech) and rapidly frozen in melting isopentane and stored at -80°C . Frozen muscles were subsequently cut in half and sectioned at the belly of the muscle. Frozen sections (10 μm) were either stained using Masson's Trichrome Stain Kit (Richard-Allan Scientific, procedure number 010, catalogue number 87010) or Hematoxylin and Eosin. Sections were visualized and digitized under brightfield at 5x and 20x magnification on a DM LB microscope (Leica Microsystems, Solms, Germany). Digital micrograph images of the trichrome stained tissue were analyzed using the software program ImageJ (<http://rsbweb.nih.gov/ij/>). ROIs, containing the entire muscle cross section, were manually selected and the percentage of positive collagen staining tissue (based on area) were calculated using a Hue-Saturation-Intensity color model for pre- and post-thresholding measures (H:146-206, S:0-255, I:0-255; Pass Filter). In this assay, 6 muscles from each group were used and the results were then statistically analyzed using a T-test with $P > 0.05$.

Verification of transgene expression in gene delivery experiments.

In order to determine if the rAAV vectors were effective immunohistochemistry assays were conducted on excised muscle tissue. The restoration of the missing protein by viral gene delivery was assessed both by Western Blotting and immunofluorescence

microscopy of fixed tissue thin sections. The methods and validation results are reported below.

Immunofluorescence. Immunofluorescence (Figure 3-7 A) of rAAV-hSG can be seen panels to the far right (treated animals), while it is absent in the center column (untreated *sgcg*^{-/-}); wt healthy control muscle from a C57BL/10 mouse is shown in the left column of Figure 3-7 A. The transgenic human γ -sarcoglycan is labeled green. There appears to be a slight amount of nonspecific binding around areas of excessive extracellular matrix on the *sgcg*^{-/-} tissue, but this is far less than was observed in the treated and positive control animals. The primary antibody against γ -sarcoglycan was generated in a mouse (and was the generous gift of Dr. Elizabeth Barton-Davis, Pennsylvania, USA) and the secondary was goat-anti-mouse-IgG-Alexafluor488. In order to label the peripheral boundry of the fibers, the muscle thin sections were co-labeled with rabbit-anti-laminin primary antibodies and goat-anti-rabbit-IgG-Rhodamine. Thus laminin is displayed in red in the top row of merged images. The labeling was so strong that a second series of merged image without laminin is presented in the lower row so that the distrubution of γ -sarcoglycan can be seen more clearly. Finally, DAPI was mixed into the mounting media to label nuclei, which are labeled blue.

Western Blot. For the Western Blot (Figure 3-7 B) 15ug of protein per lane (using 1ug/ul, a volume 15ul of sample per lane) was run denatured on a SDS-PAGE apparatus and then subsequently blot transferred onto a nitrocellulose membrane. Since γ -SG is 35 kDa and the GAPDH (used as an internal control protein concentration) is 36 kDa, the membrane was cut in half to use two different primary antibodies. A ratio of 1:400 of the γ -SG primary and 1:5,000 of the GAPDH primary was

used. A horseradish peroxidase chemiluminescence kit (BioRad, Hercules, CA, USA) was used to auto-expose x-ray film as a method of band detection. Note that the γ -SG (35 kDa) is missing in the $sgcg^{-/-}$ lane.



Figure 3-1. Mouse age cohorts and experimental design. Group selection for (*in vivo*) age and strain dependant studies of global changes in MR sensitive parameters (T_2 , ADC, and MTC). The lower hind limb muscles of six young (age: 2-5months) and six old (age: 18-24 months) control C57BL/10SnJ, *mdx*, and LGMD II d (*sgcg*^{-/-}) mice will be imaged using MRI.

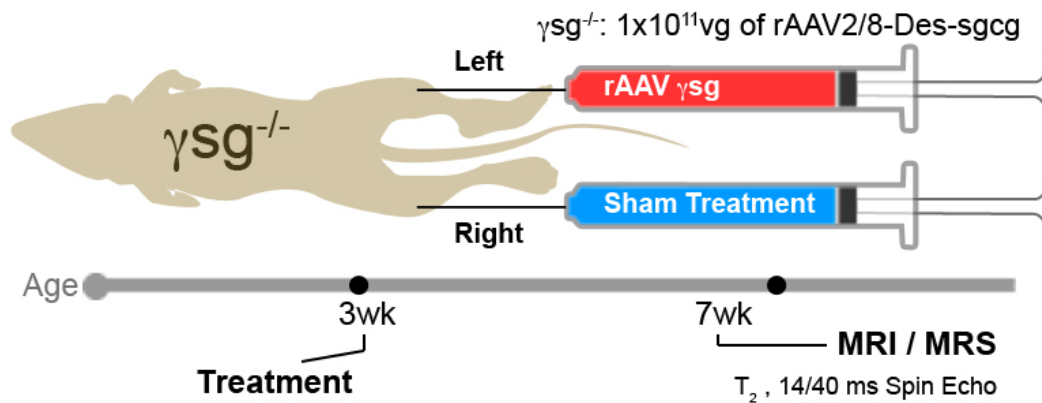


Figure 3-2. Gene correction model. Gene delivery to the right leg of *sgcg*^{-/-} mice will be achieved by IM injecting 3 week old mice with a muscle specific recombinant adeno-associated virus (1×10^{10} vg of rAAV2/8-Desmin-*sgcg*) which expresses the human form of the missing γ -sarcoglycan (*sgcg*). The contralateral limb will not be treated and served as a control. Vector diluted in phosphate-buffered saline (total volume of 100 μ l per injection) will be directly injected into the lower hindlimb using a 29 1/2 G tuberculin syringe. The needle will be inserted near the distal Achilles tendon and pointed upwards into the posterior compartment (gastrocnemius and soleus). Virus solution will be injected while withdrawing the needle to maximize volume distribution across the lower limb. Expression of γ -sarcoglycan will be confirmed using immunohistological techniques. MR imaging of both *sgcg*^{-/-} hindlimbs will be performed at 7 weeks of age (4weeks post injection).

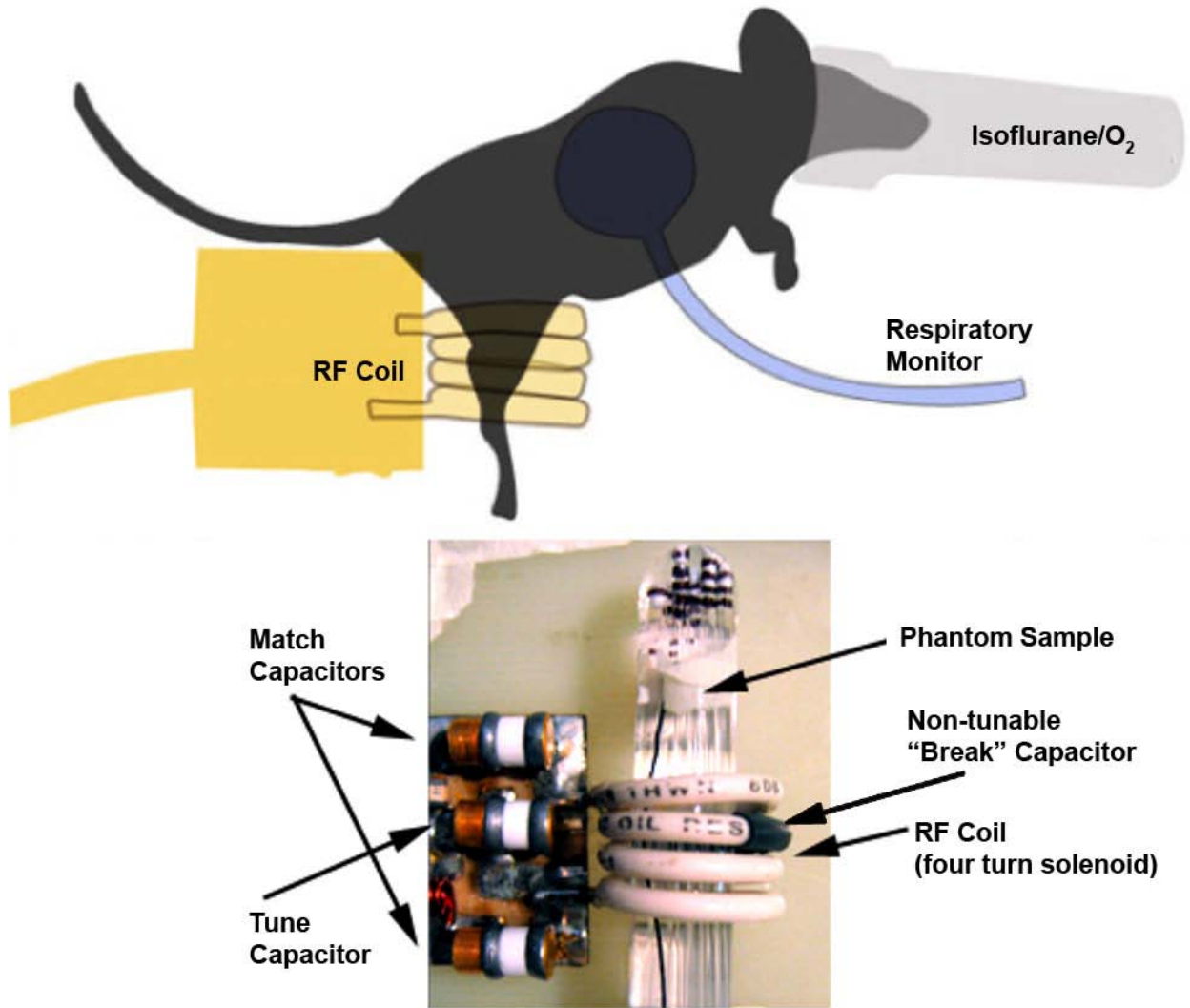


Figure 3-3. Radio frequency coil and sample positioning for MRI. A) shows the typical arrangement for *in vivo* imaging of mouse hind limbs. Both hind limbs were placed through a four-turn, single-tuned ^1H solenoid coil. The respiration of each animal was monitored by placing a pneumatic respiratory pad underneath the thoracic cavity. Anesthesia was administered through a face mask. B) Depicted in the photograph is the coil used during the experiments at 4.7T. Here a glass tube filled with capillaries containing a series of copper sulfate solutions is position for imaging. The capacitors to the left were used to tune the coil to the resonance frequency appropriate for B_0 and the ^1H nucleus. In the case where $B_0 = 4.7\text{T}$, this frequency was 200 MHz. Using a network analyzer, the match capacitors were adjusted to optimize the coil after the sample was secured in to position and reflectance was minimized in order to maximize signal in the MR experiments that would follow immediately.

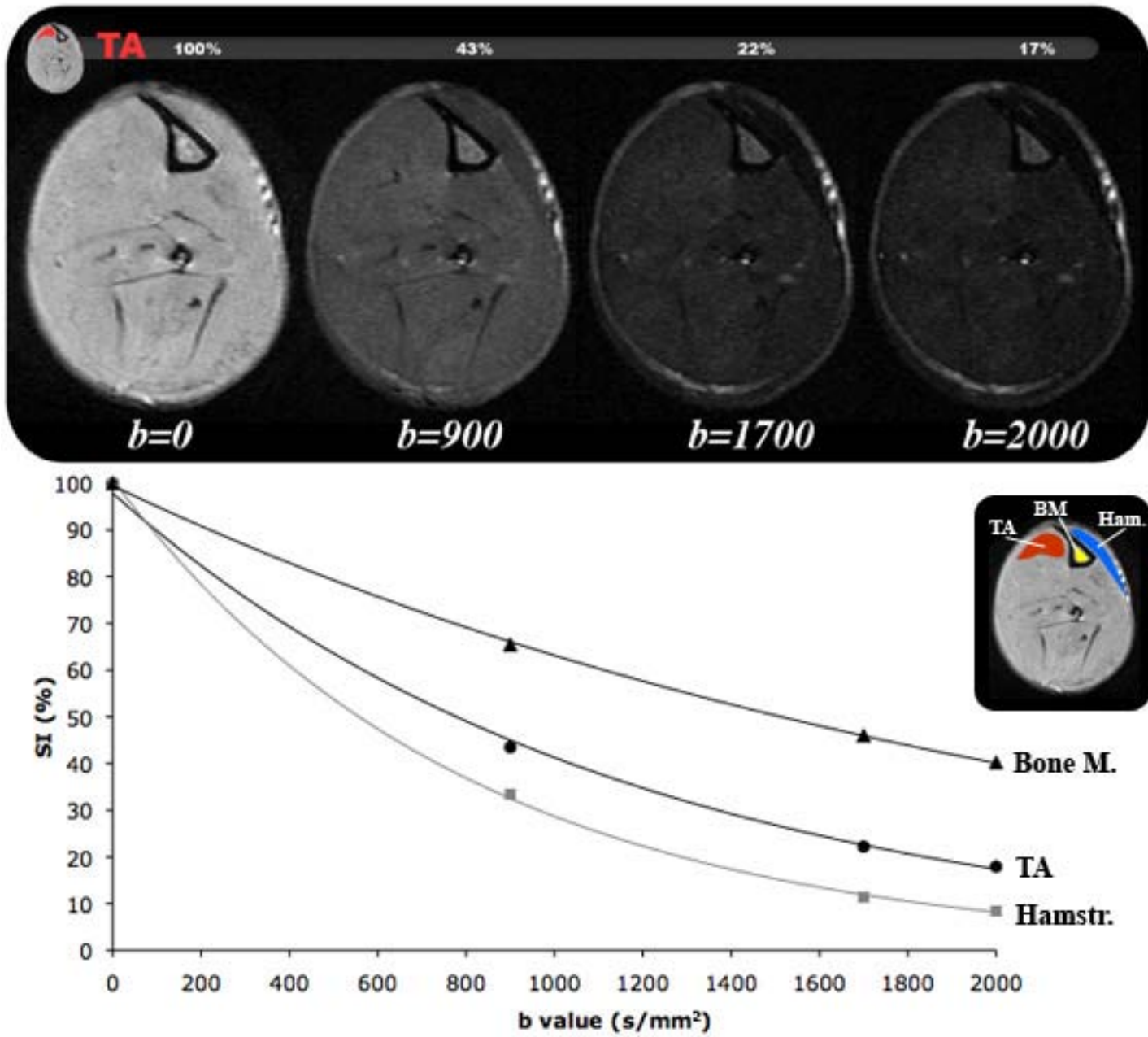


Figure 3-4. Diffusion in the plane perpendicular to net fiber orientation (axial) was determined by fitting the exponential diffusion dependant loss of signal with increasing diffusion gradient strength (reflected in the increased b value) *in vivo* at 11T. We observed an increase in SNR at this increased field strength and more powerful gradient set. Different muscles were seen to have different ADC in this direction (possibly due to fiber orientation) and lipid rich tissue was observed to have a lower ADC as we would expect (as seen in the bone marrow), reflected in the lower figure as an elongated exponential curve of signal decay with increasing b -value.

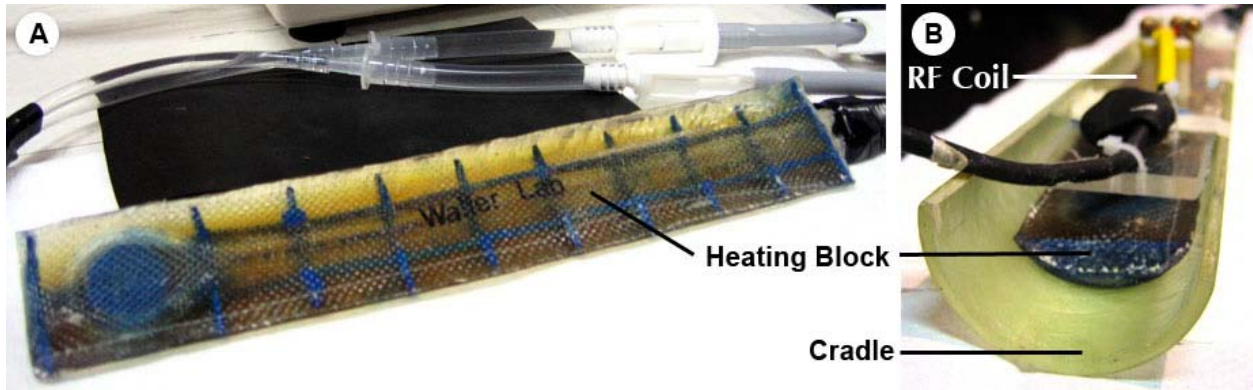


Figure 3-5. MR cradle mounted heating block. The temperature of the mice were maintained at 35°C for the duration of the DTI data collection to avoid affects of dropping temperature would have on the diffusion of water in the tissue. The system was used to circulate heated water underneath the plexi-glass plate that the animal rested on and was able to maintain the temperature within $\pm 1^{\circ}\text{C}$ for more than the total MR acquisition time of 90 minutes.

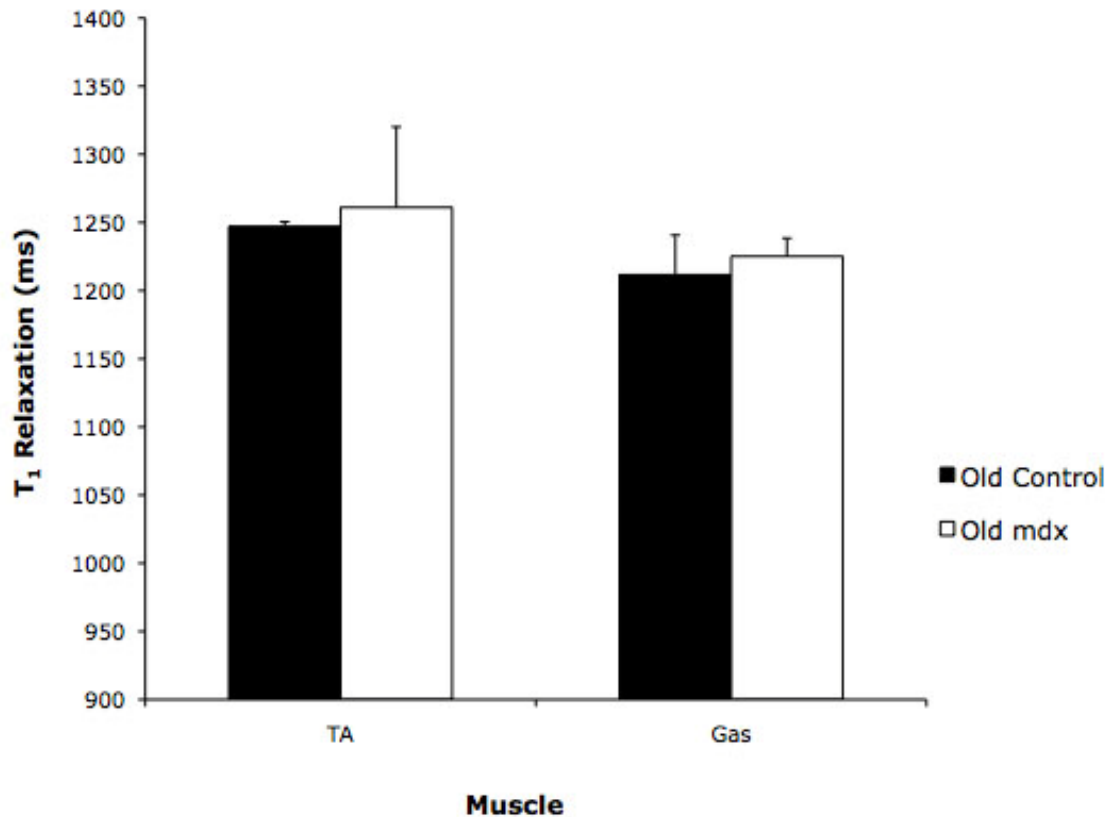


Figure 3-6. T_1 was measured in the hindlimb muscles of aged C57BL/10 and *mdx* mice. In order to determine whether there was a significant difference in T_1 between dystrophic and healthy mice progressive saturation experiments were carried out on the 4.7T magnet. A series of images were acquired each having a shorter TR. There was no significant difference in the old *mdx* vs. control GAS muscles. And while there was more variation in T_1 observed in the *mdx* than the control mice in the TA, this was less concerning since preliminary data showed that the TA was relatively protected from fibrosis and did not have a significant change in MTR in the old animal. Again this showed that the changes observed in the old GAS muscle was not likely due to T_1 differences.

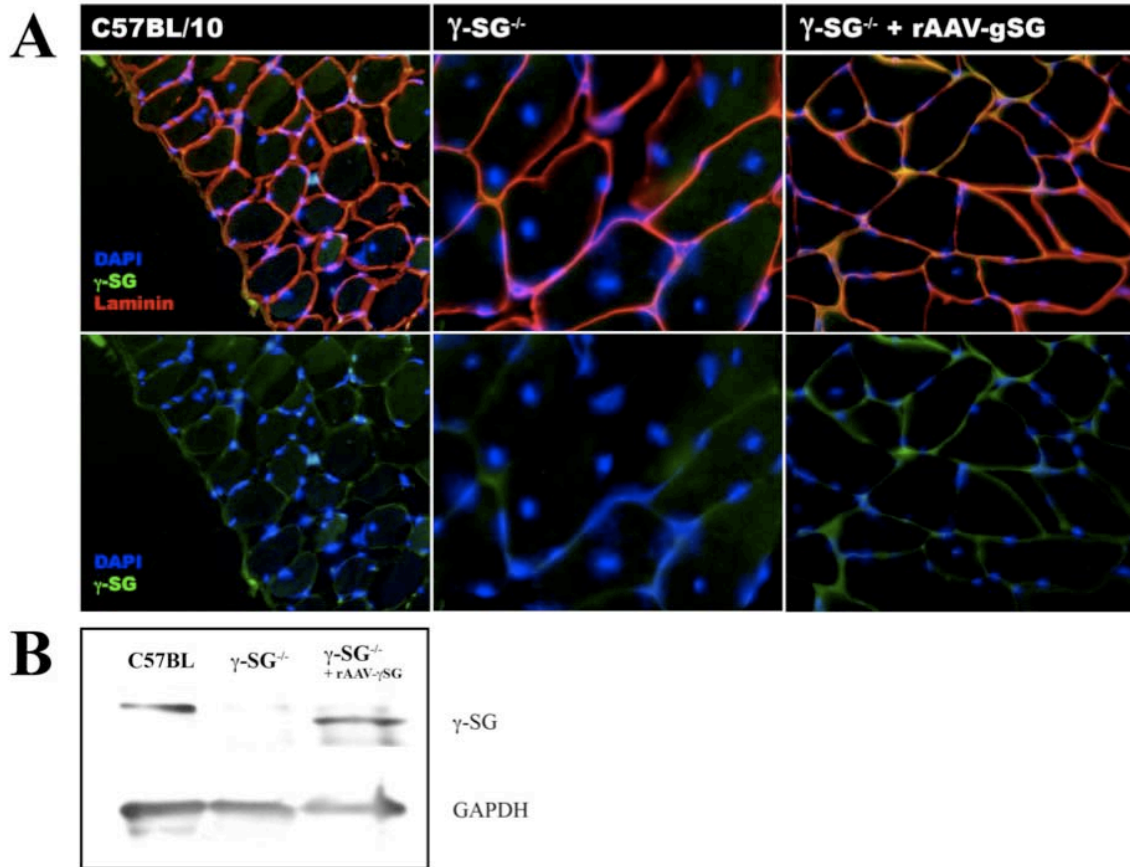


Figure 3-7. Verification of human γ -sarcoglycan expression in rAAV treated γ -sg^{-/-} mice. Immunofluorescence (A) of rAAV-hSG can be seen panels to the far right (treated animals), while it is absent in the center (untreated γ -sg^{-/-}); wt healthy control muscle from a C57BL/10 mouse is shown in the left column. The transgenic human γ -sarcoglycan is labeled green. The primary antibody against γ -sarcoglycan was generated in a mouse and the secondary was goat-anti-mouse-IgG-Alexafluor488. Sections were co-labeled with rabbit-anti-laminin primary antibodies and goat-anti-rabbit-IgG-Rhodamine. Thus laminin is displayed in red in the top row of merged images. The distribution of γ -sarcoglycan can be seen more clearly (A lower panel) without the overlay of the rhodamine labeled laminin. Finally, DAPI was mixed into the mounting media to label nuclei, which are labeled blue. For the Western Blot (B) 15ug of protein per lane (using 1ug/ul, a volume 15ul of sample per lane) was run denatured on a SDS-PAGE apparatus and then subsequently blot transferred onto a nitrocellulose membrane. Since g-SG is 35KDa and the GAPDH (used as an internal control protein concentration) is 36KDa, the membrane was cut in half to use two different primary antibodies. A ratio of 1:400 of the g-SG primary and 1:5,000 of the GAPDH primary antibodies were used. A horseradish peroxidase chemiluminescence kit (BioRad, Hercules, CA, USA) was used to auto-expose x-ray film as a method of band detection. Note that the γ -SG (35KDa) is missing in the γ -sg^{-/-} lane.

CHAPTER 4
EXPERIMENT 1: DETECTION OF SARCOLEMMA DAMAGE IN DYSTROPHIC
MUSCLE WITH T_2 WEIGHTED MRI

Abstract

The muscular dystrophies (MD) are a group of genetic diseases, which lead to progressive weakening of skeletal muscle. This weakening is due to the lack of structural proteins that protect the sarcolemma from damage during normal muscle activity. It has been established that the transverse relaxation rate constant T_2 correlates to histological measures of sarcolemmal permeability in healthy control muscle. Our first objective was to establish whether or not T_2 is also sensitive to damage in dystrophic skeletal muscle. Secondly, I explored the multi-exponential nature of the T_2 data from muscle tissue and sought to find indicators of pathology at baseline in dystrophy and within dystrophic lesions. Our results confirmed the utility of T_2 in dystrophic muscle as being a solid indicator of damage. This however can be complicated by the presents of edema and fat tissue. Multi-exponential analysis showed a novel T_2 distribution appear in dystrophic lesions, suggesting that this could be a fruitful direction of future research in trying to further characterize the anatomical or physiological source of the unique distribution peak.

Introduction

Dystrophic Muscle Undergoes Bouts of Acute Damage.

One characteristic that makes dystrophic muscle damage difficult to study is that it is constantly in the process of recovering from injury. As described in Chapter 1, the dystrophic muscle fibers are susceptible to contraction induced damage, in the case of DMD, due to mutations resulting in the absence of the structural protein dystrophin. Although initially, the regenerative capacity of the dystrophic tissue is fully in tact, the

body is ultimately overwhelmed and functional muscle mass is lost. So, even though the muscle fibers are fully repaired in the early stages of the disease, they still lack dystrophin, and will ultimately be damaged again, with what would otherwise be normal usage of the muscle. Beyond this temporal variability, there is also great spatial variance in the location of the dystrophic lesions. Seemingly random lesions can appear overnight and at any given time it is difficult to determine exactly what stage a lesion is at until a robust model is established.

T₂ Relaxation as a Measure of Muscle Damage.

The T₂ relaxation time of muscle often lengthens with exercise and is sensitive to perfusion, muscle damage, and ischemic conditions (149). Using MRI, acute muscle damage, including that of non-dystrophic muscle, is highly conspicuous on T₂ weighted images. Frimel *et al.* (2005) provided histological confirmation that significantly increased T₂ relaxation rates directly correlated with compromised sarcolemmal integrity, via Evan's blue dye (EBD) permeability assays in injured control muscle (15). EBD tightly binds serum albumin in the blood and its accumulation in fibers indicates membranes with areas with large permeability. These findings are in agreement with our observed results concerning T₂ elevation and EBD permeability in dystrophic mouse muscles (56, 150). Furthermore, the uptake of EBD can be prevented by the replacement of the missing sarcolemmal protein using gene transfer in mouse models of limb-girdle muscular dystrophy. These studies of T₂ relaxation in dystrophic muscle have proven valuable in detecting global changes in tissue damage and can consistently discriminate healthy from dystrophic muscle and corrected muscle from uncorrected, yet further refinement of scanning techniques and data analysis may yield a wealth of additional useful information about the state of the damaged tissue. For

instance, was the change in global T_2 , due to extracellular edema or increased membrane permeability? Edema was expected to be a secondary event to the loss of membrane integrity, and the focus of this sub-aim was to determine whether it would be possible to detect the loss of sarcolemmal integrity in the presence of increased extracellular water. *Therefore one of the primary goals was to determine if changes in the underlying NMR properties of water reflect changes in muscle membrane integrity.*

Multi-Exponential T_2 Decay in Skeletal Muscle.

Suggestions of multiple components of muscle water signal in NMR experiments were first made over forty years ago with the observation of multiple water line widths during NMR experiments on excised muscle (7, 151, 152). These signal components were later shown to also have unique T_2 relaxation times (153). The precise number of these components and their exact origin remains elusive and is the topic of some debate. Many researchers feel that there are at least three characteristic T_2 components in healthy muscle *in vivo*, with some papers reporting as many as five (105) and others as few as two (130). The number of T_2 components revealed by analysis in a given experiment depends greatly on the MR acquisition parameters and on the algorithm used for the decomposition of the multi-component signal. Studies that employed typical imaging sequences to assess the T_2 relaxometry of skeletal muscle often resulted in what appeared to be mono-exponential decay curves (45, 46). In general, imaging based relaxometry can be limited by the lower number of echoes that can be acquired, longer echo times required and lower signal to noise ratios (SNR) as compared to spectroscopy-based data acquisition (154). *Ex vivo* T_2 relaxation of muscle has consistently uncovered multicomponent behavior in muscle, with 3-4 components using spectral MR methods such as the Carr-Purcell Meiboom-Gill (CPMG) sequence. The

relaxation times associated with these components are generally reported to be around ~5ms, 20ms, 40ms, and 115ms (105). The shortest and longest are thought to be associated with the macromolecular bound water and the extracellular water, respectively (105). There still remains much debate and speculation over the origins of the middle components, but it is felt that they are likely related to intracellular water (105, 155). While bi-exponential models often fit the data well, they have the a priori assumption that only two dominant relaxation rates are present. A less constrained approach uses Hanson and Lawson's non-negative least squares (NNLS) algorithm to produce a spectrum of T_2 components (156). NNLS is now widely used when handling multicomponent T_2 data (105, 137, 157, 158).

Proposed Origins of T_2 Components in Skeletal Muscle.

While much effort has gone into assigning each of these relaxation components to anatomical compartments within the tissue, as described above (152), (104, 159) a few reports have presented conflicting results (103, 160) leaving the overall consensus unclear. Saab *et al.* (1999) addressed this by adding a projection presaturation to the base sequence (PP-CPMG), which nullified signal that originated from outside a cylindrical region of interest. This localized spectroscopy allowed for the collection of echoes from 1000 echo times, 1.2ms apart, with an signal-to-noise ratio (SNR) of 3243:1, of *in vivo* human skeletal muscle data and five T_2 components were resolved (105). Gambarota *et al.* (2001) conducted studies of edema in muscle tissue using CPMG imaging (99), 28) methods *in vivo* and were able to detect at least two T_2 components, which the authors suggest arise from the intra- and extracellular compartments. In that study, only the long T_2 component was shortened after a systemic delivery of the paramagnetic contrast agent Gd-DTPA. This, once again,

heavily suggests that the >100ms component originates from the extracellular water (155). Some have argued that the middle components (20ms and 40ms) may not be anatomically partitioned at all, but may be the result of multiple pools of protons undergoing proton exchange at a slow rate or magnetization transfer (105).

Interestingly, glycerin treated muscles continue to have multiple T_2 components even though they lack the outer membranous boundaries; although the muscles may have been too thick to realistically expect complete penetrance of the DMSO (107, 160). Yet following maceration, only a mono-exponential T_2 decay is detectable (107). This suggests that the origin of these middle components is likely due to anatomical partitioning of water, but that the barriers are not solely the membrane structures of the muscle tissue. Such extensive studies of muscle water compartmentalization have not been done on dystrophic muscle. *The focus of this sub-aim was to determine if the changes in T_2 components that arise due to the pathology of dystrophic muscle.*

Purpose and Summary.

In these experiments, both the age and strain dependence of mean T_2 in murine muscle were determined. Verification that measurements of global T_2 changes are a robust index of sarcolemmal damage and that this model was applicable in dystrophic muscle was then investigated. Further exploration in the ability to detect multi-exponential components of T_2 from healthy and dystrophic muscle was then tested. In order to establish confidence in the methodology, computer simulated data sets with known parameters were used to explore the limits of the protocol and analysis. Those limits were then applied and tested using phantom imaging (*in vitro*) experiments before moving onto *in vivo* subjects.

Methods

Animals.

A total of six young (age: 2-5months) and six old (age: 18-24 months) control C57BL/10Sn/J, *mdx*, and LGMD IId (γ sg^{-/-}) mice were imaged to detect global T₂ differences in lower hind limb muscles using MRI (Fig 3-1). The study was conducted with the approval from the University of Florida institutional animal care and use committee. Mice were fed *ad libitum* and were housed in an AALAC accredited animal facility in a temperature (22±1°C), humidity (50±10%), and light (12 h light/dark cycle) controlled room.

Gene Correction.

In a second experiment, an additional six 4-6wks old γ sg^{-/-} mice underwent muscle specific delivery of human- γ sg into one leg and the other leg received an intramuscular injection of the same virus encoding for a histological marker gene (LacZ; control limb). The virus that was used for gene transfer had a truncated muscle specific promoter (Desmin) and the gene was packaged into an AAV pseudotype 8/2 in order to achieve widespread expression following intramuscular injection (Fig 3-2). The mean T₂ from lower hindlimb muscles was determined as previously described in Chapter 3: Methodology. Gene expression was verified by immunohistochemical fluorescent labeling of thin cryo-sectioned muscle tissue using an anti- γ sg Ig as a primary antibody and by Western blot.

Histological Verification of Sarcolemmal Damage.

Mice were injected after the last imaging session with EBD and 24hrs later the lower limb muscles were extracted and examined for macroscopic accumulation of EBD

in muscle groups and fibers followed by detailed histological examination (see Methodology) to determine membrane and muscle damage. In addition to assessing EBD, thin-sectioned muscle was also stained with Hemotoxilin and Eosin. Histological results were then compared with mean T_2 measures determined from *in vivo* T_2 weighted MRI data.

Non-Negative Least Squares (NNLS) Analysis of Multicomponent T_2

Computer simulations. A series of computer simulations were implemented in order to test the theoretical limits of our implementation of the T_2 -NNLS algorithm utilizing an in-house software program (a modification of BVLS; graciously distributed by M. Cappellari at <http://www-astro.physics.ox.ac.uk/~mxc/idl/>), running in the development environment IDL (ITT; Boulder). These simulations were used to determine parameters such as the number of points (echo times) needed, acceptable levels of signal to noise (SNR), optimal spacing (in time) of echo times, and how those parameters effect the programs ability to resolve multiple decay components. Specifically, simulated complex decay curves having components with T_2 times of 5ms, 20ms, 40ms, and 100ms, and weighting factors that made each one similar to observed fractions in published studies of muscle tissue.

Phantom imaging. In the next step, the ability to resolve 5ms, 20ms, 40ms, and 100ms components in phantoms, consisting of different concentrations of CuSO_4 . Solutions of increasing concentration of CuSO_4 are known to shorten T_2 relaxation as compared to that of the pure solute, water. This provided a simplified multi-component sample, simulating muscle tissue, with discrete T_2 components, the relaxation of which that could be individually imperially measured. The tissue phantom was imaged at 200MHz using a single slice multiecho sequence (with an appropriate crusher sequence

(88) to reduce stimulated echoes) with various echo time spacing and signal averaging. These experiments were also used to explore the machine/sequence limitations of detecting multiple components.

Results

Assessment of Acute Damage in Dystrophic Muscle Using T₂-weighted MRI.

To evaluate acute muscle damage and dystrophic pathology, the transverse relaxation time constants (T₂) of the muscle tissue were used as a noninvasive measure of acute muscle damage. T₂-weighted images from hindlimb muscles of young control and dystrophic mice are shown Figure 4-1A. Young animals were chosen because there is a greater level of acute muscle damage in younger dystrophic mice. As was expected, a homogeneous distribution of T₂ contrast was observed in control hindlimb muscles. On the other hand, the muscles from *mdx* and γ sg^{-/-} mice were characterized by contrast heterogeneity of the T₂-weighted images. The elevated T₂ seen in the younger dystrophic muscle subsides later in life, but the transverse relaxation, while not significant, show a slightly elongated trend as compared to the age matched controls (Figure 4-1B). The T₂ heterogeneity seen in the muscles of the young mice, is due to the presence of dystrophic lesions and is thought to be representative of acute damage to the sarcolemma of muscle fibers and edema formation. This damage has been verified histologically by others (56, 150, 161) and can be seen in our work in Figure 4-2, by the presence of heterogeneous fiber diameter and central nuclei on H&E stained sections and the clumped distribution of Evan's Blue dye positive fibers in the dystrophic muscles on the bottom panel of the figure. These results show that T₂-weighted MRI is a useful marker of acute muscle damage as has been reported by others (162). Furthermore, the results of the T₂-weighted MRI experiments provided guidance in

determining regions of interest (ROI) for the magnetization transfer studies in chapter 6 and was integral to the interpretation of those results.

T₂ MRI: Detection of Gene Correction

In the LGMD gene correction studies, histological evidence of corrective gene expression and T₂ values restored to normal levels (Figures 4-3; and 3-7) was seen. In a study published by Pacak *et al.* in 2007 (Figure 4-4A) shows an typical example of the effectiveness of the viral delivered gene treatment (56) and our ability to detect the prevention of pathological lesion formation using T₂ weighted MRI. The limb on the right (mouse's left) expressed the recombinant α -sarcoglycan protein and was nearly completely free of dystrophic lesions, while the contra-lateral limb displayed lesions typical of a young dystrophic animal. Figure 4-4B illustrates the degree of severity of the untreated limb and emphasizes the level of rescue provided by the therapeutical gene expression by rendering the regions, in 3D, of each limb with elevated (twice the standard deviation of healthy muscle) T₂ relaxation times. Figure 4-4C (56) shows quantitatively that the T₂ relaxation times of muscles in both the anterior and posterior compartment were returned to values of healthy muscle in the treated limb. These results remained stable for the duration of the experiment (56) and were followed out to 13 weeks (Figure 4-4C).

NNLS Analysis of Multicomponent T₂

The ability of the non-negative-least-squares (NNLS) program to resolve distinct populations with differing T₂ relaxation times is dependent on the number of points sampled and on the ratio of the signal to background noise (156, 163). The increased heterogeneity of untreated dystrophic muscle T₂ is clearly seen by a rightward shift (increasing signal intensity) of histogram plots of signal intensity in T₂ weighted images

as compared to seemingly healthy, treated muscle (Figure 4-5). In addition to this rightward shift, the untreated muscle histogram also typically has a broadening and a right leaning shelf (elongated T_2) that is suggestive of at least a bi-modal distribution (Figure 4-5). Our computer simulations took into account these parameters and allowed us to define the theoretical limits of the NNLS analysis within the constraints of our proposed experiment. Iterative mono-exponential curve fits were run and followed by NNLS analysis on simulated signal intensity (SI) data points as a function of various distributions of echo times. Emphasis of these simulations was on the resolving power of the NNLS and the effects of various weighting of each simulated component. Three components 20 ms and 40 ms in healthy muscle, observed at 1.89T (105), and 100 ms in damaged muscle, observed at 7T (130), were selected based upon the literature; T_2 would be expected to shorten as B_0 increases. An example of such simulated data is shown in Figure 4-6. Given 1,000 echo times, evenly spaced, the 3 components were resolved (Figure 4-6; lower panel). Adjusting the weighting of each component resulted in less predictable amplitudes and widths of the distribution. These limits were then empirically verified by carrying out NNLS analysis on MR data collected on CuSO_4 phantoms of known concentrations and relaxation times. Example data from one of the CuSO_4 phantom trials is presented in figure 4-7. CuSO_4 concentration of 30 mM and 50 mM were chosen for the multiple exponent ROI since their T_2 relaxations of 25 ms and 40 ms, at 4.7T were similar to those (proposed intracellular) components found in skeletal muscle (105) that would 1) be necessary to resolve while being so close together (as opposed to a 100 ms component which is easily resolved) and 2) relevant to changes in sarcolemmal integrity and muscle damage. While the NNLS analysis of

the multi sample ROI was able to identify both known components, the integral of the distribution of each peak did not reflect the portion of the ROI that was responsible for each T_2 relaxation time (50:50). In NNLS analysis of dystrophic muscle *in vivo*, we detected several of the T_2 components that have been reported by past researchers (Figure 4-7). With the current design, it was unlikely that the <5ms component could be observed, although it is possible that it was shifted into the 10 ms. The >100ms component was likely seen in muscle that is damaged and has edema (Figure 4-6). While the middle relaxation components varied greatly depending on the degree of disease, they were possibly the most revealing of the state of the myofibers. As we would expect, a long T_2 component arose in ROIs that were sampled within regions of dystrophic lesions (Figure 4-7C).

Discussion

T_2 weighted MR images of skeletal muscle have been shown to be sensitive to acute injury and exercise induced contrast enhancement. Elevated T_2 relaxation times may be due to an increase in tissue fluid content or decreased muscle integrity. It was important for us to establish normalative data of the changes in global T_2 as a function of dystrophic disease progression. The age dependent changes in T_2 of lower hind limbs in two models of muscular dystrophy and in health controls were determined. The elongated T_2 time of the skeletal muscle in the young mice was indicative of the active bouts of damage that is observed at that age in dystrophic murine models. Indeed, these increased T_2 relaxation times had a high degree of agreement with classical histological measures of sarcolemmal integrity (or lack there of; presence of Evan's Blue positive fibers) and pathological morphology (i.e. central nuclei, variable fiber diameter, etc.). This further supports T_2 relaxation and T_2 weighted imaging as a robust

marker of sarcolemmal damage in dystrophic muscle tissue and allowed its use as a reference to identify affected (dystrophic lesions with elevated T_2) versus unaffected (seemingly healthy muscle) when comparing other contrast methods and MR parameters in future chapters. The observed decline in T_2 with age (>1.5 years) in all animals could be due to changes in activity, declining muscle growth and/or a general increase in connective tissue and reduced hydration. In the dystrophic mice, we expected that this reduced T_2 may be associated with the development of fibrosis, a topic addressed in Chapter 6.

In addition to investigating changes in T_2 with age and disease progression, a comparison of T_2 relaxation of corrected and uncorrected dystrophic muscle was made with histological indices of muscle damage and gene expression in a model of therapeutic correction. Immunofluorescence microscopy, in the case of both α -sg and γ -sg restoration to their respective sarcoglycan null LGMD mouse models, confirmed that the rAAV gene delivery was extremely efficient and that the protein was properly localizing with the inner membrane surface. In 2007, we published the use of T_2 weighted MR in tracking this successful rAAV treatment in α -sg^{-/-} mice. The ability of T_2 weighted imaging to quickly identify the lesions in the untreated limb and verify the overwhelming efficacy in the treated side is a beautiful example of the value of T_2 as a marker of muscle damage in aiding the preclinical development of a therapeutic agent for MD.

While T_2 weighting clearly allows us to define regions of unhealthy muscle, the many possible underlying sources of alteration to the signal decay make it difficult to specifically identify the nature of the underlying pathology. Due to inhomogeneous water

and lipid distribution and possibilities of differential water compartmentalization, damaged muscle tissue gives rise to an MR signal that was likely the resulting sum of multiple pools of spins having differing transverse magnetization relaxation rates. On the surface this can make the task of deciphering the precise source of a change in the calculated T_2 time ambiguous. However, when a multi-component analysis algorithm such as non-negative least squares (T_2 -NNLS) is considered (105, 130, 137), the decomposition of the multi-exponential data resulted in a unique characterization of damage; in our case lesions had an additional long component (Figure 4-7C), similar to those described by Fan *et al.* in edemas skeletal muscle (130). While a change in the profile of T_2 components may yield additional information about the nature of a lesion in the future, as we saw in the simulations and CuSO_4 phantom studies, the amplitude and peak width of the T_2 component on the NNLS spectrum may not reflect the volume of anatomy or group of spins that you may try to assign to each component. As mentioned earlier, Fan and Does (130) discussed the complex effects of exchange between pools and diffusion may have on the apparent T_2 of each component. To resolve these questions further work should be carried out in future studies that are beyond the constraints of this dissertation. Within the multicomponent analysis, T_2 relaxation may still have a good deal of information to tell us about the dynamics of injured and healing muscle tissue. In particular it would be informative to explore changes in the T_2 components following bouts of synchronized damage, as described in the next chapter, and following individual lesion over time during the course of repair. This would reduce variation in measures and provide a known time course to begin constructing a relevant model of changes in T_2 during tissue remodeling. In addition, such a model could be

further explored by the introduction of compartmentally restricted contrast agents, using a pre/post imaging strategy. Thus the researcher may be able to manipulate the relaxation of a single component in the NNLS spectra with an agent confined to a known anatomical compartment.

Changes in mean global T_2 have been solidly established as a robust indicator of sarcolemmal integrity and in this study, this has been extended to dystrophic skeletal muscle. Furthermore, we have established that there is a slight decline of T_2 relaxation times with age, but that it is only significant when comparing young versus old dystrophic mice. This may be due to the greatly elevated T_2 seen in young muscle, simply returning to a value that is closer to healthy muscle as the period of widespread recurring lesions subsides in these mouse models. Despite the reduction of T_2 lesions after one year of age, histological studies suggest that other pathologies are continuing to develop as the dystrophic mouse grows older. It is likely that T_2 will be best used in combination with other modalities since pathological factors such as edema and fat infiltration can remain ambiguous with just T_2 measurements alone. As such, it is important for us to explore other non-invasive parameters to monitor disease and recovery in muscle, in order to produce a more complete profile of a given muscle condition, especially for the purpose of aiding the development of new treatments for neuromuscular diseases.

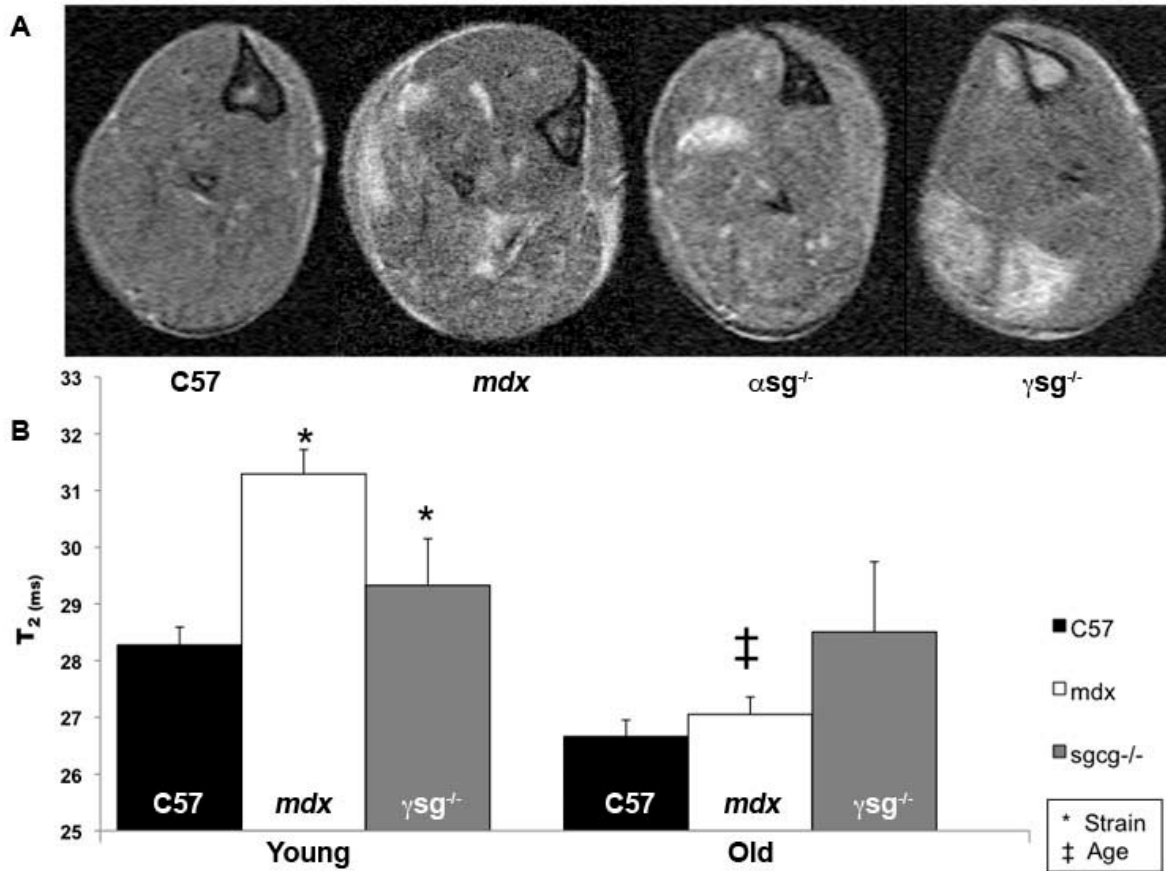


Figure 4-1. T₂ weight assessment of damage in young and old *mdx* muscle. T₂ weighed axial MRI of the lower hindlimb of young (2 – 5 mo) control C57BL10, *mdx*^{-/-}, *asg*^{-/-}, and *gsg*^{-/-} mice. (a) The muscles of the young dystrophic mice show regions of acute damage as bright lesions in these T₂w images (TE/TR = 40ms/2s). The mean T₂ relaxation times in all mice declined with age and the T₂ of dystrophic muscle was generally elevated as compared to age matched controls. In the gastrocnemius muscle of young *mdx* mice (b), the mean T₂ values were significantly longer than those of age matched controls and longer than the older *mdx* age group.

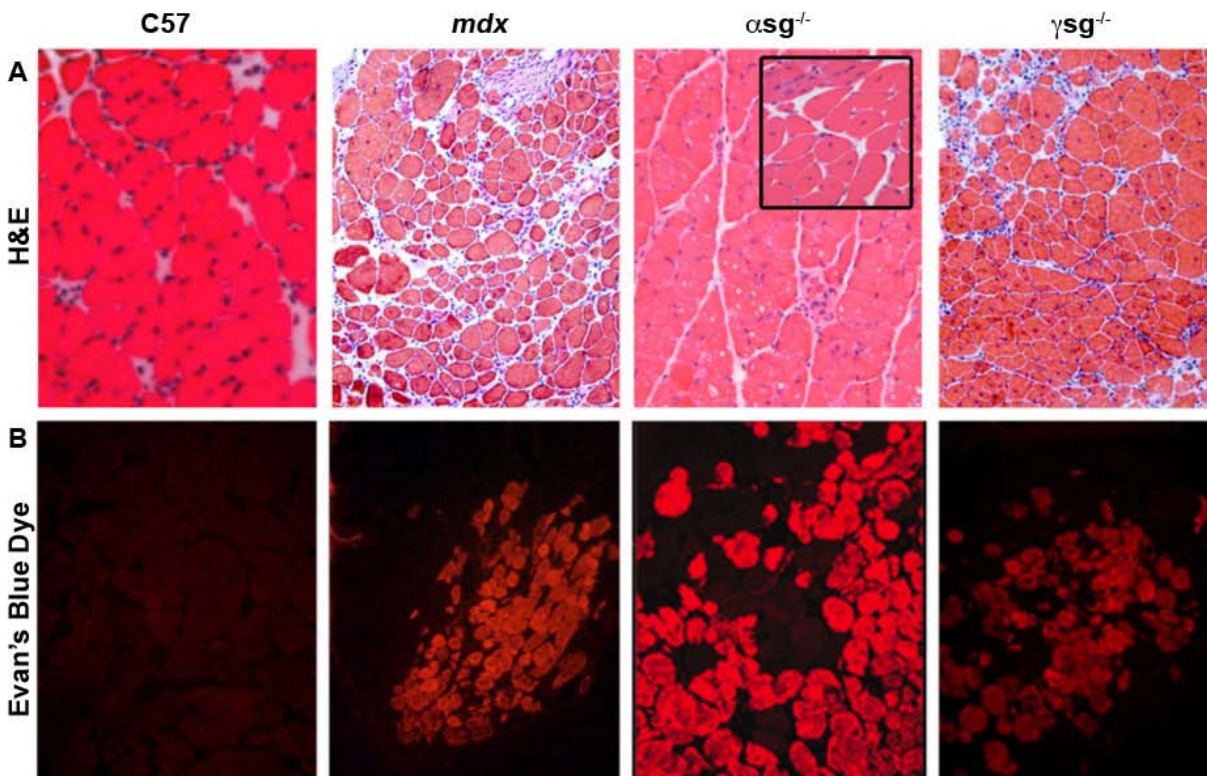


Figure 4-2. Histological verification of intensity and distribution of muscle damage in murine models of muscular dystrophy. Healthy control C57BL10 muscle is shown in the first column. (a) As seen in the hematoxylin/Eosin (H&E) stained cross sections, the control muscle has myofibers of a consistent diameter, a predominance of peripheral myonuclei, and very little space between fibers. In contrast, the dystrophic muscles show a highly heterogeneous population of fiber sizes, immune cell infiltration, an increase in extracellular matrix, and many centrally located myonuclei (inset), all of which are indicative of ongoing damage and regeneration. (b) Clusters of Evan's blue dye (EBD) positive fibers were seen in the dystrophic muscle and were not observed in controls. The spatial distribution of these EBD positive fibers was in agreement with damage observed in the T₂w MRI.

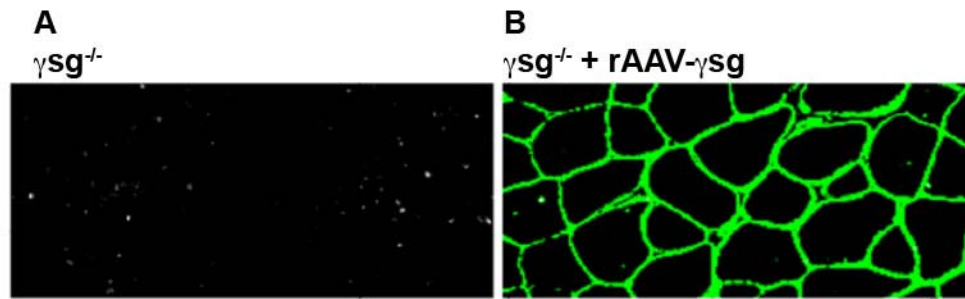


Figure 4-3. Immunohistochemical labeling of γ -sarcoglycan in muscle of the untreated (a) and treated (b) limbs of a $\text{gsg}^{-/-}$ mouse. Verification of successful gene delivery and proper spatial distribution of transgene product (γ -sarcoglycan) was observed in the treated limbs, as well as its absence was confirmed in the sham treated limbs.

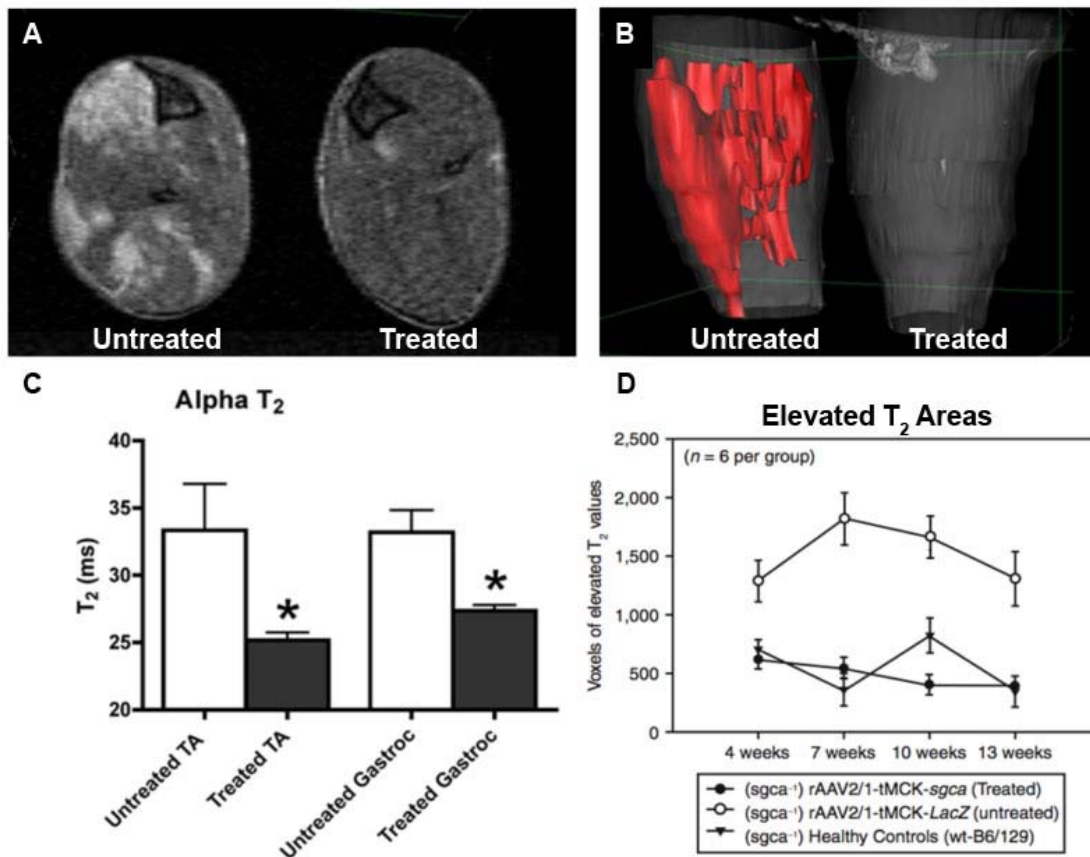


Figure 4-4. Correction of the rAAV treated limb in α -sg^{-/-} and γ -sg^{-/-} mice was easily observed in T₂ weighted MRI (a) by the absence of hyper-intense dystrophic lesions in treated tissue, while the limb that under went sham treatment displayed the pathological damage patterns similar to those seen in the young dystrophic mice in the age/strain dependant study (α -sg^{-/-} shown). (b) For illustrative purposes, lesions were segmented in multi-slice MR image sets and render in three dimensions using computer models. The red regions of damage dominate the sham treated limb, while they were completely absent in the treated limb. (c) ROI analysis of the mean T₂ of the treated and untreated TA and gastrocnemius muscles, revealed that the untreated muscles continued to have a significantly elongated T₂, while the corrected muscle's values were similar to those observed in healthy control animals. (d) The percentage of voxels with significantly elevated T₂ (>2 standard deviations above healthy control muscle) representing damaged muscle was determined (Pacak 2007). Over a course of 13 weeks the treated/sham-treated α -sg^{-/-} mice were imaged and mean muscle T₂ values were calculated. The global mean T₂ values of the sham treated muscles remained significantly elevated as compared to the treatment group and health control animals.

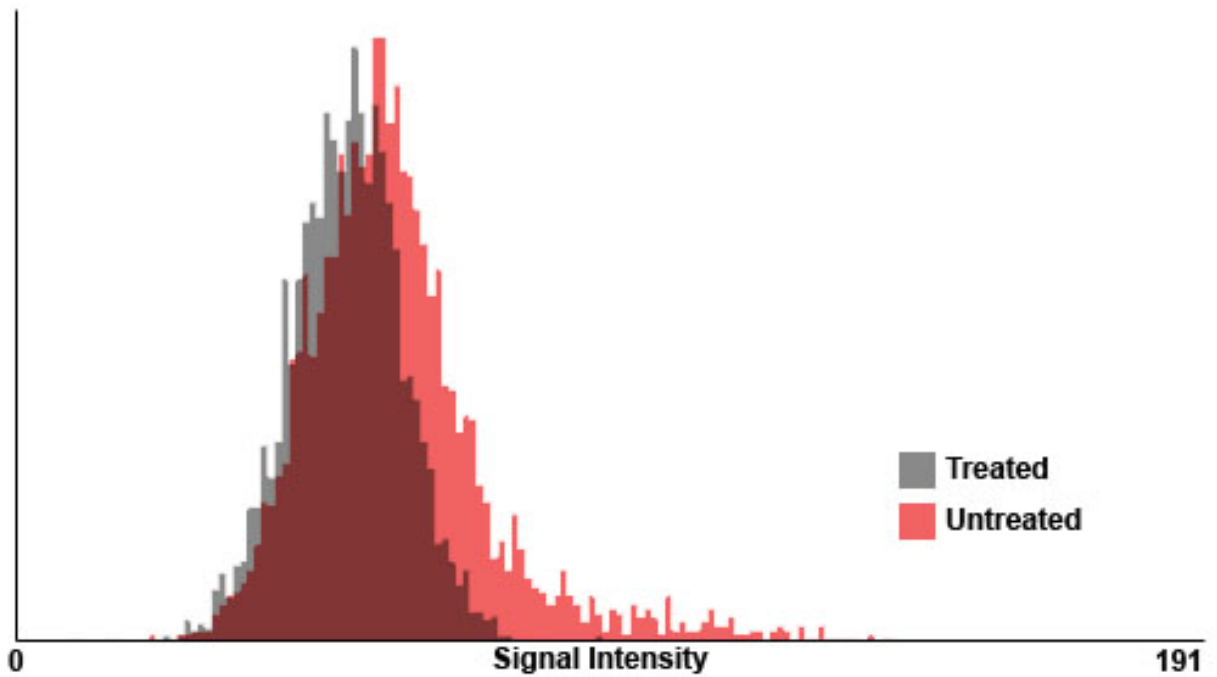


Figure 4-5. Dystrophic muscle pathology is characterized by an increased heterogeneity in T_2 . The histogram of signal intensity of voxels from regions of interest sampled from rAAV treated (grey) or untreated (red) γ sg^{-/-} muscle in heavily T_2 weighted images. The spreading of the distribution and right-ward shift are indicative of elongation of T_2 in a subpopulation muscle tissue that in this case was due to presence of dystrophic lesions.

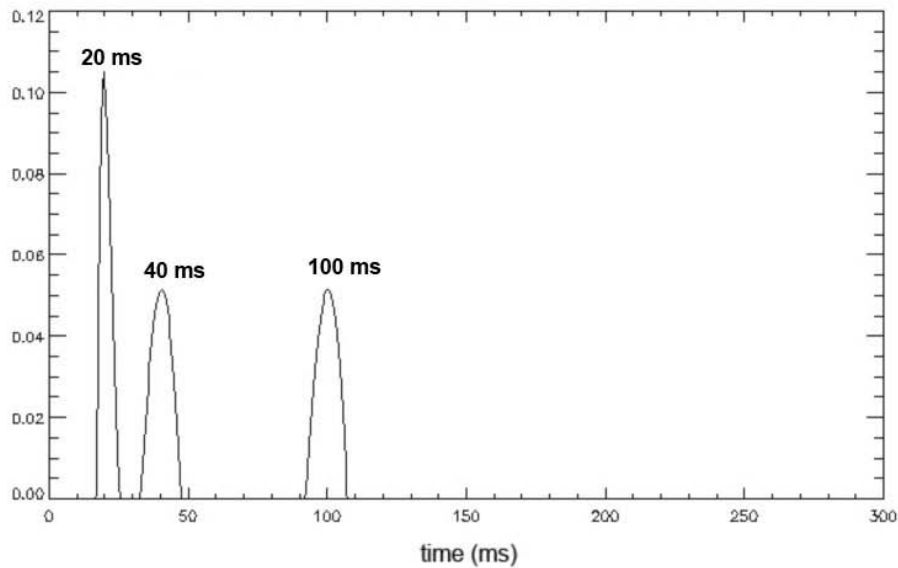
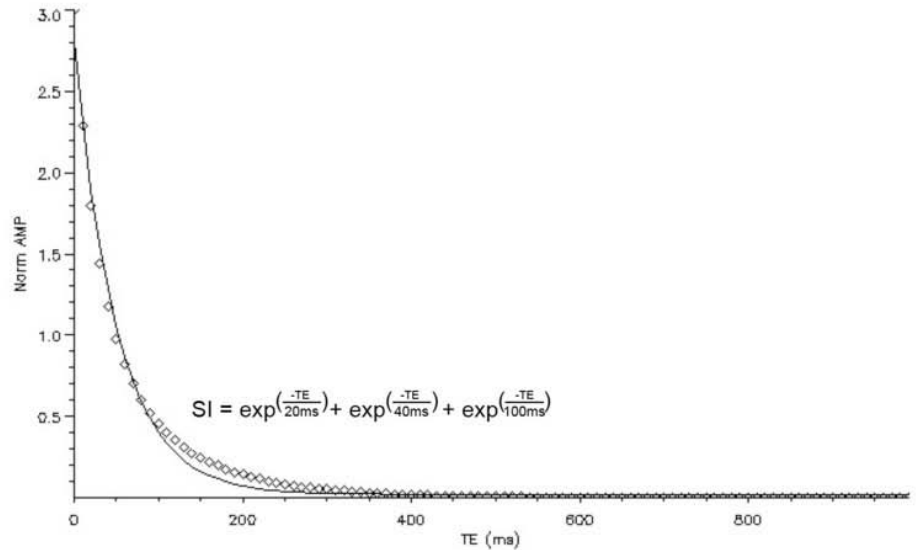


Figure 4-6. Multiple component T_2 analysis of computer simulated T_2 relaxation times. Simulations were carried out to determine the feasibility of multiple T_2 component resolution using NNLS analysis with data derived from single slice multi-echo imaging. Here a typical result is shown where three simulated T_2 components were added to the simulated signal intensity (SI) as a function of echo time (te). In this case 1,000 simulated echos were curve fit to a series of exponential decay curves and were ranked by χ^2 values. The best fits were then processed with an NNLS algorithm producing a spectra of T_2 components that had contributed to the original signal decays. The initial mono-exponential fit estimates a mean T_2 of 50.53 ms, where the NNLS analysis is able to resolve the three original components.

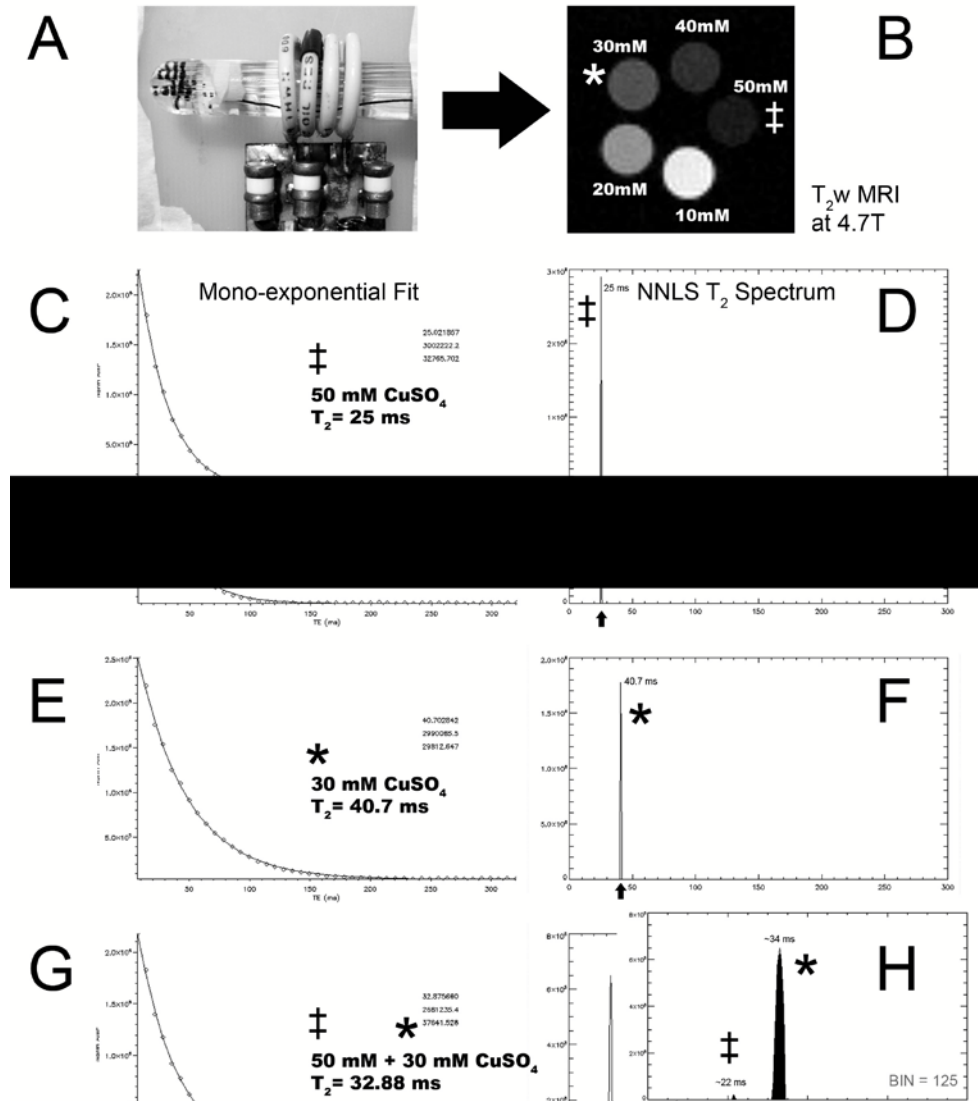


Figure 4-7. Multiple component T₂ analysis in copper sulfate (CuSO₄) phantoms (a). Studies were carried out to determine the feasibility of multiple T₂ component resolution using NNLS analysis with data derived from single slice multi-echo imaging. (b) Multi-echo T₂ weighed images were collected (60 echoes, TE/TR = 7.24ms/6s with 7.24ms increments) at 4.7 T. Multiple component analysis was carried on mean values from ROIs which were curve fit (c, e, g) to a series of exponential decay curves and were ranked by χ^2 values. The best fits were then processed with an NNLS algorithm (d, f, h), producing a spectra of T₂ components that had contributed to the original signal decays. The rate of each decay component (T₂) and its fraction of total signal contribution (integral of it histogram curve) is reflected in the resultant T₂ NNLS spectra. ROIs with only 50mM CuSO₄ (c/d) and 30mM CuSO₄ (e/f) show true mono-exponential decay, while an ROI containing both T₂ relaxations (g/h) shows resolution of both T₂ times after NNLS and a shifted mono-exponential fit (g).

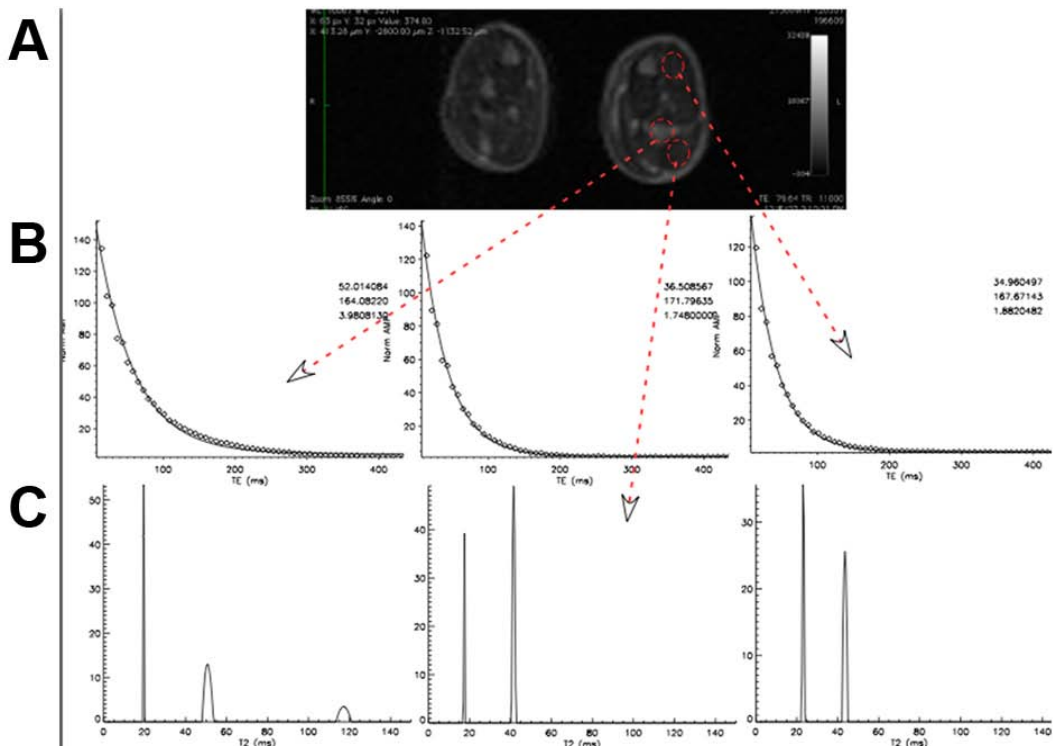


Figure 4-8. Multiple component T_2 analysis in dystrophic muscle. Studies were carried out to determine the feasibility of multiple T_2 component resolution using NNLS analysis with data derived from single slice multi-echo imaging *in vivo*. (a) Multi-echo T_2 weighed images were collected (60 echoes, TE = 7.24 ms to 434.4 ms with 7.24ms increments and a TR = 6 s) on an 11T Bruker system. Multiple component analysis was carried out using mean relative signal intensity values from selected ROIs which were curve fit (b) to a series of exponential decay curves and were ranked by χ^2 values. The best fits were then processed with an NNLS algorithm, producing a spectra of T_2 components that had contributed to the original non-mono exponential decay. The rate of each decay component (T_2) and its fraction of total signal contribution (integral of it histogram curve) is reflected in the resultant T_2 NNLS spectra. The T_2 spectra of damaged and seemingly unaffected regions were different, suggesting that further studies may reveal the underlying pathological changes that give rise to the changes observed in global T_2 measures of dystrophic muscle.

CHAPTER 5
EXPERIMENT 2: IMAGING REGENERATION IN DYSTROPHIC MUSCLE USING T_2
AND DIFFUSION MRI

Abstract

The muscular dystrophies (MD) are a group of genetic diseases, which lead to progressive weakening of skeletal muscle. Although the types of MD vary in severity, many progress due to a loss of sarcolemmal integrity due to a structural defect caused by gene mutations. This makes the dystrophic muscle susceptible to contraction-induced damage. Dystrophic muscle is especially prone to injury during eccentric, or lengthening, contractions. While the muscle repair mechanisms are intact, recently repaired dystrophic muscle fibers will still be prone to repeated damage. During these cyclic bouts of damage and recovery, the muscle tissue undergoes various stages of remodeling. In order to visualize these stages noninvasively, T_2 and diffusion weighted MRI was used to observe changes associated with damage and repair in muscle tissue. Initial observations of the process of recovery from acute injury, in healthy mice, suggested that changes in indices of diffusion were independent of changes in T_2 relaxation, and may have been more sensitive to structural changes that the remodeling tissue was going through. The directions of diffusion perpendicular to the long axis of the myofibers seem to be the most sensitive to this. While there does appear to be a consistent increase in mean diffusion in early dystrophic lesions, the random spatial and temporal appearance of the damaged areas leads to high variance and makes the measurements difficult to interpret. Experimentally synchronizing the time of incidence of the injury appears to have reduced this variation and made further analysis possible.

Specifically, I set out to image the time course of eccentric damage and recovery in dystrophic muscle caused by downhill (-14°) treadmill running for 15 - 20 minutes. The mice were pre-scanned before exercising, immediately afterwards, and imaged on days 1, 5, and 10 days post running. At each time point T_2 weighted images and diffusion tensor (DTI) data sets were collected at 11.1T. Mean T_2 in lesions rapidly increased significantly and remained elevated during most of the repair. Similar to T_2 , the mean diffusivity (ADC) also rapidly increases, but it tended to migrate towards the baseline at a faster rate during the time course of repair. The rapid decrease in FA often inversely mirrored the changes of the ADC and possibly reflected the loss of structure associated with the necrotic damage that soon follows the initial injury. Of the eigenvalues, the λ_1 and λ_2 responded with a similar trend to the ADC and were at their peak height on immediately after exercise. The third eigenvalue, λ_3 , exhibited a delay in its rise and was at its highest value at the post one-day time point. These results suggest that the observed changes in the transverse relaxation time T_2 and the indices of diffusion are governed by unique underlying mechanisms. Further, as it has been suggested in the literature, the third eigenvalue and its vector may be more sensitive to structural changes in the early stages of muscle repair that are otherwise masked by edema and inflammation.

Introduction

Histological comparisons of dystrophic and healthy muscle reveal that there is a much greater variability in fiber size (83) and the presence fiber splitting (136) found in the muscles with dystrophy. Therefore it was hypothesized that these structural

differences associated with dystrophic muscle could be detected utilizing diffusion tensor imaging (DTI).

From these experiments several indices of diffusion of water in the muscle tissue were calculated, including an apparent diffusion coefficient (ADC) and fractional anisotropy (FA), along with the eigenvectors and eigenvalues. Physical barriers to water diffusion on health muscle are drastically altered in damaged and diseased muscle. While isotropic diffusion is unrestricted in all directions (Figure 5-1A), healthy skeletal muscle is rather anisotropic (Figure 5-1B) and as such has a higher FA than damaged muscle, which may have had the normal physical barriers of diffusion breached. Studying the effects of these physical changes, resulting from pathological alteration to the muscle tissue microstructure, on the ADC and FA, as well as comparing them to measures of T_2 in prior scans of the same region, should allow the detection of unique regions of damage and regeneration in dystrophic muscle and allow us to employ a multimodal noninvasive imaging approach to the characterization of muscle tissue undergoing damage and repair.

Detecting Changes in Microstructure with Diffusion MR.

Despite the dystrophic muscle's increased susceptibility to contraction-induced damage, the muscle tissue is able to transiently repair these damaged regions, at least during the early stages of disease progression. Histological signs of muscle regeneration include high variability in the diameter of myofibers, centrally located myonuclei, expression of embryonic myosin and an activated pool of satellite cells (Fig 1b-c). Due to high frequency of damage and repair, dystrophic muscle also shows signs of remodeling of the ultra-structure, fiber splitting and changes in fiber orientation (135). Our approach for the further resolution of these structural changes due to tissue

remodeling will be the application of diffusion weighted and tensor imaging. An apparent diffusion coefficient (ADC) can be calculated for multiple planes of the muscle tissue *in vivo*. Comparison of the diffusion of water and metabolites in healthy and damaged muscle provides information on the structure and water compartmentalization of the tissue. MR measures of water diffusion in mammalian skeletal muscle were first made by Cleveland *et al.* in 1976 during NMR experiments with excised rat tibialis anterior muscles. These studies confirmed that diffusion was highly anisotropic and was less “hindered” in the direction parallel to the muscle fibers (164), i.e. along the length of the muscle fiber.

Diffusion Tensor Imaging of Skeletal Muscle.

Diffusion tensor imaging (DTI) has also proven to provide structural information about skeletal muscle through analysis of the diffusion indices it provides. It was demonstrated that DTI could distinguish differences in the water diffusion properties of muscles with different muscle functionality and revealed differences based on gender by Galbán and Ladd (165, 166). Experiments by Wedeen (2001) demonstrated the ability of DTI to examine the microstructure of skeletal muscle fiber organization by comparing the primary eigenvectors, as a measure of principal fiber direction, and angular dispersion in the bovine tongue. While it is agreed upon that the principal eigenvector relates to the direction parallel to the muscle fibers, the origin of the second and third eigenvectors is still not clear (110, 165, 167). In 2004, Galbán suggested that they likely represent diffusion in the directions perpendicular to the fiber direction (165), however histological data has yet to add evidence to support this. In addition to looking at diffusion indices from individual voxels, several studies have demonstrated the ability to apply fiber tracking algorithms to DTI data sets, allowing the reconstruction of myofiber

trajectories *in silico* based on the regional diffusion data collected in the DTI experiment (116, 168). These experiments showed the ability of measuring pennation angle, by measuring the angle of the fiber tracks from their origins at the tendon, and physiological cross sectional area (PCSA), which is directly perpendicular to the fiber tracks and directly proportional to the muscle maximum force production, suggests the possibility of predictive functional models derived from MRI data. Diffusion studies of damaged muscle have also been conducted to assess changes these DTI indices. Muscles that has been subjected to ischemia (78, 108) as well as trauma (169) often have increased T_2 and ADC, while having a decreased fractional anisotropy (FA). In models of muscle atrophy, the ADC was not affected, but the FA was increased (170). In contrast to acute injury models, Zhang *et al.* in 2008 showed that denervation-induced muscle atrophy lead to a significant increase in FA and decreases in the secondary and tertiary eigenvalues (171). The decreases in λ_2 and λ_3 were interpreted by the authors as reflecting decreases in fiber diameter during muscle atrophy. Interestingly, T_2 was increased before the observed cross-sectional area reduction in the GAS, but then remained insensitive during the remaining muscle volume loss. It was speculated that this initial elongation of T_2 may have been due to changes in perfusion or edema that where a result of the denervation (171). This uncoupling of T_2 and diffusion indices gives further argument that they are sensitive to different underlying phenomena.

The relationship between T_2 and ADC is complex and it has been shown that combined T_2 /diffusion experiments can shed additional light on the origins of these changes in diffusion indices and transverse decay with the onset of disease (36). Both

T_2 relaxation and diffusion have been demonstrated to have multiple components in healthy and damaged muscle (129). When Ababneh *et al.* investigated both multicomponent transverse relaxation and diffusion in acute edema of muscle in rats, they saw that both T_2 and ADC curves were best fit with a bi-exponential function (129). While the acute edema did alter the relative signal contribution from the slower (proposed intracellular) and faster (proposed extracellular) T_2 components in a way that supported those anatomical water compartmentalization assignments, the same did not hold true for the fast and slow diffusion components. This led the authors to suggest that an alternate form of compartmentalization was at play when it came to diffusion, such as surface associated versus free liquid pool water to give rise to the fast and slow diffusing water signals (129). In 2007, Fan and Does (130) observed a mono-exponential T_2 relaxation in healthy rat muscle tissue and a bi-exponential fit in edematous or acutely injured muscle following injection of λ -carrageenan. They further explored the relationship between T_2 and ADC by varying the echo times of their DTI sequence and found a resultant change in the calculated ADC. It was felt that the two components (short and long for T_2 and fast and slow for ADC) actually may represent the intracellular and extracellular compartments but that effects of exchange between the two pools of spins could be in flux and altered by the edema. In addition there could be possible metabolic side effects of the λ -carrageenan that was used to induce the injury or inflammation and the fact that there always is some degree of T_2 weighting, that could further cause a shift from a simple calculated expectation of what these values should be (130).

Thus, it is important to first make simple measurements of parameters of diffusion in healthy and dystrophic mouse skeletal muscle, in order establish the limits of our model and to optimize our imaging protocol. Following these pilot studies, we set out to measure T_2 relaxation, along side diffusion parameters such as ADC and FA, in various mouse models of muscular dystrophy and compare them to healthy controls. Further we evaluated the ability of these diffusion parameters to detect and monitor therapeutic correction in mouse models of limb girdle muscular dystrophy. Ultimately, we explore a synchronized damage model in *mdx* mice, via treadmill running, that allows us to determine changes in the eigenvalues and eigenvectors, of the calculated diffusion tensor, during recovery from muscle injury and compare them to the trends of T_2 , ADC and FA. With this model, we hope to better understand the process of lesion repair in dystrophic muscle and to provide researchers with a tool that provides insight into structural remodeling.

Experimental Design

Specific protocols are described in Chapter 3, the following describes the overall design of the experiments relevant to the results presented in this chapter. The initial results presented in this chapter, related to myotoxin injected control mice, are from the work of Åkerstedt and Yap (Masters Thesis, 2004) from our laboratory and are presented here for the sake of discussion and their underlying importance to the development of the rationale behind my current work. These data consist of two experiments, first measuring T_2 and diffusion after notexin, a myotoxin derived from the venom of the Austrian Tiger Snake, *Notechis scutatus scutatus* (172), injection into the TA muscle in (n=13) healthy C57BL mice, and a second set of measures in *mdx* mice, comparing damaged and unaffected muscle.

The same protocols were then used to obtain T_2 and diffusion weighted images to evaluate the sensitivity of these contrast methods to detect structural changes and prevention of disease in viral gene therapy treated LGMD IIe (*sgca*^{-/-}) mice. In these studies, diffusion was measured along 3 orthogonal laboratory frame axis's (X, Y and Z), with the mean fiber orientation of the majority of lower limb muscle being parallel to the Z axis (Figure 5-2).

Following those studies, muscle water diffusion was further explored by implementing diffusion tensor imaging (DTI) in healthy and dystrophic mice. A total of six young (age: 2-5months) and six old (age: 18-24 months) control C57BL/10SnJ, *mdx*, and LGMD IIc (*sgcg*^{-/-}) mice were imaged using directional diffusion weighted imaging (DWI) at 4.7T and DTI at 11.1T to investigate differences in the indices of diffusion in lower hind limb muscles of dystrophic mice throughout disease progression.

In a parallel experiment an additional six 4-6 week old LGMD IIc mice underwent muscle specific delivery of human γ sg into the lower right leg. High resolution, short TE, and high *b* value diffusion tensor imaging DTI data was collected at 11.1T (Figure 5-1). A fiber orientation independent ADC and fractional anisotropy (FA) was calculated using Paravision JIVE (PV4; Bruker Avance) software. Analysis of the DTI data provided additional parameters that gave information about the direction and magnitude of apparent water diffusion in each voxel represented by a set of eigenvectors and eigenvalues. Close inspection of the corresponding eigenvectors and eigenvalues, along with FA, has aided us in our interpretation of the ADC results and helped to refine a working model of muscle damage and water diffusion. T_2 weight images were also

acquired at 11.1T and provided the opportunity to directly compare changes in global T_2 and changes in mean ADC between healthy and damaged muscle tissue.

Treadmill model of eccentric damage. Mice were allowed to run on a downhill treadmill at an angle of -14° (-24.9% grade) for 15 to 30 min at a speed of 8 to 10 m/min (Figure 5-2). Exercise was terminated when they could no longer run. This protocol was developed based on reporting the literature and our own experience. This work was approved by the IACUC at the University of Florida. The mice were first imaged before running and at 0, 1, 2, 5, and 10 days post exercise.

Results

The goal of this study was to determine the sensitivity of diffusion and T_2 weighted MRI to study structural changes during pathogenesis and repair following acute damage in dystrophic skeletal muscle.

Diffusion weighted imaging of recovery from acute damage in healthy control C57BL/10 mice.

In order to determine the sensitivity of diffusion weighted imaging (DWI) to track the structural changes in murine skeletal muscle following acute injury, Åkerstedt and Yap (Masters Thesis, 2004) investigated the TA muscles from a set of healthy C57 control mice ($n=13$) that were injected with notexin, a myotoxin derived from snake venom, or saline solution (serving as a negative control) by collecting diffusion and T_2 weighted MRI. To evaluate these changes over the time during the healing process, the MRI data was collected at 48 hours and 96 hours post injury and at 48 hours alone for mock injury (Figure 5-3). Both limbs were imaged simultaneously and diffusion weighted images were collected with the diffusion sensitive pulsed field gradients along

the three base axis's of the magnet (the slice selective direction, Z; the phase encoded direction, Y; and the frequency encoded direction, X).

The fibers of the TA muscle were nearly parallel to the Z axis, while the X and Y axis's were approximately perpendicular to the long axis of the myofibers. At both post injection time points (48 hr and 96 hr) the T_2 relaxation times of the notexin injected muscles was significantly lengthened, while it was unchanged in the saline injected muscles (as compared to mean T_2 of healthy unjected data). While T_2 was significantly increased at both 48 and 96 hours, there was no difference between these two post injected time points. The diffusion in all three directions (D_x , D_y , D_z) was also significantly increased at 48 hours post injection, while diffusion the saline control injected mice remained normal. The diffusion in the slice direction that is parallel to the fiber length increased during the first two day but failed to be significantly different by day four. In contrast, the diffusion in the perpendicular directions (x and Y) to the myofibers had significantly decreased by 96 hours, as compared to the same measurements in the saline injected control muscles. So while T_2 was sensitive to detecting damage and inflammation, it was not sensitive to structural or environmental changes taking place in the recovering tissue. The observations made in notexin injured muscle led to the hypothesis that bulk water diffusion could provide additional information not available with T_2 measures. The dynamic elevation followed by a significant depression of the diffusion in directions perpendicular the fiber length suggests that they are the most sensitive to the structural changes during muscle repair.

Diffusion weighting imaging of damaged and unaffected muscle in *mdx* mice.

To investigate the ability of diffusion weighted imaging to detect pathological changes in dystrophic skeletal muscle (Figure 5-3), again Åkerstedt and and Yap

(Masters Thesis, 2004) investigated young *mdx* mice (n=7) by MR imaging them at an age known to display an abundance of dystrophic lesions (3 – 6 months old). Regions of interest were manually determined using manual tracing in custom software; dystrophic lesions (designated *mdx-d* for “damage”) and unaffected regions (*mdx-u*) of muscle tissue were outlined for measurements. The T_2 relaxation in the unaffected regions was not different from that of control muscle at this age, while the dystrophic lesions consistently had a significantly lengthened T_2 . Like the control C57 limbs 48 hours post injected with notexin, the dystrophic lesions were determined to have increased diffusion in the axial directions, perpendicular to the muscle fibers, as compared to the unaffected tissue. Interestingly, there was no significant change in the diffusion along the long axis of the myofibers between unaffected and lesions. This again suggests that the long axis is less sensitive to alterations the tissue is going through during repair and damage.

Diffusion weighted imaging of rAAV correct *sgca*^{-/-} mice.

Using the same protocol established in our laboratory (described above), I set out to evaluate the sensitivity of T_2 and diffusion weighted MRI to detect the prevention of pathogenic structural changes in α -sarcoglycan null mice which were treated with a recombinant adeno-associated virus (rAAV) bearing the gene for human α -sarcglycan, or a mock treatment in the contra lateral limb. At 4 weeks of age the mice were MR imaged with diffusion weighting in the directions parallel and perpendicular to the muscle fiber orientation. While there was a significant increase in the T_2 relaxation in the muscles of the mock treated limbs, the rAAV treated muscles were restored to normal levels of the T_2 time constant for healthy muscle; thus successfully detecting correction of the pathological phenotype (56). Yet, the diffusion in the axial direction (perpendicular

to fiber length) was not found significantly different from the untreated limb. (Figure 5-4) Nor was the diffusion along the length of the fiber. This seems to be due to several sources of variance in either the animal model itself or the imaging procedure.

Diffusion tensor imaging (DTI) in rAAV corrected *sgcg*^{-/-} mice.

To determine if the previously observed variation arose from subtle inconsistencies in the limb orientation in reference X, Y and Z axes of the laboratory frame, a rotationally invariant method of diffusion tensor imaging was utilized to evaluate a similar group of treated animals (Figure 5-5). In this study, *sgcg*^{-/-} mice were treated with a rAAV virus carrying the gene for human γ -sarcoglycan. DTI studies of gene corrected of the *sgcg*^{-/-} mice again showed trends that would be expected with successful treatment, but the measurements had a high degree of variation and the groups were not significantly different. Since limb orientation could then be ruled out as the source of variance, we hypothesized that the random distribution of temporal stages and severity of lesions were likely contributing a large amount of variation into our statistical analysis (Figure 5-6)

Recovery from eccentric damage.

To overcome possible variations in the indices of diffusion, due to the random distribution of occurrence of injury and severity, an attempt to synchronize the damage in a physiologically relevant manner was made. Skeletal muscle in various types of muscular dystrophy has been demonstrated to be susceptible to eccentric contraction induced damage. As such, a model of mild damage induced from a single bout of treadmill running, angled at a downhill angle of $\sim 14^\circ$ (Figure 5-7), proved to be a physiologically relevant model for synchronized tissue repair in the *mdx* mouse than the use of a general agent like a myotoxin. Using this model, the *mdx* mice showed

consistent damage in all muscle groups (predictable regions were in the medial compartment), while healthy C57 control mice did not show any damage at day 2 post exercise (Figure 5-8). While the mean T_2 in a lesion rapidly increases and remains lengthened during most of the repair process (T_2 : 18.9 ± 0.5 ms, 30.7 ± 1.3 ms^{**}, 27.7 ± 1.7 ms^{**}, 19.9 ± 0.3 ms, 17.64 ± 0.2 ms; for Days Pre, 0, 1, 5, and 10. ^{**} $P < 0.001$ vs Pre, ANOVA) there are many subtle but significant changes that can be seen in the different parameters of diffusion (Figure 5-9). Like the T_2 , the mean diffusivity (ADC) also rapidly increases, but returns to the baseline at a faster rate during the time course of repair. The rapid decrease in FA inversely mirrors the changes of the ADC and reflects the loss of structure associated with the necrotic damage that soon follows the initial injury. Of the eigenvalues, the λ_1 and λ_2 responded with a similar trend to the ADC and were at their peak height immediately after exercise. The third eigenvalue, λ_3 exhibited a sustained significant increase for 24 hours, while λ_1 and λ_2 had become indistinguishable from unaffected muscle after the first day. The highest value for λ_3 was observed one day post running.

Discussion

These experiments were designed to establish a better understanding of the dynamic changes in T_2 and the indices of diffusion following acute and chronic damage in dystrophic skeletal muscle, so that they may be monitored noninvasively using MRI. Similar histological studies rely on sacrificing representative groups of animals at various time points after the incidence of injury. While these data have high resolution and allow a vast array of biological staining and labeling procedures to report the state of the tissue, it does not give us a continuous picture of the dynamic repair process of a

single specific lesion. Early work presented here from Åkerstedt and Yap (Masters Thesis, 2004) demonstrated that while T_2 is a reliable marker for acute muscle damage, it is not very sensitive to massive structural changes going on in regions of repair. And of the directions of diffusion (relative to the laboratory frame's primary axis's X, Y, and Z) the directions that were perpendicular to the long axis of the myofibers were the most sensitive to structural and environmental changes occurring at 2 and 4 days after myotoxin injection into the TA muscle of healthy C57 mice. This is in agreement with other studies of diffusion in damaged skeletal muscle (108). Similar trends were observed in dystrophic lesions as compared to seemingly unaffected regions of *mdx* mice. When simple diffusion weighted imaging was applied to LGMD mice treated with a recombinant adeno-associated virus in the left hind limb and a mock treatment in the other, high levels in variation made it difficult to consistently distinguish between the treated and non-treated limb.

In order to reduce variation brought on by measuring dystrophic lesions of unknown temporal existence, in various stages of repair, we utilized a downhill treadmill running protocol to synchronize the incidence of injury. By imaging the mice before and after running and specifically following lesions that had all occurred during the same, single bout of exercise, we then had a method to follow subtle changes in the indices of diffusion MRI and compare these observations to values of T_2 as a reference of acute damage. The data acquisition was just over one hour long and great care was taken to maintain the mouse's body temperature so that it would not confound our measures of diffusion or physiologically alter perfusion. As expected, a significant rise in T_2 following exercise, which persisted for approximately one week after running, was observed in

the *mdx* mice and was back to normal resting values in a matter of hours in the control animals. Thus the bout of exercise was just at the threshold of damage for the dystrophic model and it was well within the range of limits for normal use and performance of healthy muscle tissue (Figure 5-8). As was observed in the notexin experiments in the healthy C57 mice, immediately after injury an increase in ADC and a concomitant reduction in FA was seen in the exercised *mdx* muscle. This was consistent with an increase in tissue swelling and loss of restriction of water, presumably mostly in the axial directions since water is already not as restricted in the direct parallel to fiber orientation. To look at these changes in diffusion closer, the eigenvalues were measured (along with noting the eigenvector orientations). The primary and secondary eigenvalues largely followed trends similar to the T_2 and the ADC, i.e. they immediately increased and slowly returned to normal values over the next week. Interestingly, fluctuations were also seen in seemingly unaffected muscles as well, but they were not as pronounced as the changes in the lesions themselves (Figure 5-9). The greatest difference between unaffected and affected (lesion) muscle was seen in λ_3 and FA. While an anatomical assignment for the 3rd eigenvector is difficult to make, it has been suggested to be sensitive to changes such as swelling (78) and so perhaps changes in fiber diameter as well.

These results suggest that the observed changes in the transverse relaxation time T_2 and the indices of diffusion are governed by unique underlying mechanisms. Further, the third eigenvalue (λ_3) and its vector may be sensitive to structural changes in the early stages of muscle repair that are otherwise masked in T_2 weighted imaging by edema and inflammation. The addition of the down hill running protocol to this

experiment offered a physiologically relevant method to study damage and recovery in a dystrophic animal that also reduced the variation of our measures and highlight the importance of synchronized damage in models like these. A combined analysis of T_2 and diffusion parameters appears to be a promising approach for monitoring recovery from damage in longitudinal studies of dystrophic skeletal muscle. Such advances in the non-invasive characterization of repair events and markers of damage will advance preclinical development of viable treatments for muscular dystrophy. In addition recent reports of DTI and fiber tracking in human skeletal muscle (118) suggest that it may have applications in human MD research as well.

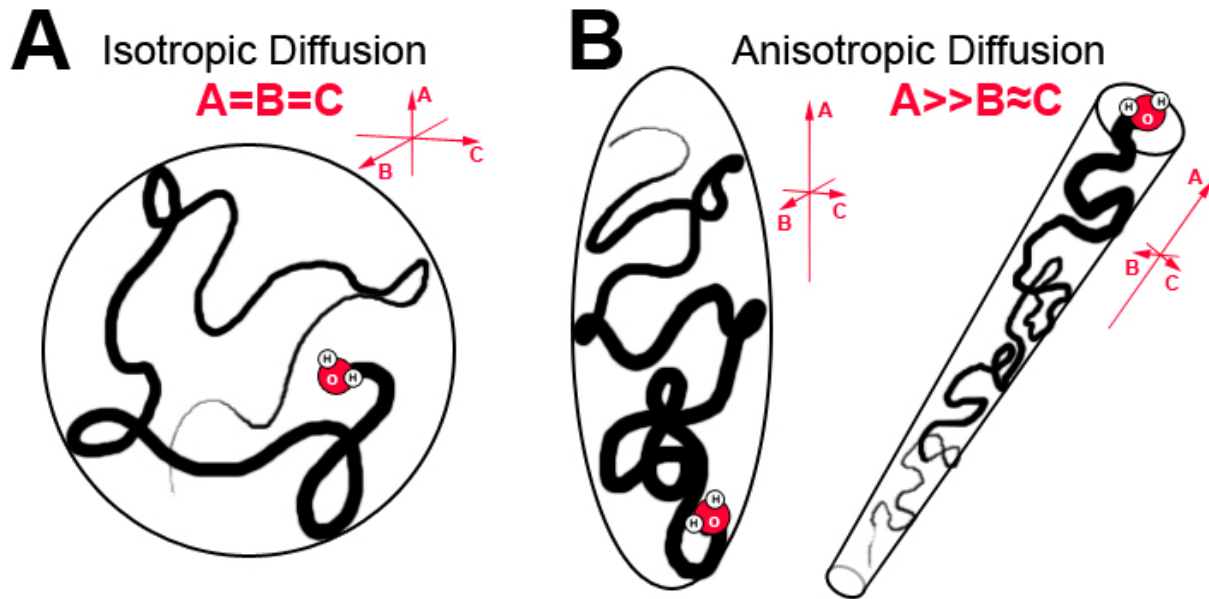


Figure 5-1. The diffusion of water molecules can be restricted by physical barriers in biological tissues. If the diffusion is completely unhindered A) it is isotropic and all the probability is equal for movement of molecules traveling in all directions ($A=B=C$). The greater the mean diffusion in all directions is, the greater the apparent diffusion coefficient (ADC) will be. If, on the other hand, the diffusion is limited in one or two directions B) it is anisotropic. If diffusion in one direction greatly out ways the other two, than the tissue is said to have a high fractional anisotropy (for example if $A \gg B \approx C$). Note that healthy muscle fibers will tend to be rather anisotropic, due to their tube-like structure similar to cylinder depicted on the far ride side of the figure.

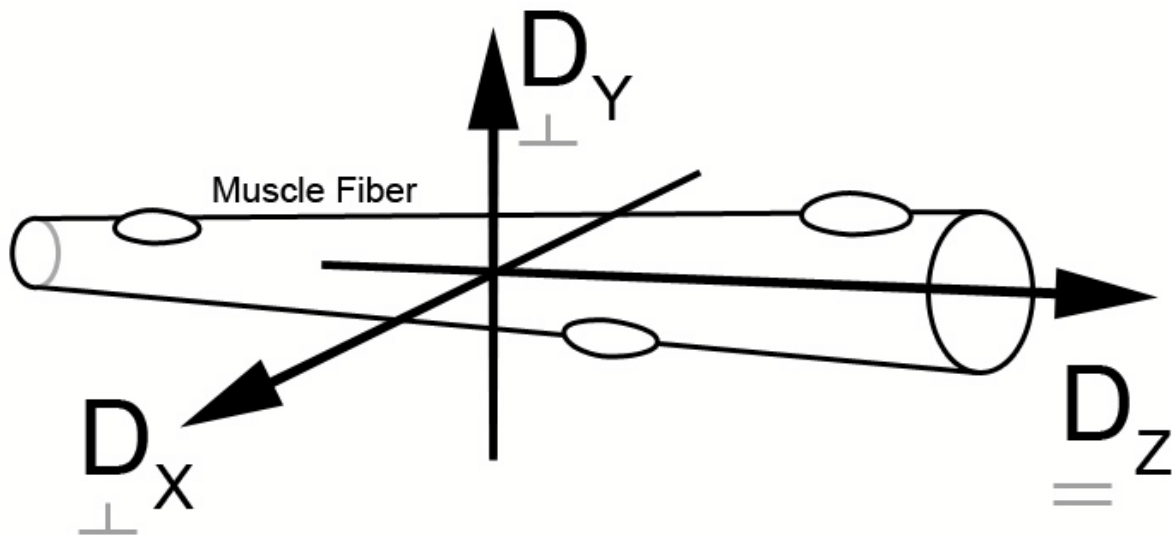


Figure 5-2. Muscle fibers are normally rather anisotropic and in our experiments the length of the muscle fibers run approximately parallel to the Z-axis, while the X axis and Y axis are perpendicular to the fiber. In this cartoon of a healthy muscle fiber the multiple myonuclei are peripheral.

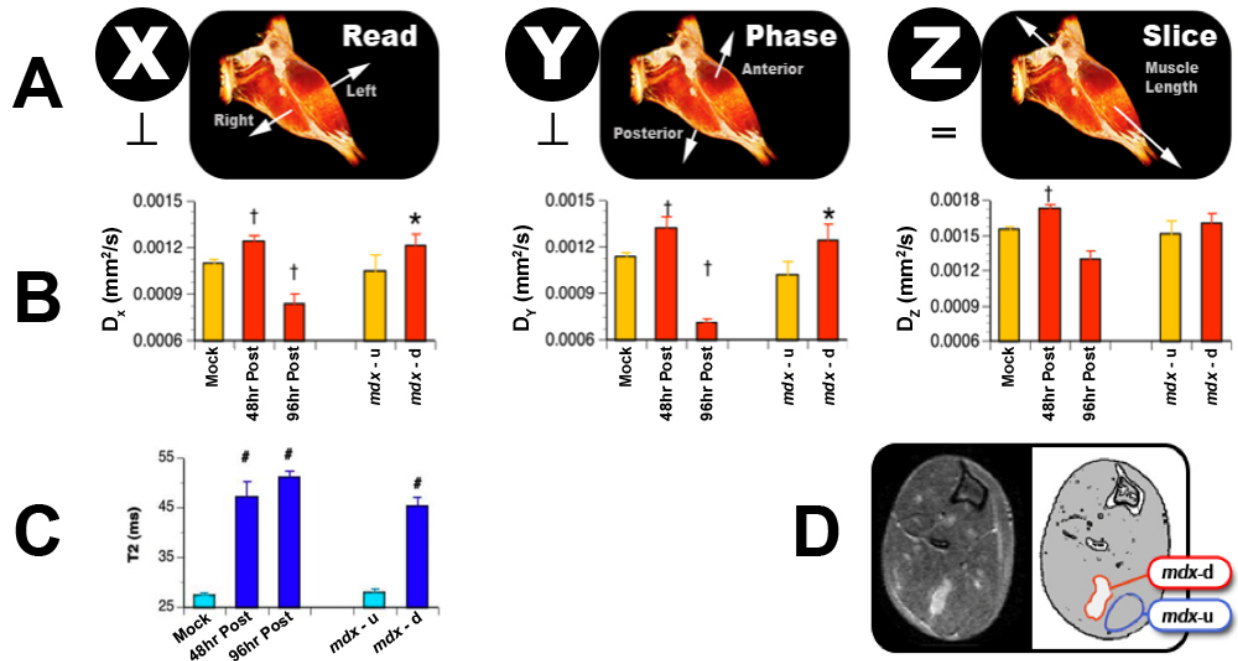


Figure 5-3. Muscle fibers of the TA muscle relative to the diffusion sensitive pulsed field gradients used in the DWI sequences at 4.7T. The X direction (frequency encoded) and Y direction (phase encoded) of the laboratory frame were perpendicular to mean myofiber orientation in the TA, while the Z direction (slice selection) was approximately parallel.

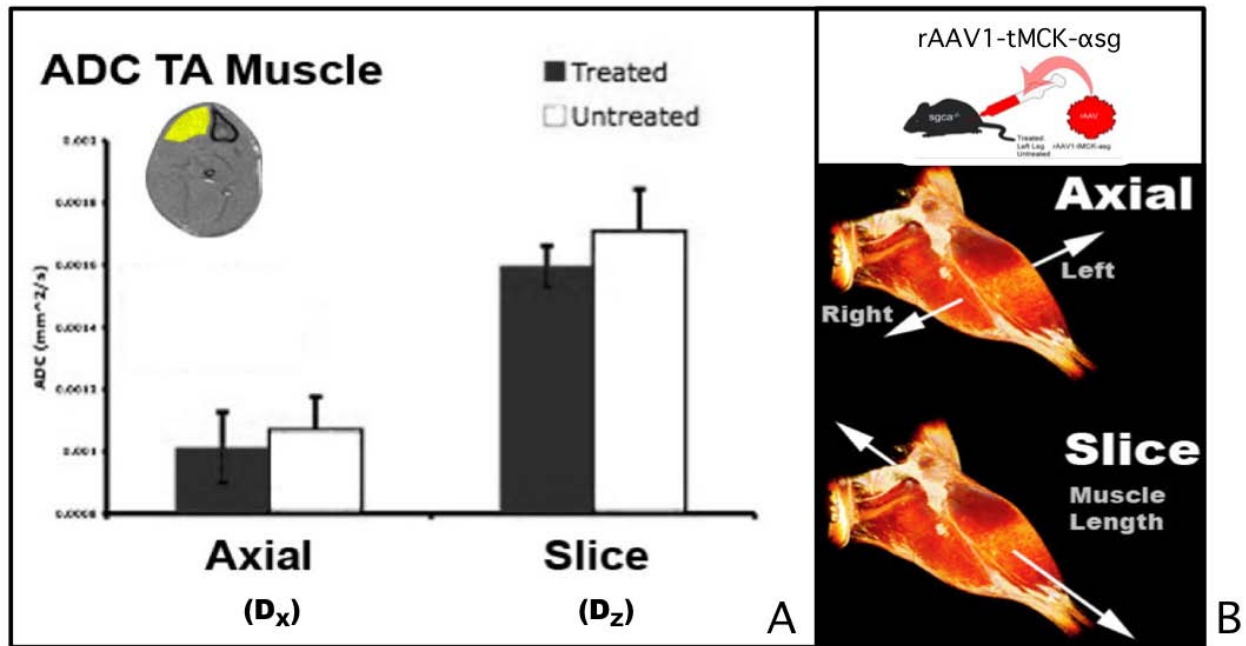


Figure 5-4. Diffusion weighted imaging of gene corrected LGMD mice. An AAV viral vector was used to deliver human α -sarcoglycan to group of $sgca^{-/-}$ LGMD mice. Images were collected with the diffusion gradient applied either longitudinally (parallel) or axially (perpendicular) to the mean direction of muscle fibers in the limb.

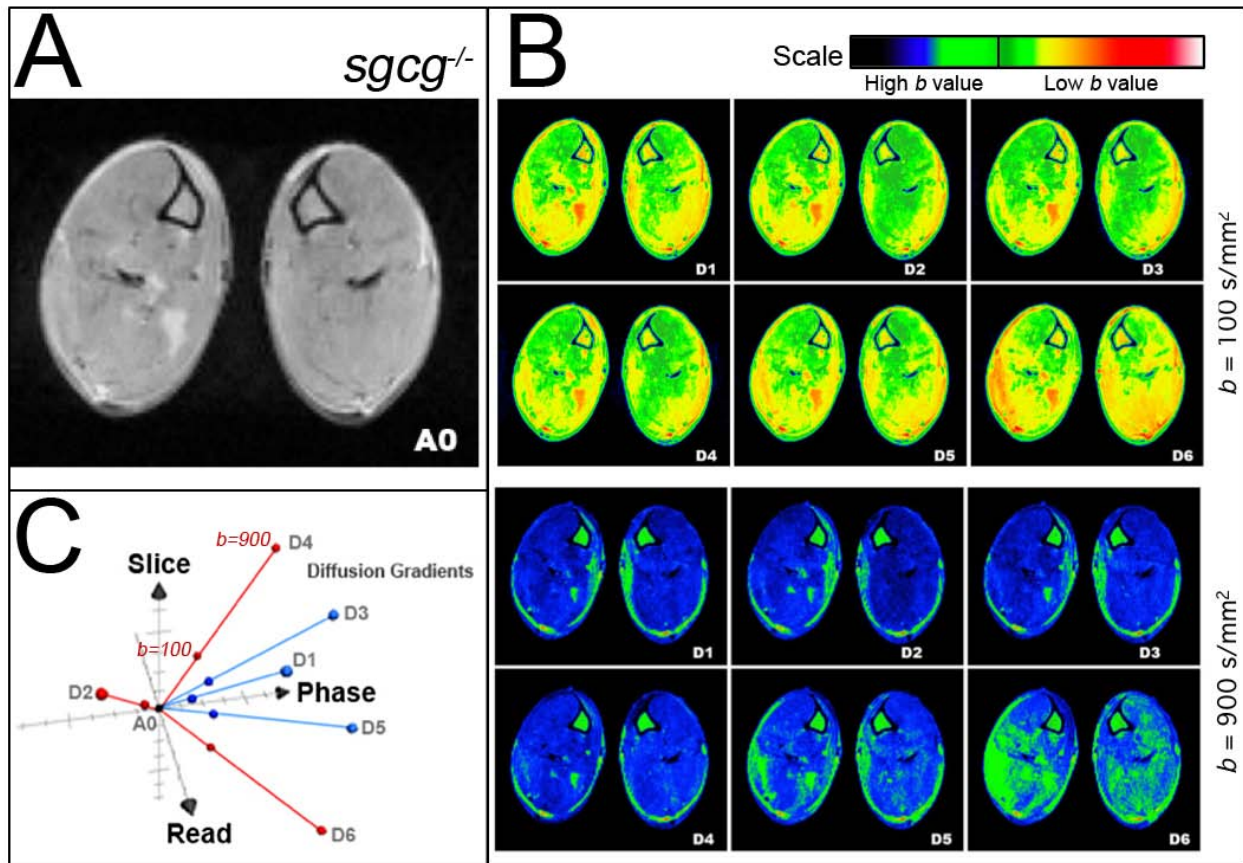


Figure 5-5. Directions and diffusion weighting in diffusion tensor imaging. This series shows a typical DTI data set for a young (2-6 month old) *sgcg*^{-/-} mouse. A) The A₀ image has no diffusion weighting. A dystrophic lesion can be seen on the head of the medial GAS muscle on the right limb (left side of the image). Both hind limbs were imaged simultaneously. Images with low and high ($b = 100$ and 900 s/mm^2) were collected in 6 different directions. The set of images were then used to calculate the mean apparent diffusion coefficient (ADC), fractional anisotropy (FA) along with the eigenvectors and eigenvalues of the tensor. These indices of diffusion were then monitored in control and dystrophic muscle at baseline and following acute injury.

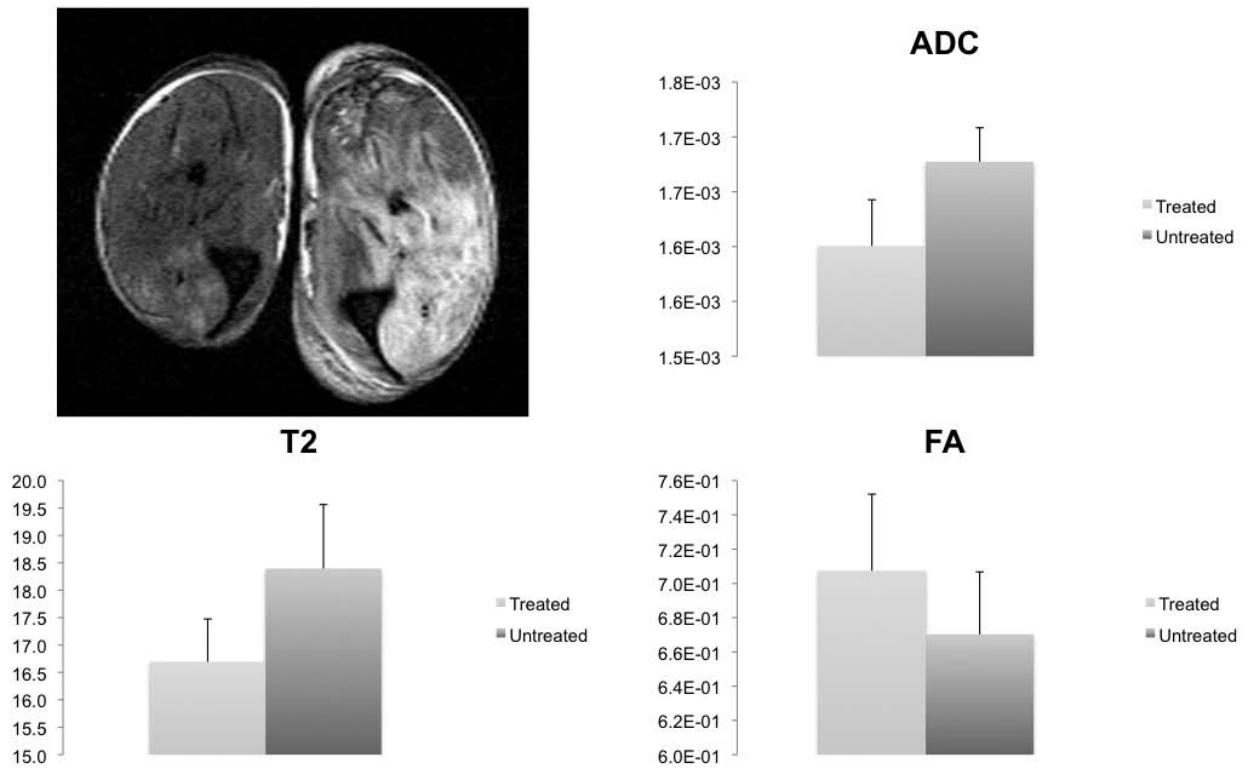


Figure 5-6. Diffusion tensor imaging of viral vector treated γ -sg^{-/-} mice. The inset image shows that the untreated left limb was continued to exhibit a dystrophic phenotype of dystrophic lesions while the right limb looks like healthy control muscle. The untreated limb had an increase in T₂ and ADC and a drop in FA.

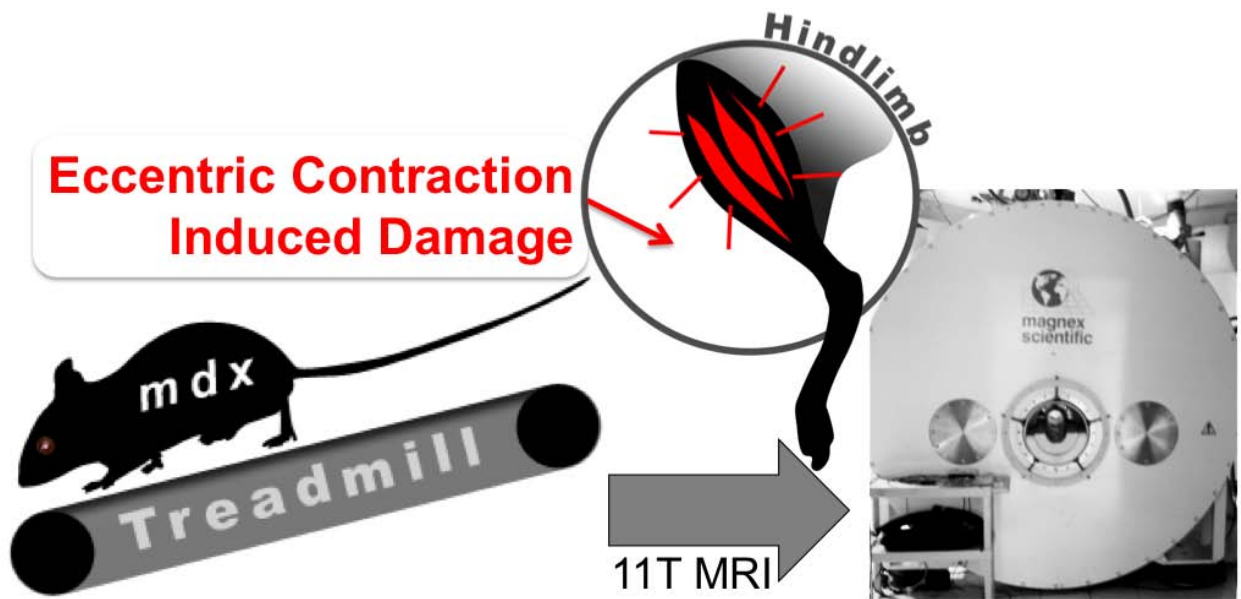


Figure 5-7. Schematic diagram illustrating the downhill running protocol. The mice ran on a treadmill with a $\sim 14^\circ$ angle for 20 – 30 min at a speed of 8-10m/minute.

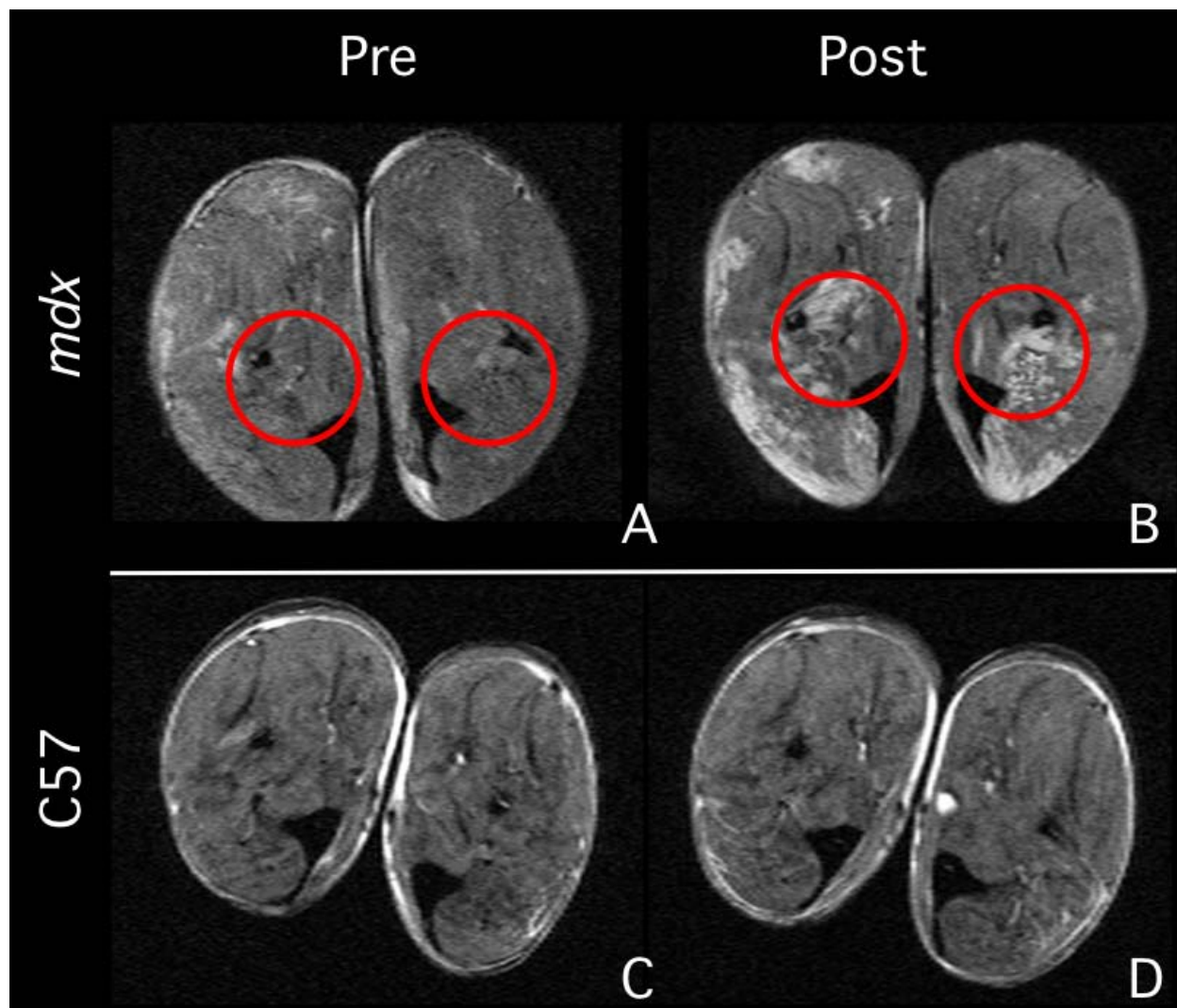


Figure 5-8. Control C57 and *mdx* hindlimb muscle post downhill treadmill running. A) Shows the pre-exercise condition and B) show 24hrs post running. Panels C and D suggest that the control C57 mice are not injured by the duration or intensity of the running protocol.

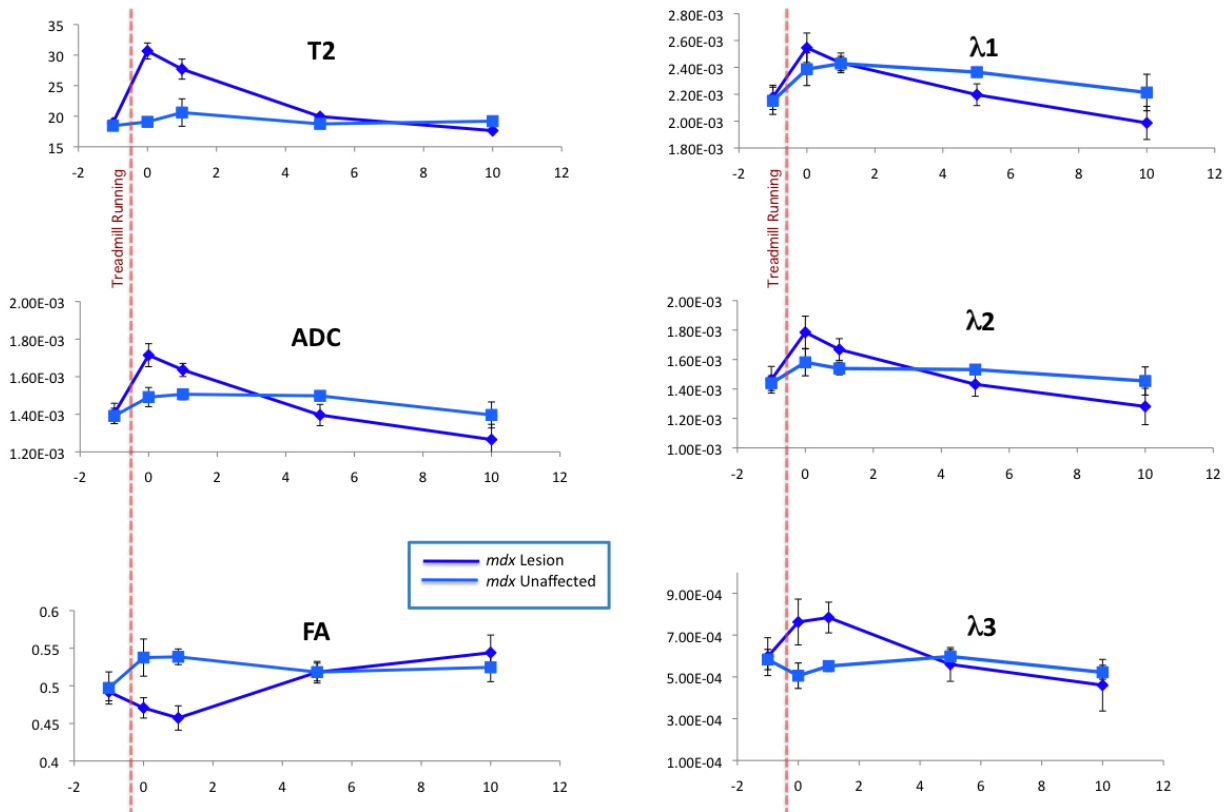


Figure 5-9. T₂ and diffusion indices during recovery from eccentric contraction induced muscle damage. The dark blue plot show the characteristics of a dystrophy lesion, while the light blue line follows a muscle that was not directly damaged by the exercise protocol. Both FA and the third eigenvalue, λ_3 , were interesting over the course of recovery from damage.

CHAPTER 6
EXPERIMENT 3: ASSESSMENT OF DAMAGE AND FIBROSIS IN DYSTROPHIC
MUSCLE USING MAGNETIZATION TRANSFER MRI

Abstract

Experiments were performed to assess the ability of magnetization transfer (MT) to detect tissue damage in dystrophic muscle. Areas of muscle edema and acute damage were determined based on areas of elevated T_2 . The relationship between MT, age and areas of tissue damage was determined in control and *mdx*, and LGMD mice. In addition changes in MT were visualized following an acute bout of muscle damage in *mdx* mice. The ability of MT to detect tissue damage and fibrosis in muscular dystrophy was determined based on comparison with histology. Fibrosis was measured by staining muscle collagen, the major protein of fibrotic tissue, with Masson's trichrome dye. Studies were performed on the hindlimb muscles of murine models of Duchenne (*mdx* mice) and Limb-Girdle (γ sg^{-/-} mice) muscular dystrophies. The following results were obtained: 1) MTR is decreased in young dystrophic muscle, 2) Changes in MT contrast correspond to areas of T_2 elevation in young dystrophic muscle and following acute muscle damage; 3) MT is decreased in the presence of extensive fibrosis and decreased muscle T_2 in old dystrophic mice and 4) MT was significantly increased following gene correction in LGMD. All of these data taken together suggest that the changes in MT reflect tissue damage in dystrophic muscle. The underlying mechanism resulting in MT contrast is multifactorial and results from a combination of changes in water compartmentation, fibrosis, and possibly protein structure.

Introduction

The major defect in DMD is the absence of dystrophin and the primary role of dystrophin is to maintain the integrity of the muscle plasma membrane during muscle

contraction (173). Therefore, the skeletal muscle cell membranes of affected individuals are susceptible to damage during contraction (174). This leads to a loss in the integrity of muscle cells, a loss of skeletal muscle function, and eventually fibrosis (175). The mechanism involved in the muscle damage which occurs in other forms of MD, such as limb girdle MD, is similar. In these cases, there is a loss of dystrophin-associated proteins which leads to the same type of muscle damage and fibrosis (141).

Throughout the progression of the dystrophic myopathies, the affected muscles undergo numerous cycles of damage and repair. When the regenerative capacity of these muscles has been exhausted, the fibers are progressively replaced by the fat and connective tissue which is the hallmark of fibrosis (176). Fibrosis has particularly negative effects because it greatly reduces muscle function, discourages endogenous repair mechanisms (177), and interferes with many therapeutic interventions. The current clinical methods for determining fibrotic changes in muscle rely heavily on histological evaluations of muscle biopsies. In addition to being invasive, this method suffers from the disadvantage of the inability to easily examine the entire muscle region over time. A valuable asset to the study of muscular dystrophy would be the development of a non-invasive technique to assess skeletal muscle fibrosis.

Detection of Fibrosis with Magnetization Transfer Imaging.

The repeated bouts of damage and repair that are associated with muscular dystrophy results in either an exhaustion of support cell regenerative capacity and/or a remodeling of the tissue environment that results in an ever increasing replacement of functional muscle fibers with scar tissue and fat. This build up of lipid and fibrosis both decreases the muscle's elasticity and reduces the volume of tissue that will be receptive to treatment. Extensive fibrosis has been observed in animal models of muscular

dystrophy and progressively increases as the animal ages (67). MRI has been shown to be a valuable tool in the study of these neuromuscular diseases, yet current methodology falls short of directly measuring tissue fibrosis. This difficulty arises from the extremely short T_2 and short diffusion times (88-91) associated with collagen. To overcome this investigators have utilized a technique which images the magnetization transfer of signal from a "bound" pool of water to the highly mobile bulk pool of water (72). Tissues containing high concentrations of hydrated macromolecules with short T_2 s, such as muscle and cartilage, experience the largest magnetization transfer effect, resulting in larger decreases in signal intensity compared to other tissues (i.e. fat, blood, water). Guo *et al.* (2003) suggested that magnetization transfer contrast MRI was sensitive to an increase in tissue fibrosis in a murine model of liver disease (73). They showed that the amount of magnetization transfer (at 4.7T) was related to the degree of liver fibrosis and the hydroxyproline content. Hydroxyproline is a modified amino acid that is almost exclusively found in collagen, making it a quantitative biochemical measure of tissue collagen content (74, 75). Magnetization transfer (MT) was first measured in skeletal muscle tissue by Wolff and Balaban in 1989 and they estimated it to be three times more efficient than MT in the kidney (72). Based on these previous MRI studies, the initial hypothesis of this study was that the increased tissue fibrosis associated with aging dystrophic muscle will result in an age dependent increase in muscle MT from a "bound" pool of water, associated with collagen and proteoglycans, to "bulk" water.

MT Imaging of Dystrophic Muscle.

Fatty tissue deposition has complicated the interpretation of MT results in human subjects with muscular dystrophy. For instance, Schick *et al.* found that when using a

water selective imaging sequence that that there was no difference in MT between affected and unaffected muscles in three patients with Erb muscular dystrophy (76). In contrast, McDaniel *et al.* not only found that in subjects with LGMD that MT was dramatically reduced in muscles with gross fatty infiltration but MT also was reduced in muscle tissues without visual evidence of fatty infiltration (77). Overall fatty tissue infiltration is anticipated to be lesser a problem in murine models of dystrophy. Mouse models of muscular dystrophy reflect many of the hallmarks of human dystrophies with muscle fiber damage and regeneration, yet the amount of fatty tissue infiltration is not as severe (78).

MT Imaging of Damaged and Fibrotic Muscle.

Decreased muscle MT has also previously been shown to occur under conditions of large fluid shifts. Yoshioka *et al.* showed an inverse correlation of MT in muscle with free water content in exercised muscle (79). Also Mattila *et al.* found that following muscle damage in a rodent model that there are large acute changes in MT that could not be associated with fatty tissue infiltration over the time scale studied (80). Acute muscle damage is associated with muscle fiber swelling, edema, cell necrosis and regeneration. It has also been suggested that other factors such as destruction of the large protein complexes, damaged cell membranes, and infiltration of inflammatory cells could also reduce MT (81). Vahlensieck *et al.* used MT imaging to look at intramuscular tumors and observed that muscular scar tissue had a lower MTR than healthy muscle, while both had MTR values that were significantly higher than that of the tumors (82). This supports the possibility that despite collagen having a high MTR relative to most body tissues and a increase in it's concentration with progressive fibrosis, that due to the higher MTR of healthy muscle, an increase in fibrosis in muscular dystrophy could

result in a decrease in the MTR that is independent of an increase in water content (edema) or lipid deposition. Thus it was intended in this study to use MT imaging as a method of detecting progressive fibrosis in mouse models of muscular dystrophy.

Therefore, the objective of this study was to investigate the ability of MT to detect fibrosis and damage in animal models of muscular dystrophy, which undergo extensive fibrosis with age. In addition, MT contrast was compared with T₂-weighted MRI, a measurement which has been used extensively to assess muscle damage in dystrophic and injured muscle. T₂ mapping was also used as guidance in determining the muscle regions of interest for the MT contrast experiments and in the interpretation of the results. Experiments were performed by using animal models of Duchenne and Limb-Girdle muscular dystrophies.

Methods

Animals

This study was conducted with approval from the University of Florida Institutional Animal Care and Use Committee (IACUC). A total of twelve C57BL/10SnJ, twelve *mdx* (C57BL/10ScSn-Dmd^{mdx}/J), and twelve LGMD IId (γ sg^{-/-}) mice were studied. The twelve mice of each strain were further stratified into two age groups being young and old, resulting in six mice in each unique age/strain group. The animals were housed in an AAALAC accredited animal facility in a temperature (22±1°C), humidity (50±10%), and light (12 hr light/dark cycle) controlled room.

MR Imaging Data Acquisition

MRI was performed in the lower hindlimb muscles of control and dystrophic mice at different ages. Specifically, quantitative T₂ imaging was implemented to monitor muscle injury/regeneration and MT to assess muscle fibrosis. During all *in vivo* MR

experiments animals were anesthetized using gaseous isoflurane (3% induction, 0.5-2.5% maintenance). Both hindlimbs were imaged simultaneously using a custom built four-turn, 1.5 cm single tuned ^1H solenoid coil (200MHz) and a 4.7T Bruker Advance (Rheinstetten, Germany) horizontal bore spectrometer (Paravision V3/DMR). To determine transverse relaxation rates (T_2), multiple slice, single spin-echo, diffusion-controlled images were acquired with the following parameters: FOV=1cm, matrix=256x128, slices=12, slice thickness=1mm, slice gap 1 mm, diffusion weighting $b=5 \text{ mm}^2/\text{s}$, NEX=2 and TR=2s. To avoid the contribution of stimulated echoes to the T_2 measurement, I implemented a Hahn spin-echo MR image sequence in which two separate acquisitions were acquired at echo times of 14 and 40 ms (15).

Magnetization transfer was measured using a same spin-echo sequence, except that a single transaxial image was acquired using a MT preparation pulse consisting of a total of 40, 25 msec square pulses (93). First, in a subset of dystrophic and control animals Z-spectra were acquired with frequency offsets of ± 20 , ± 15 , ± 10 , ± 5 KHz using a 1s pre-saturation pulse. The pre-saturation power level was empirically derived based on in vivo optimal MT contrast ($n=6$). However, measurements were only performed within SAR power levels (see methods chapter). The absence of tissue heating was determined using an agar phantom with a fiber optic thermocouple. Based on the Z-spectra, consistent discrimination between control and dystrophic animals was observed at a frequency offset of -10KHz. Therefore all subsequent MT data were collected with a pre-saturation pulse at this frequency offset.

Finally, longitudinal relaxation rates (T_1) of dystrophic and control muscles were determined by progressive saturation. Single slice, transaxial images were acquired

with a variable TR sequence with TE=7ms, FOV=2.4x 1.8cm, matrix=128x64, slice thickness=3mm, NEX=1 and TRs=6, 3, 1.5, 0.75, 0.325, and 0.2s.

MR Image Analysis

All T_2 and MTR images were analyzed using in-house software running in the Interactive Data Language programming environment (IDL version 6.2, ITT Corp.). T_2 was calculated assuming a single exponential decay with respect to TE as previously described (15). A T_2 threshold map was created based on individual T_2 values. Pixels with T_2 values 2 standard deviations above the average T_2 value of control (C57BL/10) muscles were considered to be affected (15). Subsequently the mean T_2 value of the muscles of interest (TA and GAS) was determined, as well as the mean T_2 of affected versus unaffected regions. Muscle groups and affected /unaffected muscle regions were outlined in five image slices and the mean T_2 recorded. For the magnetization transfer experiments, the MTR ratio was calculated using the following equation:

$$MTR = 1 - \frac{M_{Sat}}{M_0} \quad [\text{Equation 6-1}]$$

with M_0 representing the scan with no MT pulse and M_{Sat} representing the image with the MT pulse on. First, a MTC map was created based (56) on individual pixel M_{Sat} / M_0 values. Subsequently, the mean MTR value was determined from the same ROI as in the T_2 maps.

T_1 images were analyzed using Paravision 3.0.2 (Xtip; PV3) and T_1 was calculated assuming a single exponential function.

$$M_z(t) = M_0 \left(1 - e^{-t/T_1} \right) \quad [\text{Equation 6-2}]$$

Specifically, the mean T_1 of the TA and GAS was calculated by fitting the exponential increase in ROI signal intensity of each muscle as a function of TR.

Histological Measurements.

Following completion of the MR experiments, all animals were euthanized. The tibialis anterior and gastrocnemius muscles were dissected from both hindlimbs. The muscles were fixed at resting length, coated in O.C.T. gel (Tissue-Tech) and rapidly frozen in melting isopentane and stored at -80°C . Frozen muscles were subsequently cut in half and sectioned at the belly of the muscle (the region of muscle with the maximum cross sectional area). Frozen sections ($10\ \mu\text{m}$) were either stained using Masson's Trichrome Stain Kit (Richard-Allan Scientific) or Hematoxylin and Eosin. Sections were visualized and digitized under brightfield at 5x and 20x magnification on a DM LB microscope (Leica Microsystems, Solms, Germany).

Digital micrograph images of the trichrome stained tissue were analyzed using ImageJ (<http://rsbweb.nih.gov/ij/>). ROIs, containing the entire muscle cross section, were manually selected and the percentage of positive collagen staining tissue (based on area) was calculated using a Hue-Saturation-Intensity color model for pre- and post-thresholding measures (H:146-206, S:0-255, I:0-255; Pass Filter).

Postnatal Gene Delivery

Gene delivery to the left leg of $\text{sgcg}^{-/-}$ mice was achieved by IM injection of 3 week old mice with a muscle specific recombinant adeno-associated virus which expresses the human form of the missing γ -sarcoglycan (sgcg). The contralateral limb received mock treatment. Briefly, 3 week old $\text{sgcg}^{-/-}$ mice were anesthetized by induced hypothermia. Vector diluted in phosphate-buffered saline (total volume of $35\ \mu\text{l}$ per injection) was directly injected into the lower hindlimb using a 29 $\frac{1}{2}$ gauge tuberculin

syringe. The needle was inserted near the distal tibialis anterior tendon and pointed upwards along the tibia. Virus solution was injected while withdrawing the needle to maximize volume distribution across the lower limb (56). MR imaging of both *sgcg*^{-/-} hindlimbs was performed at 8 weeks and 1 year of age.

Statistical Analysis

All data are expressed as mean±standard errors. T-tests were performed to compare mean T₂ values of the TA and GAS muscles in experiment 1. For experiment 2, one-way ANOVA was used to analyze the dependence of T₂ and MTR on age and mouse strain. Paired t-tests were used to evaluate differences between mean T₂ and MTR values of the treated and untreated legs of the *sgca*^{-/-} mice in experiment 3. Statistical significance was set at P <0.05.

Results

Optimization of Magnetization Transfer Contrast.

In order to optimize the scan protocol for detection of damage and fibrosis in murine models of muscular dystrophy, magnetization transfer ratios (MTR) were compared over a range of presaturation offset frequencies in aged (>72 wks) healthy C57BL10 and dystrophic *mdx* mice. Aged mice were chosen for optimization due to the advanced pathology and fibrosis found in the older dystrophic animals. The objective was to determine the presaturation offset frequencies which optimize the differences between control and dystrophic muscle. The relative loss in signal intensity was plotted for each corresponding presaturation offset frequency and this Z-spectra was used to compare MT in control and *mdx* gastrocnemius muscles are shown in Figure 6-1. At all offset frequencies tested (-20KHz to +20KHz; 5KHz increments) the MT ratios were lower in dystrophic than in control muscles (Figure 6-2), as seen by magnetization

transfer causing a less severe drop in signal intensity (i.e. the signal intensity in a dystrophic muscle remains higher following an MT pulse than it would in health control muscle). The Z-spectrum in $\gamma\text{sg}^{-/-}$ animals was similar to that in *mdx* mice. Because the largest differences in magnetization transfer contrast were observed between -10 and -15KHz, all subsequent data were acquired at -10KHz. A comparison of MT contrast in the hindlimb muscles of healthy control, *mdx*, and $\gamma\text{sg}^{-/-}$ mice is shown in Figure 6-3A. These results were obtained using the optimal conditions described above. The data demonstrate differences in MT contrast between control and the two dystrophic samples. Dystrophic muscles have less MT overall than control muscles, and the lesions ($T_2 > 2\text{SD}$) within dystrophic muscle display minimal MT.

T_2 and MTR in Gastrocnemius Muscles From Young and Old Control and Dystrophic Mice.

Magnetization transfer ratios (MTR) and transverse relaxation rate constants (T_2) were measured in the GAS muscles from young and old control C57 and dystrophic *mdx* and $\gamma\text{sg}^{-/-}$ mice. The rationale for this approach is that younger dystrophic animals display more acute muscle damage while older dystrophic mice display more fibrosis (177). Our hypothesis is that T_2 is the better technique to assess acute muscle damage while MTR is a technique that may be useful to assess fibrosis. T_2 and MTR in GAS muscles from young control and dystrophic mice are shown in Figure 4-1B (T_2) and Figure 6-3B (MTR). These measures were made including the anatomical cross-section of the muscle and included regions that had dystrophic lesions. A complete listing of these findings is presented in Table 6-1 for the TA and GAS muscle of young and old mice from healthy and dystrophic mice. While these data made it clear that MT was able to distinguish healthy from dystrophic muscle, areas of acute damage always had the

opposite trend as compared to T_2 . This was likely due to dominating effects of bulk water influx associated with inflammation in the early months of murine models of dystrophy.

Because our primary aim was to assess the ability of MTR to detect fibrosis, areas of acute muscle damage with dystrophic lesions were excluded from the MTR measurements. In order to exclude these areas, T_2 maps were calculated and areas that had a T_2 value of greater than 29 ms (two times the standard error over the mean of healthy muscle) were avoided when ROIs were defined. This adjustment allowed us to evaluate changes in MTR based on changes in the muscles while avoiding areas dominated by pooling of fluid, i.e. areas of edema or inflammation.

Even after avoiding lesions (Figure 6-4), the muscles from dystrophic *mdx* mice displayed significantly longer T_2 values (*mdx*-GAS 28 ± 0.7 ms) than those from the γ sg^{-/-} and the control animals (γ sg^{-/-}-GAS 26.47 ± 0.85 ms, C57-GAS 27.38 ± 1.44 ms), and the T_2 values were longer in the muscles from *mdx* than in those from γ sg^{-/-} animals (Table 6-2). On the other hand, there was no significant difference in the MTR values of muscles from control and either dystrophic animal (*mdx*-GAS 0.81 ± 0.02 , γ sg^{-/-}-GAS 0.81 ± 0.01 , C57-GAS $0.81 \pm < 0.001$). The control muscle had considerably less variation. The increase in T_2 values suggest that young dystrophic muscle is in a state of acute damage and that the damage is greater in *mdx* than in γ sg^{-/-} animals. The lack of a significant difference in MTR measurements between young control and young dystrophic muscle may mean that the young dystrophic mice have not yet developed significant levels of fibrosis.

The results of the T_2 and MTR measurements in GAS muscles from old control and dystrophic mice are shown in Figure 6-4. There is no difference in T_2 between control and dystrophic animals (*mdx*-GAS 26.64 ± 1.34 ms, γ sg^{-/-}-GAS 26.94 ± 1.21 ms, C57-GAS 26.48 ± 0.29 ms). However, there is a significant decrease in MTR in dystrophic mice relative to control (*mdx*-GAS 0.76 ± 0.03 , γ sg^{-/-}-GAS 0.78 ± 0.03 , C57-GAS 0.80 ± 0.01). The decrease in MT is greater in *mdx* than in γ sg^{-/-} animals. These results suggest that bouts of acute damage in aged dystrophic muscle have largely subsided at this point in disease progression and are reflected by the relatively normal T_2 values. Of great interest is the significant decrease (6%) in MTR in older dystrophic muscle as compared to healthy age matched controls. This result indicates that changes in MTR are associated with the fibrosis that comes with advanced disease progression.

Histological Assessment of Fibrosis in Dystrophic Muscle.

In order to verify the development of fibrosis in dystrophic muscles, experiments were performed with GAS muscles from young and old control, *mdx* and γ sg^{-/-} mice. The appearance of collagen, the major protein of fibrotic tissue, was assessed by staining the muscles with Masson's Trichrome. There was no apparent fibrosis in muscles from younger dystrophic animals. The results obtained from muscles of older animals are shown in Figure 6-5 and is quantified in Figure 6-6 using a color-threshold image processing method to measure the percentage of tissue staining positive for collagen (blue in color). There is no visible fibrosis in control animals. On the other hand, there is collagen present in the muscles from both dystrophic samples. There is more apparent fibrosis in muscles from *mdx* than in those from γ sg^{-/-} animals. These results are similar

to those obtained with MTR; i.e. there is a larger decrease in MT signal in *mdx* than in *sgcg*^{-/-} muscles with age. Furthermore, histological analysis of the TA muscles in all groups of animals showed few signs of the development of fibrosis. This was also in agreement with MTR measures of the TA, which appears to be somewhat protected in aged dystrophic mice.

These histological data, in combination with our previous MR imaging results, indicate a relationship between an increase in tissue fibrosis and a decrease in MTR of skeletal muscle in the hindlimb of murine models of muscular dystrophy.

Use of T₂ and MTR in Monitoring Therapeutic Intervention.

T₂ and MT contrast images of hindlimb muscles were compared from untreated *γsg*^{-/-} mice and from mice which received intramuscular injections of a recombinant virus that expresses human alpha or gamma sarcoglycan. This type of therapeutic intervention leads to reversal of the dystrophic effects. Images were made in younger animals (3 months of age). The results are shown in Figure 6-7. In younger animals, there were significantly more pixels with elevated T₂ in untreated than in treated mice and a significant increase in MTR between the two groups in both the TA and GAS muscles (~ 5%). This is an indication that viral gene delivery was effective in reducing the acute muscle damage which occurs in younger animals and that there was no development of fibrosis at this time.

Discussion

Older dystrophic muscle was expected to be significantly more fibrotic than healthy control tissue, especially as age and pathology progressed. Young dystrophic muscle showed evidence of damage and repair, but did not show extensive overproduction of collagen in the extracellular matrix so early in the course of the disease. The trichrome

stained tissue sections were useful in assessing the spatial distribution of fibrosis in the muscle cross sections, but *ex vivo* histology can be difficult to register with MR data acquired *in vivo*.

The results of these experiments suggest that a decrease in muscle magnetization transfer (MT) is an indicator of muscle damage in dystrophic muscle. The evidence for this includes the following: 1) histological data show no significant fibrosis in GAS muscles from young dystrophic mice, and there is no significant difference in MT between GAS muscles from young dystrophic animals and controls; 2) histological data show significant fibrosis in GAS muscles from older dystrophic mice, and there is a significant decrease in MT in GAS muscles from older dystrophic animals relative to control; 3) histological data show more fibrosis in GAS muscles from *mdx* (Duchenne model of MD) than from *sgcg*^{-/-} (limb girdle model of MD) dystrophic animals, and there is a greater decrease from control in GAS muscle MT from *mdx* than from *sgcg*^{-/-} mice; and 4) Histological data show little signs of fibrosis in TA muscles from dystrophic mice, and there was no decrease in MT. 4) *sgcg*^{-/-} mice which were treated with a gene transfer technique have no histological signs of hind limb muscle fibrosis, and there is no decrease in hind limb muscle MT relative to controls following the gene transfer treatment. All of these data taken together suggest that the decrease in muscle MT in dystrophic mice is related to tissue damage and fibrosis.

The rationale for doing this study was that most MRI techniques to image the replacement of muscle with connective tissue have not been proven to be successful. For example, measurements of diffusion imaging and T₂ were not useful in detecting fibrosis. This was due to the fact that T₂ is extremely short and diffusion times are very

fast when imaging collagen, the major protein of fibrotic tissue. Some investigators have attempted to use magnetization transfer in order to overcome these previous difficulties (88). With this technique, the magnetization transfer of signal from a “bound” pool of water to a highly mobile bulk pool of water is imaged. In fact, tissues containing high concentrations of hydrated macromolecules, such as muscle, exhibit the greatest MT effect. Therefore it was hypothesized that an increase in muscle tissue fibrosis would result in an increase in muscle MT from a “bound” pool of water associated with collagen to “bulk” water (92). In this regard, Guo *et al.* demonstrated previously that the amount of MT is related to the degree of liver fibrosis in the Niemann Pick Type C mouse (93). Thus, in the current study, it was expected that an increase, not a decrease, in muscle MT with fibrosis would be observed.

There are at least three possible scenarios to explain the decrease, rather than an increase in MT in fibrotic muscles. First, it is possible that fatty tissue infiltration may account for some decrease in magnetization transfer in these muscles. It has been known for some time that fat tissue has an extremely low MT (178). For example, McDaniel *et al.* showed that MT was dramatically reduced in muscles with gross fatty infiltration in subjects with limb girdle muscular dystrophy. In addition, Shick *et al.* reported that using a water selective imaging sequence would minimize the signal from fat in patients with Erb muscular dystrophy. Although fat infiltration can be a source of decreased MT, it is probably not the case in our experiments for the following reasons: 1) I determined MT in areas in which muscle T2 was not elevated; 2) when compared to canine or human dystrophies, murine muscular dystrophy is characterized by an extremely low degree of fatty tissue replacement (41).

The second possible reason for a decrease in MT involves tissue water. Studies have shown that there is a decrease in magnetization transfer under conditions of an increase in tissue water content. These conditions may be associated with tissue damage as in muscle fiber swelling, edema, cell necrosis and regeneration, inflammation, and damage associated with exercise (120, 121, 179). For example, Yoshioka *et al.* showed a correlation between a decrease in MT and the free water content in exercised muscle. However, it is unlikely that these areas of damage were involved in the decrease in MT in our current studies. Measurements of T_2 were used to identify areas of damage (15) so that they were excluded from measurements of MT.

The third possible explanation for a decrease in MT in fibrotic muscles involves the MTR of collagen and is probably the most likely explanation. Healthy muscle tissue has a relatively high magnetization transfer ratio; i.e., muscle is very efficient at MT (176, 180). Collagen, in the form of cartilage, also has a relatively high MTR, but it is slightly lower than healthy muscle tissue (181). Therefore, when healthy muscle tissue is replaced by collagen in fibrosis, one may expect a decrease in MT. A similar explanation may account for the increase in MT which occurs with liver fibrosis (93). In this case, liver tissue has a relatively low magnetization transfer ratio while the MTR of collagen is greater. In liver fibrosis, healthy liver tissue with a lower MT is replaced by collagen with a greater MT which leads to an overall increase in signal. For example an increase collagen content in muscle would results in a slight decrease in MTR whereas an equal change liver would increase MTR tremendously. Therefore, all of this information taken together suggests that the most likely reason for a decrease in MT

with muscle fibrosis is the replacement of healthy muscle tissue with collagen which has a lower MT than muscle tissue.

Finally, the results of all these experiments suggest that the use of T_2 and magnetization transfer together can be a valuable tool in MRI studies of murine models of muscular dystrophy. T_2 -weighted MRI can be used to identify areas of edema and acute muscle damage. Therefore, these areas of damage can be identified and filtered out, or not used, for measurements of magnetization transfer. Thus, the decreases in MT in regions of muscle free from edema suggest the development of fibrosis.

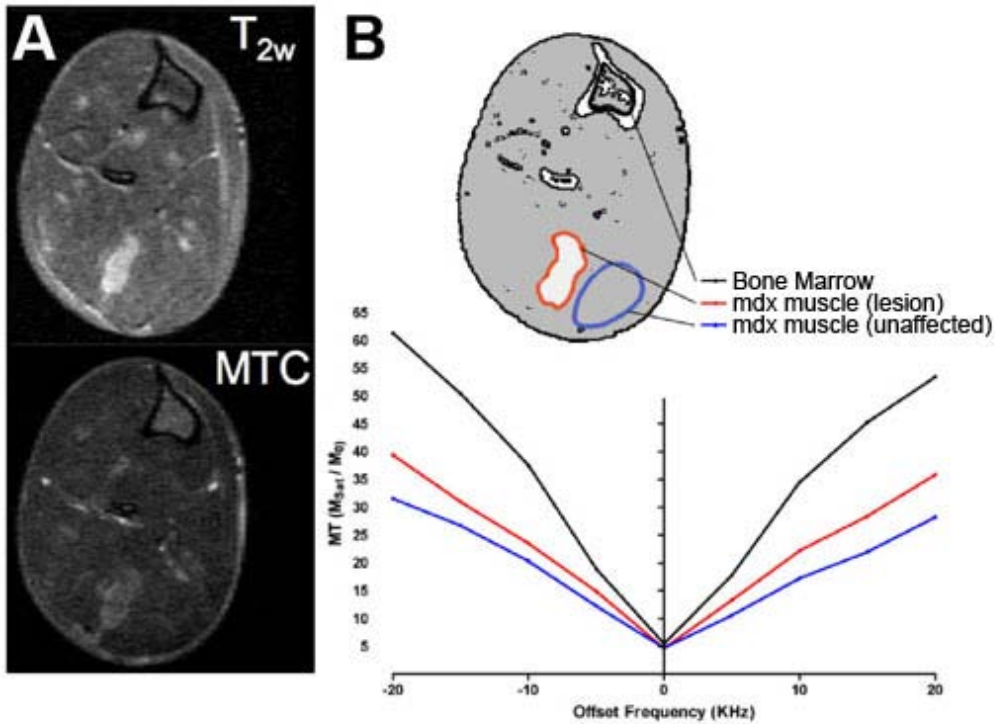


Figure 6-1. Typical T_2 and magnetization transfer contrast and the Z-Spectra from damaged and undamaged muscle. (a) T_2 weighted (upper) and MTC (lower) images of lower hindlimb of a young mdx mouse display the typical pathological contrast observed in younger acutely damaged dystrophic muscle. A representative Z-spectrum of ROIs in mdx muscle (b) reveals differences in MT of dystrophic tissue determined (by T_2 analysis; $T_2 > 29$ ms) to be lesions (red) versus seemingly unaffected regions (blue). To demonstrate the effect of high lipid content would have on MT an additional plot of the Z-spectra of bone marrow is included (black).

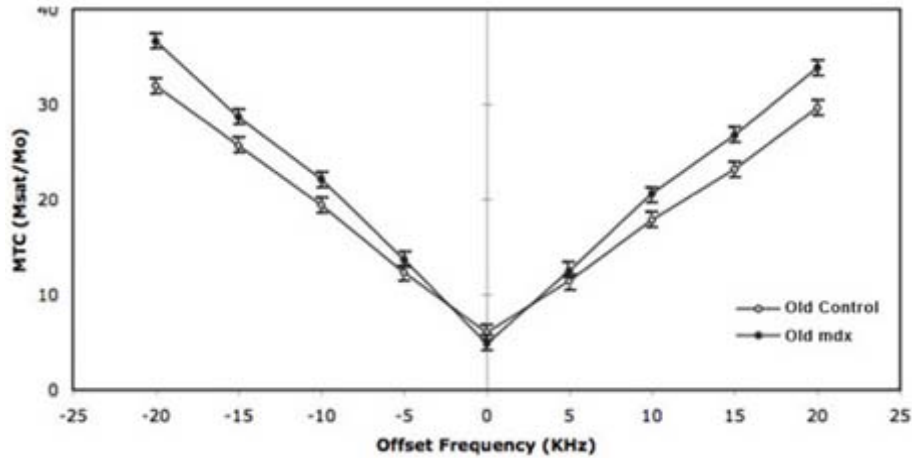


Figure 6-2. Z-spectra from the gastrocnemius muscles of old C57BL10 control and old mdx mice. The MT contrast is plotted as the mean $(M_{Sat}/M_0) \times 10^2$ (% signal retained following an MT presaturation pulse) as a function of offset frequency of the MT pulse ($\Delta = \omega_{RF} - \omega_0$; when $\Delta = 0$, the liquid pool is directly saturated). Data were collected with MT pulses at a range of offset frequencies ($\Delta = \pm 20,000$ Hz, $\pm 15,000$ Hz, $\pm 10,000$ Hz, $\pm 5,000$ Hz and 0 Hz). No asymmetry was observed in the Z-spectra of either mdx or control muscle. The lower mean MTR ($M_0 - M_{Sat}/M_0$) in mdx muscle was significantly different from controls with MT offset frequencies beyond ± 10 KHz, while 0 KHz and ± 5 KHz had considerable direct saturation effects on all muscles. I determined the measuring MT at -10 KHz alone would be sufficient for the detection of dystrophic pathology for future experiments.

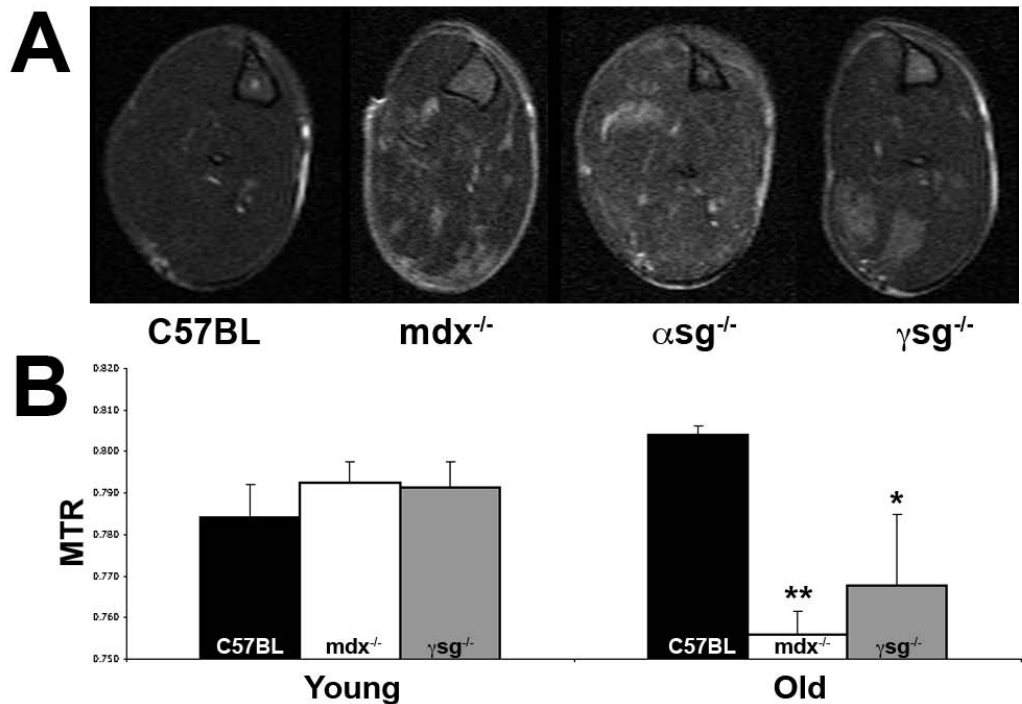


Figure 6-3. (a) Lesions in young dystrophic mice are distinctly visible in magnetization transfer (MT) contrast images and have a similar spatial distribution as damage observable in T_2 weighted images. While similar in trend in contrast, the relatively inverse indices T_2 and MTR did not always track with the same magnitude in damaged and seemingly unaffected dystrophic tissue, confirming that the contrast in the methods do arise from unique endogenous properties of the tissue. (b) While the MTR of the C57BL10 control gastrocnemius muscles have a trend of slight increase with age, the dystrophic muscles showed a significant reduction. The reduction in MTR observed in the older mdx and $gsg^{-/-}$ muscles were significant when compared to younger mice of the same strain (indicating the reduction was progressive) and were both significant when compared to age matched control muscle (indicating the reduction was due to pathology).

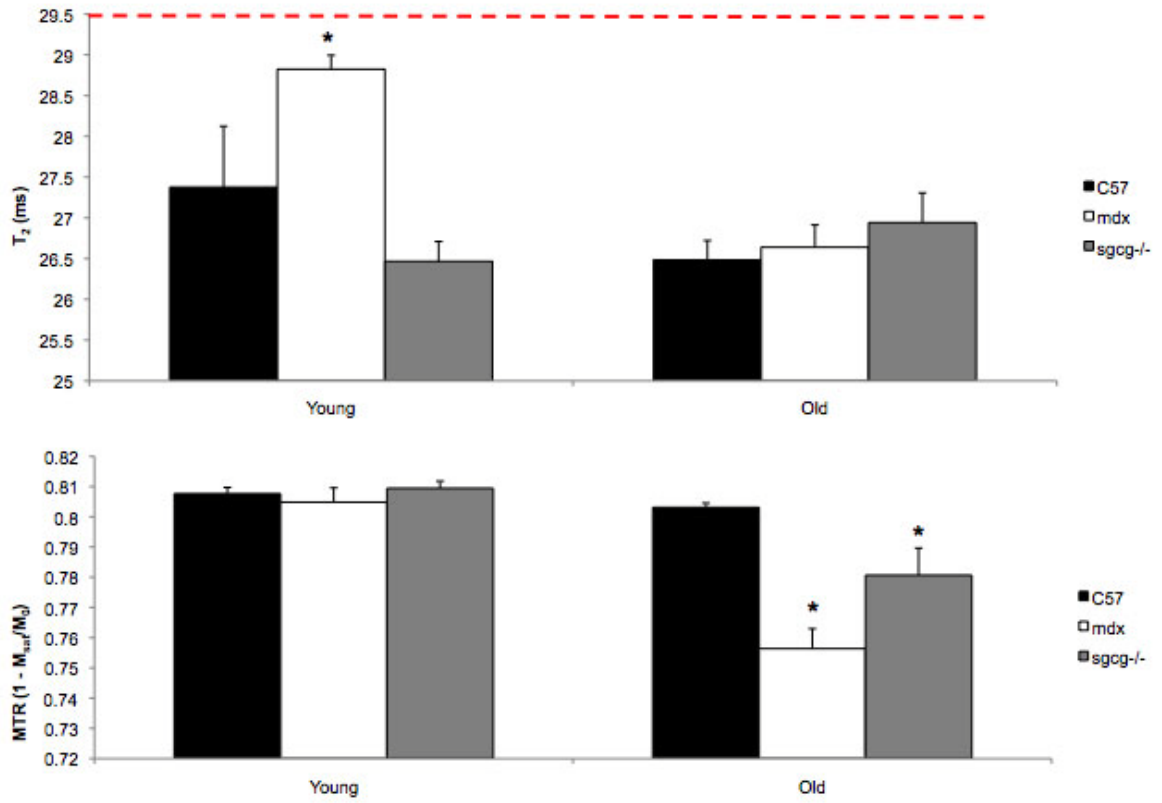


Figure 6-4. T₂ and MTR in unaffected (T₂ < 29 ms) GAS muscle.

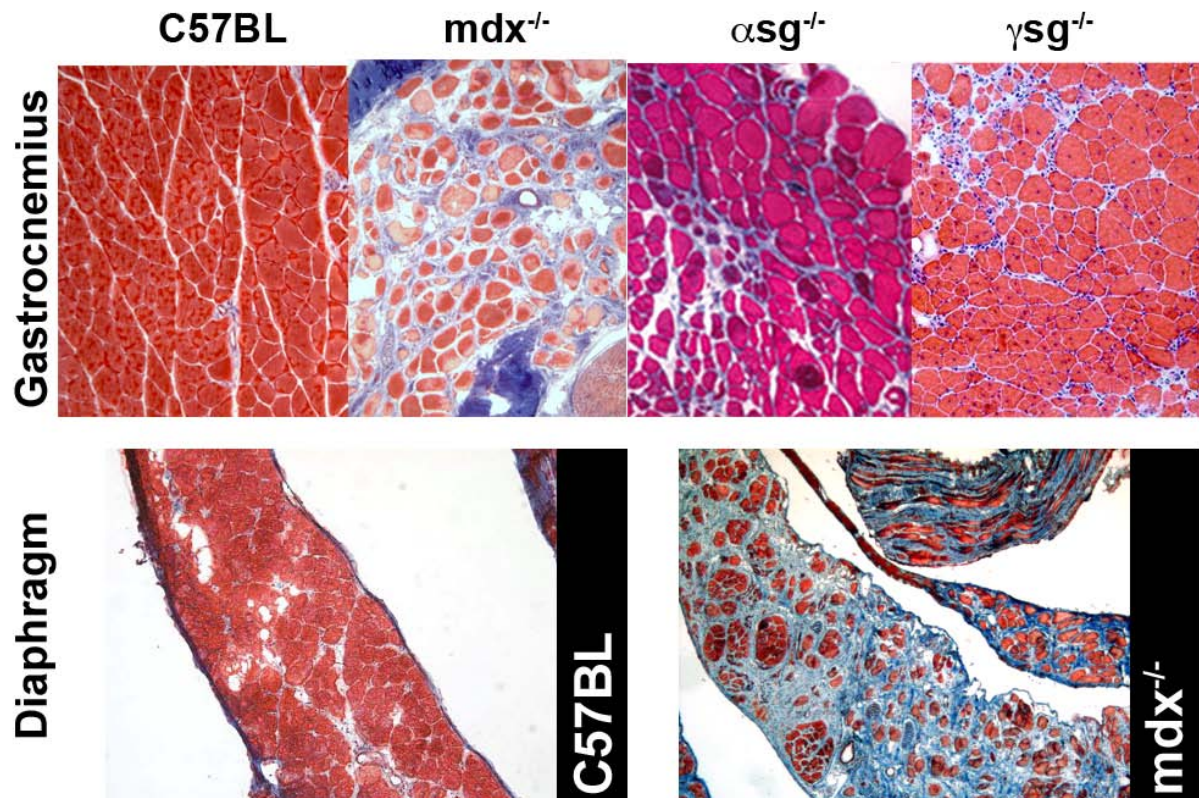


Figure 6-5. Extensive fibrosis was seen in the muscles of older (>1.5yr) dystrophic mice and is not observed in control C57BL10 mice. Here, Masson's trichrome stained thin sections (10 μ m) of gastrocnemius muscles (top row) show increased fibrotic collagen (staining blue) deposition between dystrophic muscle fibers. Severe fibrosis is commonly observed in the diaphragm muscle in muscular dystrophy and is seen in our murine models (lower panel).

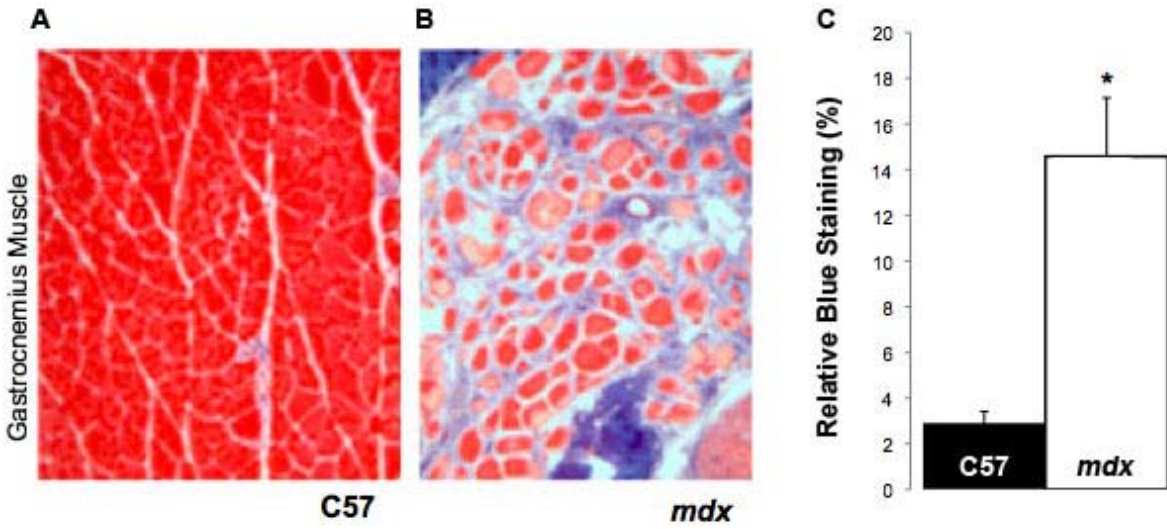


Figure 6-6. Extensive fibrosis was observed in the old *mdx* muscle as compared to the C57 control (a and b). Quantitative image analysis, using a color threshold to calculate the percentage of positive collagen (blue) staining, showed that this increase in collagen was significant (c).

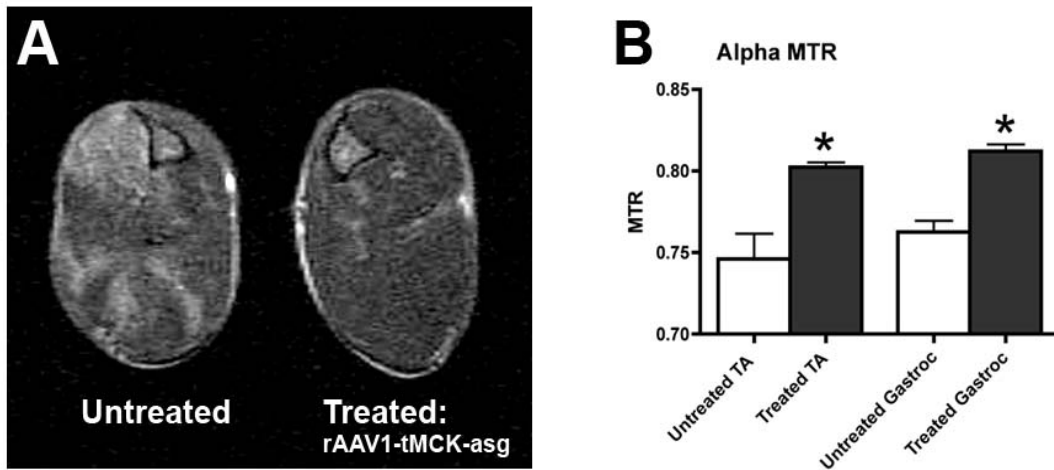


Figure 6-7. MT contrast was able to detect genetic correction of dystrophic muscle tissue. (a) The muscle of the treated limb showed homogeneous contrast similar to that of healthy control muscle, while the sham treatment limb displayed the patchy lesions that are commonly seen in young dystrophic tissue. (b) The MTR values of the TA and gastrocnemius muscles of the treated limb were significantly elevated as compared to the sham treatment limb and were similar to MTR values observed in healthy controls.

Table 6-1. Comparison of T₂ and MTR for TA and GAS muscles by age and strain

Muscle	Param.	Young C57	Old C57	Young <i>mdx</i>	Old <i>mdx</i>	Young <i>γsg</i> ^{-/-}	Old <i>γsg</i> ^{-/-}
TA	T ₂	26.34±0.56	25.30±0.36	27.48±0.69	27.67±0.67	27.54±0.64	27.63±1.18
	MTR	0.78±8.0E-3	0.81±3.6E-3	0.81±5.3E-3	0.78±67E-3	0.80±5.7E-3	0.78±8.8E-3
GAS	T ₂	28.28±0.32	26.66±0.29	31.29±0.43	27.05±0.31	29.33±0.82	28.51±1.24
	MTR	0.78±8.2E-3	0.80±2.3E-3	0.79±5.2E-3	0.76±5.7E-3	0.79±6.4E-3	0.77±1.7E-2

Table 6-2. T₂ and MTR for unaffected regions (T₂ < 29 ms) of TA and GAS muscles

Muscle	Param.	Young C57	Old C57	Young <i>mdx</i>	Old <i>mdx</i>	Young <i>γsg</i> ^{-/-}	Old <i>γsg</i> ^{-/-}
TA	T ₂	24.55±1.21	24.72±0.37	26.98±0.26	26.80±0.37	25.93±0.47	25.88±0.35
	MTR	0.81±5.0E-3	0.81±5.8E-3	0.81±4.8E-3	0.79±2.6E-3	0.80±5.3E-3	0.78±8.3E-3
GAS	T ₂	27.38±0.75	26.48±0.24	28.82±0.17	26.64±0.27	26.47±0.24	26.94±0.36
	MTR	0.81±2.1E-3	0.80±1.4E-3	0.81±4.7E-3	0.76±6.6E-3	0.81±2.4E-3	0.78±9.0E-3

CHAPTER 7 CONCLUSION

The muscular dystrophies are a collection of devastating genetic diseases that result in muscle wasting and currently no acceptable cure is available. Great efforts towards finding clinical solutions are underway and many promising avenues have been discovered. Whether it involves gene therapy, cell based treatment, pharmaceuticals or a combination of the above, advances in these fields are fueled by our collective understanding of basic muscle physiology and growth and repair mechanisms. It is only after fully understanding these underlying components, that we may develop truly elegant ways to help the body repair itself. In this dissertation I have presented a collection of non-invasive techniques that allow us to monitor basic processes in the recovery of damage in skeletal muscle and follow disease progression in models of muscular dystrophy. Each of the MR imaging modalities discussed (T_2 , diffusion, and MT) have individual strengths and weakness. We propose that used in concert, these imaging protocols allow the researcher to derive detailed information about spatial distribution of fiber damage, dynamic processes of remodeling following necrosis, and the pathology of chronic disease, including fibrosis (Figure 7-1), all without altering the tissue that they are trying to learn to repair. We have extended the observation that elevated T_2 corresponds to markers of fiber damage such as Evan's Blue dye uptake and other histological marker of damage such as immune cell infiltration, central myonuclei, and heterogeneous fiber diameter. Adding to this, diffusion weighted imaging holds information about the nature of muscle fiber structure, orientation, fat infiltration, swelling and dynamic processes of repair. In a chronic disease model, the aged dystrophic mice displayed unique magnetization transfer properties that

repeatedly identified acute damage, like T_2 weighted imaging, but also in areas where T_2 relaxation analysis failed to detect any differences despite overwhelming histological evidence showing a marked increase in extracellular matrix proteins (fibrosis). This was an especially valuable finding since fibrosis is particularly difficult to image with MR due to greatly shortened T_1 and T_2 relaxation times. In addition to the imaging modalities presented in this dissertation, it cannot be stressed enough the value of a protocol such as the downhill tread mill running to illicit a physiologically relevant, eccentric contraction induced, synchronized model of acute damage in skeletal muscle for the purpose of studying repair and remodeling in the tissue. This especially holds true in models of muscular dystrophy, where lesions are occurring seemly at random. The random spatial and random temporal flux of necrosis, inflammation and recovery introduces copious amounts of variation into such sensitive measures, such as the indices of diffusion. All together these non-invasive imaging techniques promise to guide our future work in developing effective treatments for the numerous forms of muscular dystrophy and will strengthen the background of knowledge for those with similar aspirations in pursuit of cures and treatments for other neuromuscular disorders.

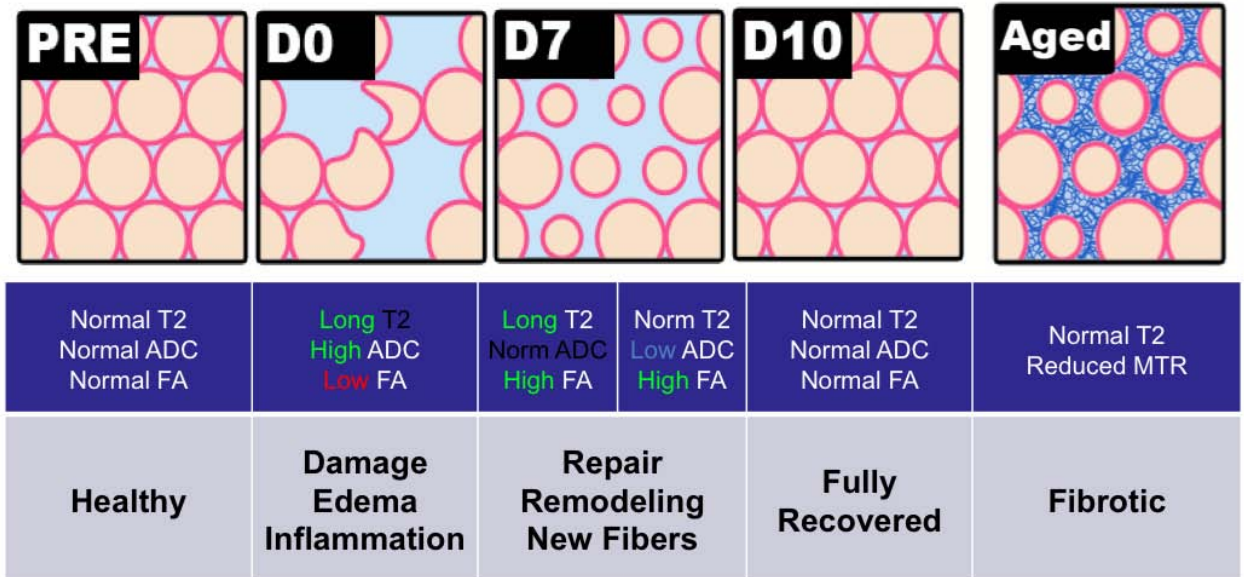


Figure 7-1. A model of multiple methods of MRI contrast at various stages of damage and disease progression is shown above. The first four columns represent the cycles of acute damage and repair that dystrophic muscle mouse tissue undergoes early in life. The first column represents normal healthy or unaffected muscle (PRE = Pre-injury), while the following show immediately after (D0= day 0), day 7 (D7), and day 10 (D10) after injury. The final column depicts the advanced progression of dystrophy in murine models, exhibiting heterogeneous fiber diameter and extensive fibrosis.

REFERENCES

1. Lexell J & Taylor CC (1989) Variability in muscle fibre areas in whole human quadriceps muscle. How much and why? *Acta Physiol Scand* 136:561-568.
2. O'Doherty DS, Schellinger D, & Raptopoulos V (1977) Computed tomographic patterns of pseudohypertrophic muscular dystrophy: preliminary results. *Journal of computer assisted tomography* 1:482-486.
3. Gersten J (1954) Ultrasonics and muscle disease. *American journal of physical medicine* 33:68-74.
4. Heckmatt JZ, Dubowitz V, & Leeman S (1980) Detection of pathological change in dystrophic muscle with B-scan ultrasound imaging. *Lancet* 1:1389-1390.
5. Weiss ES, *et al.* (1976) External detection and visualization of myocardial ischemia with ¹¹C-substrates in vitro and in vivo. *Circ Res* 39:24-32.
6. Scott JA, Rosenthal DI, & Brady TJ (1984) The evaluation of musculoskeletal disease with magnetic resonance imaging. *Radiol Clin North Am* 22:917-924.
7. Cope FW (1969) Nuclear magnetic resonance evidence using D₂O for structured water in muscle and brain. *Biophys J* 9:303-319.
8. Hilar T, Bolson EL, Hubka M, Sheehan FH, & Kushmerick MJ (2003) Three dimensional ultrasound analysis of fascicle orientation in human tibialis anterior muscle enables analysis of macroscopic torque at the cellular level. *Adv Exp Med Biol* 538:635-644; discussion 645.
9. Boesch C (2007) Role of proton MR for the study of muscle lipid metabolism.
10. Lodi R, *et al.* (1997) Correlative MR imaging and ³¹P-MR spectroscopy study in sarcoglycan deficient limb girdle muscular dystrophy. *Neuromuscul. Disord.* 7:505-511.
11. Ackerman JJ, Grove TH, Wong GG, Gadian DG, & Radda GK (1980) Mapping of metabolites in whole animals by ³¹P NMR using surface coils. *Nature* 283:167-170.
12. Vandeborne K, Walter G, Leigh J, & Goelman G (1993) pH heterogeneity during exercise in localized spectra from single human muscles. *Am J Physiol* 265:C1332-1339.
13. Studitsky AN (1964) Free Auto- and Homografts of Muscle Tissue in Experiments on Animals. *Ann N Y Acad Sci* 120:789-801.
14. Stevens J, *et al.* (2004) Muscle adaptations with immobilization and rehabilitation after ankle fracture. *Med Sci Sports Exerc* 36:1695-1701.

15. Frimel T, Walter G, Gibbs J, Gaidosh G, & Vandeborne K (2005) Noninvasive monitoring of muscle damage during reloading following limb disuse. *Muscle Nerve* 32:605-612.
16. Allen DL, Roy RR, & Edgerton VR (1999) Myonuclear domains in muscle adaptation and disease. *Muscle Nerve* 22:1350-1360.
17. Gundersen K & Bruusgaard JC (2008) Nuclear domains during muscle atrophy: nuclei lost or paradigm lost? *J Physiol* 586:2675-2681.
18. Mauro A (1961) Satellite cell of skeletal muscle fibers. *J Biophys Biochem Cytol* 9:493-495.
19. Partridge T (2009) Developmental biology: Skeletal muscle comes of age. *Nature* 460:584-585.
20. Schultz E (1985) Satellite cells in normal, regenerating and dystrophic muscle. *Adv Exp Med Biol* 182:73-84.
21. Qu-Petersen Z, *et al.* (2002) Identification of a novel population of muscle stem cells in mice: potential for muscle regeneration. *J. Cell Biol.* 157:851-864.
22. Péault, *et al.* (2007) Stem and Progenitor Cells in Skeletal Muscle Development, Maintenance, and Therapy. *Mol. Ther.*
23. Lepper C, Conway SJ, & Fan CM (2009) Adult satellite cells and embryonic muscle progenitors have distinct genetic requirements. *Nature* 460:627-631.
24. Funk WD, Ouellette M, & Wright WE (1991) Molecular biology of myogenic regulatory factors. *Mol Biol Med* 8:185-195.
25. Tedesco FS, Dellavalle A, Diaz-Manera J, Messina G, & Cossu G (2010) Repairing skeletal muscle: regenerative potential of skeletal muscle stem cells. *J Clin Invest* 120:11-19.
26. Zammit PS (2008) All muscle satellite cells are equal, but are some more equal than others? *J Cell Sci* 121:2975-2982.
27. McElhinny AS, Kazmierski ST, Labeit S, & Gregorio CC (2003) Nebulin: the nebulous, multifunctional giant of striated muscle. *Trends Cardiovasc Med* 13:195-201.
28. Friden J & Lieber RL (1992) Structural and mechanical basis of exercise-induced muscle injury. *Med Sci Sports Exerc* 24:521-530.
29. McNeil PL & Khakee R (1992) Disruptions of muscle fiber plasma membranes. Role in exercise-induced damage. *Am J Pathol* 140:1097-1109.

30. Costa ML, Escaleira R, Cataldo A, Oliveira F, & Mermelstein CS (2004) Desmin: molecular interactions and putative functions of the muscle intermediate filament protein. *Braz J Med Biol Res* 37:1819-1830.
31. Ervasti JM (2003) Costameres: the Achilles' heel of Herculean muscle. *J Biol Chem* 278:13591-13594.
32. Kobayashi YM, *et al.* (2008) Sarcolemma-localized nNOS is required to maintain activity after mild exercise [Supplementary Information]. *Nature* 456:511-515.
33. Goodhart SP & Globus JH (1918) On the nature of muscular dystrophies. *Neurol. Bull.* 1:386.
34. Erb W (1884) Über die "juvenile Form" der progressiven Muskelatrophie und ihre Beziehungen zur sogehanten Pseudohypertrophie der Muskeln. *Deutsch Archiv Klin Med* 34:467-519.
35. Duchenne G (1868) Studies on pseudohypertrophic muscular paralysis or myosclerotic paralysis. *Arch Neurol.*
36. Funsten R (1923) Clinical study of thirty cases of muscular dystrophy. *J Bone Joint Surg Am.* 5:190-203.
37. Lovering R, Porter N, & Bloch R (2005) The muscular dystrophies: from genes to therapies. *Phys Ther* 85:1372-1388.
38. Liu J, *et al.* (1998) Dysferlin, a novel skeletal muscle gene, is mutated in Miyoshi myopathy and limb girdle muscular dystrophy. *Nat Genet* 20:31-36.
39. Udd B, *et al.* (1998) Tibial muscular dystrophy--from clinical description to linkage on chromosome 2q31. *Neuromuscul Disord* 8:327-332.
40. Straub V, *et al.* (2000) Contrast agent-enhanced magnetic resonance imaging of skeletal muscle damage in animal models of muscular dystrophy. *Magnetic resonance in medicine : official journal of the Society of Magnetic Resonance in Medicine / Society of Magnetic Resonance in Medicine* 44:655-659.
41. Bulfield G, Siller W, Wight P, & Moore K (1984) X chromosome-linked muscular dystrophy (mdx) in the mouse. *PNAS* 81:1189-1192.
42. Willmann R, Possekkel S, Dubach-Powell J, Meier T, & Ruegg MA (2009) Mammalian animal models for Duchenne muscular dystrophy. *Neuromuscul Disord* 19:241-249.
43. Araki E, *et al.* (1997) Targeted disruption of exon 52 in the mouse dystrophin gene induced muscle degeneration similar to that observed in Duchenne muscular dystrophy. *Biochem Biophys Res Commun* 238:492-497.

44. Cooper BJ & Valentine BA (1988) X-linked muscular dystrophy in the dog. *Trends Genet* 4:30.
45. Valentine BA, *et al.* (1992) Canine X-linked muscular dystrophy as an animal model of Duchenne muscular dystrophy: a review. *Am J Med Genet* 42:352-356.
46. Allamand V & Campbell KP (2000) Animal models for muscular dystrophy: valuable tools for the development of therapies. *Hum. Mol. Genet.* 9:2459-2467.
47. Shimatsu Y, *et al.* (2003) Canine X-linked muscular dystrophy in Japan (CXMDJ). *Exp Anim* 52:93-97.
48. Shimatsu Y, *et al.* (2005) Major clinical and histopathological characteristics of canine X-linked muscular dystrophy in Japan, CXMDJ. *Acta Myol* 24:145-154.
49. Yugeta N, *et al.* (2006) Cardiac involvement in Beagle-based canine X-linked muscular dystrophy in Japan (CXMDJ): electrocardiographic, echocardiographic, and morphologic studies. *BMC Cardiovasc Disord* 6:47.
50. Nigro V, *et al.* (1997) Identification of the Syrian hamster cardiomyopathy gene. *Hum Mol Genet* 6:601-607.
51. Straub V, *et al.* (1998) Molecular pathogenesis of muscle degeneration in the delta-sarcoglycan-deficient hamster. *Am J Pathol* 153:1623-1630.
52. Ferrer A, Foster H, Wells KE, Dickson G, & Wells DJ (2004) Long-term expression of full-length human dystrophin in transgenic mdx mice expressing internally deleted human dystrophins. *Gene Ther* 11:884-893.
53. Tennyson CN, Klamut HJ, & Worton RG (1995) The human dystrophin gene requires 16 hours to be transcribed and is cotranscriptionally spliced. *Nat Genet* 9:184-190.
54. Gilbert R, *et al.* (2003) Prolonged dystrophin expression and functional correction of mdx mouse muscle following gene transfer with a helper-dependent (guttled) adenovirus-encoding murine dystrophin. *Hum Mol Genet* 12:1287-1299.
55. Cordier L, *et al.* (2000) Rescue of skeletal muscles of gamma-sarcoglycan-deficient mice with adeno-associated virus-mediated gene transfer. *Mol. Ther.* 1:119-129.
56. Pacak CA, *et al.* (2007) Long-term skeletal muscle protection after gene transfer in a mouse model of LGMD-2D. *Mol. Ther.* 15:1775-1781.
57. Li J, *et al.* (1999) rAAV vector-mediated sarcoglycan gene transfer in a hamster model for limb girdle muscular dystrophy. *Gene Ther.* 6:74-82.

58. Mendell JR, *et al.* (2009) Limb-girdle muscular dystrophy type 2D gene therapy restores alpha-sarcoglycan and associated proteins. *Ann Neurol* 66:290-297.
59. Perkins KJ & Davies KE (2002) The role of utrophin in the potential therapy of Duchenne muscular dystrophy. *Neuromuscul Disord* 12 Suppl 1:S78-89.
60. Gramolini AO, *et al.* (1998) Muscle and neural isoforms of agrin increase utrophin expression in cultured myotubes via a transcriptional regulatory mechanism. *J Biol Chem* 273:736-743.
61. Barton ER, Morris L, Musaro A, Rosenthal N, & Sweeney HL (2002) Muscle-specific expression of insulin-like growth factor I counters muscle decline in mdx mice. *J. Cell Biol.* 157:137-148.
62. Shavlakadze T, White J, Hoh J, Rosenthal N, & Grounds M (2004) Targeted expression of insulin-like growth factor-I reduces early myofiber necrosis in dystrophic mdx mice. *Mol Ther* 10:829-843.
63. Wheeler TM (2008) Myotonic dystrophy: therapeutic strategies for the future. *Neurotherapeutics* 5:592-600.
64. Fisher I, *et al.* (2005) Prednisolone-induced changes in dystrophic skeletal muscle. *Sheng Wu Gong Cheng Xue Bao* 19:834-836.
65. Balaban B, Matthews DJ, Clayton GH, & Carry T (2005) Corticosteroid treatment and functional improvement in Duchenne muscular dystrophy: long-term effect. *American journal of physical medicine & rehabilitation / Association of Academic Physiatrists* 84:843-850.
66. Angelini C (2007) The role of corticosteroids in muscular dystrophy: a critical appraisal. *Muscle Nerve* 36:424-435.
67. Arbogast S, *et al.* (2006) Bowman-Birk inhibitor concentrate prevents atrophy, weakness, and oxidative stress in soleus muscle of hindlimb-unloaded mice. *J. Appl. Physiol.* 102:956-964.
68. Nelson SF, Crosbie RH, Miceli MC, & Spencer MJ (2009) Emerging genetic therapies to treat Duchenne muscular dystrophy. *Curr Opin Neurol* 22:532-538.
69. Welch, *et al.* (2007) PTC124 targets genetic disorders caused by nonsense mutations. *Nature*.
70. Lu QL, *et al.* (2003) Functional amounts of dystrophin produced by skipping the mutated exon in the mdx dystrophic mouse. *Nat Med* 9:1009-1014.
71. Yin H, Lu Q, & Wood M (2008) Effective Exon Skipping and Restoration of Dystrophin Expression by Peptide Nucleic Acid Antisense Oligonucleotides in mdx Mice. *Mol. Ther.* 16:38-45.

72. Williams JH, Schray RC, Sirsi SR, & Lutz GJ (2008) Nanopolymers improve delivery of exon skipping oligonucleotides and concomitant dystrophin expression in skeletal muscle of mdx mice. *BMC Biotechnol* 8:35.
73. Sirsi SR, Schray RC, Wheatley MA, & Lutz GJ (2009) Formulation of polylactide-co-glycolic acid nanospheres for encapsulation and sustained release of poly(ethylene imine)-poly(ethylene glycol) copolymers complexed to oligonucleotides. *J Nanobiotechnology* 7:1.
74. Rimessi P, *et al.* (2009) Cationic PMMA nanoparticles bind and deliver antisense oligoribonucleotides allowing restoration of dystrophin expression in the mdx mouse. *Mol Ther* 17:820-827.
75. Goyenvalle A, Babbs A, van Ommen GJ, Garcia L, & Davies KE (2009) Enhanced exon-skipping induced by U7 snRNA carrying a splicing silencer sequence: Promising tool for DMD therapy. *Mol Ther* 17:1234-1240.
76. van Deutekom JC, *et al.* (2007) Local dystrophin restoration with antisense oligonucleotide PRO051. *N Engl J Med* 357:2677-2686.
77. Beroud C, *et al.* (2007) Multiexon skipping leading to an artificial DMD protein lacking amino acids from exons 45 through 55 could rescue up to 63% of patients with Duchenne muscular dystrophy. *Hum Mutat* 28:196-202.
78. Heemskerk AM, Strijkers GJ, Drost MR, van Bochove GS, & Nicolay K (2007) Skeletal muscle degeneration and regeneration after femoral artery ligation in mice: monitoring with diffusion MR imaging. *Radiology* 243:413-421.
79. Skuk D (2004) Myoblast transplantation for inherited myopathies: a clinical approach. *Expert Opin Biol Ther* 4:1871-1885.
80. Galvez BG, *et al.* (2006) Complete repair of dystrophic skeletal muscle by mesoangioblasts with enhanced migration ability. *J Cell Biol* 174:231-243.
81. Sampaolesi M, *et al.* (2006) Mesoangioblast stem cells ameliorate muscle function in dystrophic dogs. *Nature* 444:574-579.
82. MacReady N (2009) The murky ethics of stem-cell tourism. *Lancet Oncol* 10:317-318.
83. Spurney CF, *et al.* (2009) Preclinical drug trials in the mdx mouse: assessment of reliable and sensitive outcome measures. *Muscle Nerve* 39:591-602.
84. O'Doherty DS, Schellinger D, & Raptopoulos V (1977) Computed tomographic patterns of pseudohypertrophic muscular dystrophy: preliminary results. *J Comput Assist Tomogr* 1:482-486.
85. Gersten JW (1954) Ultrasonics and muscle disease. *Am J Phys Med* 33:68-74.

86. Carr HY & Purcell EM (1954) Effects of Diffusion on Free Precession in Nuclear Magnetic Resonance Experiments. *Phys Rev* 94:630-638.
87. Meiboom S & Gill D (1958) Modified Spin-Echo Method for Measuring Nuclear Relaxation Times. *Rev Sci Instrum* 29:688-691.
88. Gatehouse PD & Bydder GM (2003) Magnetic resonance imaging of short T2 components in tissue. *Clinical radiology* 58:1-19.
89. Harrison R, Bronskill MJ, & Henkelman RM (1995) Magnetization transfer and T2 relaxation components in tissue. *Magnetic resonance in medicine : official journal of the Society of Magnetic Resonance in Medicine / Society of Magnetic Resonance in Medicine* 33:490-496.
90. Henkelman RM, Stanisz GJ, & Graham S (2001) Magnetization transfer in MRI: a review. *NMR Biomed* 14:57-64.
91. Traore A, Foucat L, & Renou JP (2000) 1H-nmr study of water dynamics in hydrated collagen: transverse relaxation-time and diffusion analysis. *Biopolymers* 53:476-483.
92. Wolff SD & Balaban RS (1989) Magnetization transfer contrast (MTC) and tissue water proton relaxation in vivo. *Magnetic resonance in medicine : official journal of the Society of Magnetic Resonance in Medicine / Society of Magnetic Resonance in Medicine* 10:135-144.
93. Guo J, Erickson R, Trouard T, Galons J, & Gillies R (2003) Magnetization transfer contrast imaging in Niemann pick type C mouse liver. *J Magn Reson Imaging* 18:321-327.
94. STETTEN MR (1949) Some aspects of the metabolism of hydroxyproline, studied with the aid of isotopic nitrogen. *J. Biol. Chem.* 181:31-37.
95. GREEN NM & LOWTHER DA (1959) Formation of collagen hydroxyproline in vitro. *Biochem J* 71:55-66.
96. Pettegrew J, Minshew N, & Feit H (1984) 31P-NMR studies of normal and dystrophic chicken muscle. *Muscle Nerve* 7:442-446.
97. Dunn JF, Frostick S, Brown G, & Radda GK (1991) Energy status of cells lacking dystrophin: an in vivo/in vitro study of mdx mouse skeletal muscle. *Biochim Biophys Acta* 1096:115-120.
98. Huang Y, *et al.* (1994) Quantitative MR relaxometry study of muscle composition and function in Duchenne muscular dystrophy. *Journal of magnetic resonance imaging : JMRI* 4:59-64.

99. Gong QY, *et al.* (2000) Estimation of body composition in muscular dystrophy by MRI and stereology. *Journal of magnetic resonance imaging : JMRI* 12:467-475.
100. Fleckenstein JL, Canby RC, Parkey RW, & Peshock RM (1988) Acute effects of exercise on MR imaging of skeletal muscle in normal volunteers. *AJR American journal of roentgenology* 151:231-237.
101. Mercuri E, *et al.* (2007) Muscle MRI in inherited neuromuscular disorders: past, present, and future. *Journal of magnetic resonance imaging : JMRI* 25:433-440.
102. Murphy WA, Totty WG, & Carroll JE (1986) MRI of normal and pathologic skeletal muscle. *AJR American journal of roentgenology* 146:565-574.
103. Le Rumeur E, De Certaines J, Toulouse P, & Rochcongar P (1987) Water phases in rat striated muscles as determined by T2 proton NMR relaxation times. *Magn Reson Med* 5:267-272.
104. Hazlewood CF, Chang DC, Nichols BL, & Woessner DE (1974) Nuclear magnetic resonance transverse relaxation times of water protons in skeletal muscle. *Biophys J* 14:583-606.
105. Saab G, Thompson R, & Marsh G (1999) Multicomponent T2 relaxation of in vivo skeletal muscle. *Magn Reson Med* 42:150-157.
106. Fenrich F, Beaulieu C, & Allen P (2001) Relaxation times and microstructures. *NMR Biomed* 14:133-139.
107. Cole WC, LeBlanc AD, & Jhingran SG (1993) The origin of biexponential T2 relaxation in muscle water. *Magnetic resonance in medicine : official journal of the Society of Magnetic Resonance in Medicine / Society of Magnetic Resonance in Medicine* 29:19-24.
108. Heemskerk AM, *et al.* (2006) DTI-based assessment of ischemia-reperfusion in mouse skeletal muscle. *Magnetic resonance in medicine : official journal of the Society of Magnetic Resonance in Medicine / Society of Magnetic Resonance in Medicine* 56:272-281.
109. Gilbert RJ, *et al.* (2006) Mapping complex myoarchitecture in the bovine tongue with diffusion-spectrum magnetic resonance imaging. *Biophys J* 91:1014-1022.
110. Gilbert RJ & Napadow VJ (2005) Three-dimensional muscular architecture of the human tongue determined in vivo with diffusion tensor magnetic resonance imaging. *Dysphagia* 20:1-7.
111. Kim S, Barnett A, Pierpaoli C, & Chi-Fishman G (2007) Three-dimensional mapping of lingual myoarchitecture by diffusion tensor MRI. *NMR in biomedicine*.

112. Weiss S, *et al.* (2006) Three-dimensional fiber architecture of the nonpregnant human uterus determined ex vivo using magnetic resonance diffusion tensor imaging. *Anat Rec A Discov Mol Cell Evol Biol* 288:84-90.
113. Sosnovik DE, Wang R, Dai G, Reese TG, & Wedeen VJ (2009) Diffusion MR tractography of the heart. *J Cardiovasc Magn Reson* 11:47.
114. Reese TG, *et al.* (1995) Imaging myocardial fiber architecture in vivo with magnetic resonance. *Magn Reson Med* 34:786-791.
115. Rohmer D, Sitek A, & Gullberg GT (2007) Reconstruction and visualization of fiber and laminar structure in the normal human heart from ex vivo diffusion tensor magnetic resonance imaging (DTMRI) data. *Invest Radiol* 42:777-789.
116. Damon BM, Ding Z, Anderson AW, Freyer AS, & Gore JC (2002) Validation of diffusion tensor MRI-based muscle fiber tracking. *Magnetic resonance in medicine : official journal of the Society of Magnetic Resonance in Medicine / Society of Magnetic Resonance in Medicine* 48:97-104.
117. Lansdown DA, Ding Z, Wadington M, Hornberger JL, & Damon BM (2007) Quantitative diffusion tensor MRI-based fiber tracking of human skeletal muscle. *J Appl Physiol* 103:673-681.
118. Heemskerk AM, Sinha TK, Wilson KJ, Ding Z, & Damon BM (2010) Repeatability of DTI-based skeletal muscle fiber tracking. *NMR Biomed.*
119. Yoshioka H, *et al.* (1994) Acute change of exercised muscle using magnetization transfer contrast MR imaging. *Magn Reson Med* 12:991-997.
120. Mattila KT, *et al.* (1995) Magnetic resonance imaging and magnetization transfer in experimental myonecrosis in the rat. *Magnetic resonance in medicine : official journal of the Society of Magnetic Resonance in Medicine / Society of Magnetic Resonance in Medicine* 33:185-192.
121. Hatakenaka M (2003) Effect of muscular contraction on magnetization transfer detected at 1.5 T. *Magnetic resonance in medical sciences : MRMS : an official journal of Japan Society of Magnetic Resonance in Medicine* 2:151-154.
122. Vahlensieck M, Gieseke J, Traber F, & Schild H (1999) The quantification of the magnetization transfer contrast (MTC) effect by calculating MT quotients: does it yield additional information for the differentiation of benign and malignant diseases of the locomotor apparatus? *Rofo* 171:468-472.
123. Matsumura K, *et al.* (1988) Proton spin-lattice relaxation time of Duchenne dystrophy skeletal muscle by magnetic resonance imaging. *Muscle Nerve* 11:97-102.

124. Misra LK & Narayana PA (1989) In vivo T1 characterization of genetically induced muscle atrophy. *Magn Reson Med* 7:277-282.
125. McIntosh LM, Baker RE, & Anderson JE (1998) Magnetic resonance imaging of regenerating and dystrophic mouse muscle. *Biochem Cell Biol* 76:532-541.
126. Chang DC, Misra LK, Beall PT, Fanguy RC, & Hazlewood CF (1981) Nuclear magnetic resonance study of muscle water protons in muscular dystrophy of chickens. *J Cell Physiol* 107:139-145.
127. Thibaud J-L, *et al.* (2007) Characterization of dystrophic muscle in golden retriever muscular dystrophy dogs by nuclear magnetic resonance imaging. *Neuromuscul. Disord.* 17:575-584.
128. Foley JM, Jayaraman RC, Prior BM, Pivarnik JM, & Meyer RA (1999) MR measurements of muscle damage and adaptation after eccentric exercise. *J Appl Physiol* 87:2311-2318.
129. Ababneh Z, *et al.* (2005) Biexponential Parameterization of Diffusion and T2 Relaxation Decay Curves in a Rat Muscle Edema Model: Decay Curve Components and Water Compartments. *Magnetic Resonance in Medicine.*
130. Fan R & Does M (2007) Compartmental relaxation and diffusion tensor imaging measurements in vivo in lambda-carrageenan-induced edema in rat skeletal muscle. *NMR in biomedicine.*
131. Sijens PE, *et al.* (2007) MR spectroscopy and diffusion tensor imaging of the brain in congenital muscular dystrophy with merosin deficiency: metabolite level decreases, fractional anisotropy decreases, and apparent diffusion coefficient increases in the white matter. *Brain Dev* 29:317-321.
132. Schick F (1996) Pulsed magnetization transfer contrast MRI by a sequence with water selective excitation. *Journal of computer assisted tomography* 20:73-79.
133. McDaniel JD, *et al.* (1999) Magnetization transfer imaging of skeletal muscle in autosomal recessive limb girdle muscular dystrophy. *Journal of computer assisted tomography* 23:609-614.
134. Dunn JF & Zaim-Wadghiri Y (1999) Quantitative magnetic resonance imaging of the mdx mouse model of Duchenne muscular dystrophy. *Muscle Nerve* 22:1367-1371.
135. Pastoret C & Sebillle A (1995) mdx mice show progressive weakness and muscle deterioration with age. *J Neurol Sci* 129:97-105.
136. Head SI, Williams DA, & Stephenson DG (1992) Abnormalities in structure and function of limb skeletal muscle fibres of dystrophic mdx mice. *Proc Biol Sci* 248:163-169.

137. Saab G, Thompson RT, & Marsh GD (2000) Effects of exercise on muscle transverse relaxation determined by MR imaging and in vivo relaxometry. *J. Appl. Physiol.* 88:226-233.
138. Heemskerk AM, Strijkers GJ, Vilanova A, Drost MR, & Nicolay K (2005) Determination of mouse skeletal muscle architecture using three-dimensional diffusion tensor imaging. *Magnetic resonance in medicine : official journal of the Society of Magnetic Resonance in Medicine / Society of Magnetic Resonance in Medicine* 53:1333-1340.
139. Morrison J, Lu QL, Pastoret C, Partridge T, & Bou-Gharios G (2000) T-cell-dependent fibrosis in the mdx dystrophic mouse. *Lab Invest* 80:881-891.
140. Vial C, *et al.* (2008) Skeletal muscle cells express the profibrotic cytokine connective tissue growth factor (CTGF/CCN2), which induces their dedifferentiation. *J Cell Physiol* 215:410-421.
141. Hack AA, *et al.* (1998) Gamma-sarcoglycan deficiency leads to muscle membrane defects and apoptosis independent of dystrophin. *J. Cell Biol.* 142:1279-1287.
142. Barton-Davis E (2006) Impact of sarcoglycan complex on mechanical signal transduction in murine skeletal muscle. *Am J Physiol Cell Physiol* 290:C411-419.
143. Childers MK, *et al.* (2002) Eccentric contraction injury in dystrophic canine muscle. *Archives of physical medicine and rehabilitation* 83:1572-1578.
144. Edwards RH, Newham DJ, Jones DA, & Chapman SJ (1984) Role of mechanical damage in pathogenesis of proximal myopathy in man. *Lancet* 1:548-552.
145. Brussee V, Tardif F, & Tremblay JP (1997) Muscle fibers of mdx mice are more vulnerable to exercise than those of normal mice. *Neuromuscul Disord* 7:487-492.
146. Whitehead NP, Streamer M, Lusambili LI, Sachs F, & Allen DG (2006) Streptomycin reduces stretch-induced membrane permeability in muscles from mdx mice. *Neuromuscul Disord* 16:845-854.
147. Lynch GS, Fary CJ, & Williams DA (1997) Quantitative measurement of resting skeletal muscle $[Ca^{2+}]_i$ following acute and long-term downhill running exercise in mice. *Cell Calcium* 22:373-383.
148. Saupe N, White LM, Stainsby J, Tomlinson G, & Sussman MS (2009) Diffusion tensor imaging and fiber tractography of skeletal muscle: optimization of B value for imaging at 1.5 T. *AJR American journal of roentgenology* 192:W282-290.

149. Fisher MJ, Meyer RA, Adams GR, Foley JM, & Potchen EJ (1990) Direct relationship between proton T2 and exercise intensity in skeletal muscle MR images. *Investigative radiology* 25:480-485.
150. Walter G, Cordier L, Bloy D, & Sweeney H (2005) Noninvasive monitoring of gene correction in dystrophic muscle. *Magn Reson Med* 54:1369-1376.
151. Butterfield TA & Herzog W (2005) Is the force-length relationship a useful indicator of contractile element damage following eccentric exercise? *Journal of biomechanics* 38:1932-1937.
152. Hazlewood CF, Nichols BL, & Chamberlain NF (1969) Evidence for the existence of a minimum of two phases of ordered water in skeletal muscle. *Nature* 222:747-750.
153. Belton PS, Jackson RR, & Packer KJ (1972) Pulsed NMR studies of water in striated muscle. I. Transverse nuclear spin relaxation times and freezing effects. *Biochim Biophys Acta* 286:16-25.
154. Graham SJ, Stanchev PL, & Bronskill MJ (1996) Criteria for analysis of multicomponent tissue T2 relaxation data. *Magnetic resonance in medicine : official journal of the Society of Magnetic Resonance in Medicine / Society of Magnetic Resonance in Medicine* 35:370-378.
155. Gambarota G, Cairns BE, Berde CB, & Mulkern RV (2001) Osmotic effects on the T2 relaxation decay of in vivo muscle. *Magnetic resonance in medicine : official journal of the Society of Magnetic Resonance in Medicine / Society of Magnetic Resonance in Medicine* 46:592-599.
156. Whittall KP & Mackay AL (1989) Quantitative Interpretation of Nmr Relaxation Data. *Journal of Magnetic Resonance* 84:134-152.
157. Andrews T, Lancaster J, Dodd S, Contreras-Sesvold C, & Fox P (2005) Testing the three-pool white matter model adapted for use with T2 relaxometry. *Magn Reson Med* 54:449-454.
158. Oh J, Han E, Pelletier D, & Nelson S (2006) Measurement of in vivo multi-component T2 relaxation times for brain tissue using multi-slice T2 prep at 1.5 and 3 T. *Magn Reson Med* 24:33-43.
159. Fullerton GD (1982) Basic concepts for nuclear magnetic resonance imaging. *Magn Reson Med* 1:39-55.
160. Fung BM & Puon PS (1981) Nuclear magnetic resonance transverse relaxation in muscle water. *Biophys J* 33:27-37.
161. Frimel T, *et al.* (2005) A model of muscle atrophy using cast immobilization in mice. *Muscle Nerve* 32:672-674.

162. Bansal D, *et al.* (2003) Defective membrane repair in dysferlin-deficient muscular dystrophy. *Nature* 423:168-172.
163. Dula AN, Gochberg DF, & Does MD (2009) Optimal echo spacing for multi-echo imaging measurements of Bi-exponential T2 relaxation. *J Magn Reson* 196:149-156.
164. Cleveland GG, Chang DC, Hazlewood CF, & Rorschach HE (1976) Nuclear magnetic resonance measurement of skeletal muscle: anisotropy of the diffusion coefficient of the intracellular water. *Biophys J* 16:1043-1053.
165. Galbán CJ, Maderwald S, Uffmann K, de Greiff A, & Ladd ME (2004) Diffusive sensitivity to muscle architecture: a magnetic resonance diffusion tensor imaging study of the human calf. *Eur J Appl Physiol* 93:253-262.
166. Galbán CJ, Maderwald S, Uffmann K, & Ladd ME (2005) A diffusion tensor imaging analysis of gender differences in water diffusivity within human skeletal muscle. *NMR in biomedicine* 18:489-498.
167. van Doorn A, Bovendeerd PH, Nicolay K, Drost MR, & Janssen JD (1996) Determination of muscle fibre orientation using Diffusion-Weighted MRI. *European journal of morphology* 34:5-10.
168. Sinha S, Sinha U, & Edgerton VR (2006) In vivo diffusion tensor imaging of the human calf muscle. *Journal of magnetic resonance imaging : JMRI* 24:182-190.
169. Zaraiskaya T, Kumbhare D, & Noseworthy MD (2006) Diffusion tensor imaging in evaluation of human skeletal muscle injury. *Journal of magnetic resonance imaging : JMRI* 24:402-408.
170. Saotome T, Sekino M, Eto F, & Ueno S (2006) Evaluation of diffusional anisotropy and microscopic structure in skeletal muscles using magnetic resonance. *Magn Reson Med* 24:19-25.
171. Zhang J, Zhang G, Morrison B, Mori S, & Sheikh KA (2008) Magnetic resonance imaging of mouse skeletal muscle to measure denervation atrophy. *Exp Neurol* 212:448-457.
172. Chang LS (1996) Chemical modification of notexin from *Notechis scutatus scutatus* (Australian tiger snake) venom with pyridoxal-5'-phosphate. *J Protein Chem* 15:473-480.
173. Menke A & Jockusch H (1991) Decreased osmotic stability of dystrophin-less muscle cells from the mdx mouse. *Nature* 349:69-71.
174. Stedman HH, *et al.* (1991) The mdx mouse diaphragm reproduces the degenerative changes of Duchenne muscular dystrophy. *Nature* 352:536-539.

175. Morizumi H, Hizawa K, Nunomura S, & li K (1984) Comparative study of alterations of skeletal muscle in Duchenne muscular dystrophy and polymyositis. *Acta Pathol Jpn* 34:1221-1242.
176. Blau H, Webster C, & Pavlath G (1983) Defective myoblasts identified in Duchenne muscular dystrophy. *PNAS* 80:4856-4860.
177. Alexakis, Partridge, & Bou-Gharios (2007) Implication of the satellite cell in dystrophic muscle fibrosis: a self perpetuating mechanism of collagen over-production. *Am J Physiol Cell Physiol*.
178. Loesberg AC, Kormano M, & Lipton MJ (1993) Magnetization transfer imaging of normal and abnormal liver at 0.1 T. *Investigative radiology* 28:726-731.
179. Louie E, Gochberg D, Does M, & Damon B (2008) Transverse relaxation and magnetization transfer in skeletal muscle: Effect of pH. *Magnetic resonance in medicine : official journal of the Society of Magnetic Resonance in Medicine / Society of Magnetic Resonance in Medicine*.
180. Boss A, et al. (2006) Whole-body magnetization transfer contrast imaging. *Journal of magnetic resonance imaging : JMRI* 24:1183-1187.
181. Stanisz GJ, et al. (2005) T1, T2 relaxation and magnetization transfer in tissue at 3T. *Magnetic Resonance in Medicine* 54:507-512.

BIOGRAPHICAL SKETCH

Nathan Bryant began his academic career initially interested in the visual arts at Middle Tennessee State University. It was there that an introductory biology course opened his eyes to the prospects of a career in the life sciences. There he majored in general biology, with a concentration in microbiology, and minored in chemistry. He graduated with a B.S. degree in 1999. He continued there, working in the laboratory of Anthony Farone, conducting research on novel *Legionella*-like amoebal pathogens. During this time he was a graduate teaching assistant and instructed the laboratory section of the same introductory biology course that had brought him into the field three years earlier. During this time he was awarded a GAANN fellowship, from the U.S. Department of Education, which he brought with him during his first year of his doctoral studies at the University of Florida.

In Florida, he enrolled in the Interdisciplinary graduate program in biomedical sciences (IDP) in the College of Medicine. He spent his first two years studying the biophysical characteristics of the capsid proteins of Parvoviruses and was interested in their role in virulence and host cell tropism. This work, in the Department of Biochemistry and Molecular Biology, was largely centered around structural studies utilizing X-ray crystallography. The world of three dimensional data sets and computer modeling reunited him with his early interests in the fine arts and computer rendering.

In 2006 he began working in the laboratory of Glenn A. Walter in the Department of Physiology and Functional Genomics and later received an NIH T-32 Training Fellowship in neuromuscular plasticity. His current research, which is the foundation of the dissertation, is focused on developing noninvasive methods of monitoring damage and repair in dystrophic skeletal muscle using MRI. By delving into the science of

imaging, he has been able to interlock his passion for both art and science into his daily work. At present Nathan lives in Gainesville, Florida, enjoys photography, music, camping, rock climbing, Argentine tango, and the company of his friends and family.